Direct Numerical Simulations of plasma-assisted ignition in quiescent and turbulent flow conditions

Maria Luis Gracio Bilro Castela

NNT : 2016SACLC042

THÈSE DE DOCTORAT DE L'UNIVERSITÉ PARIS-SACLAY

préparée à CentraleSupélec

ÉCOLE DOCTORALE N°579

Sciences mécaniques et énergétiques, matériaux et géosciences

Spécialité de doctorat Combustion

Présentée par

MARIA LUÍS GRÁCIO BILRO CASTELA

DIRECT NUMERICAL SIMULATIONS OF PLASMA-ASSISTED IGNITION IN QUIESCENT AND TURBULENT FLOW CONDITIONS

Thése soutenue à Châtenay-Malabry, le 12/05/2016

Composition du jury:

S. Pasquiers	Directeur de Recherche CNRS, LPGP	Président
P. Domingo	Directrice de Recherche CNRS, CORIA	Rapporteur
D. Thévenin	Prof. Otto von Guericke University Magdeburg	Rapporteur
B. Cuenot	Chercheur Senior CERFACS	Examinateur
B. Fiorina	Prof. CentraleSupélec, EM2C	Directeur de thèse
N. Darabiha	Prof. CentraleSupélec, EM2C	Co-Directeur de thèse
C. O Laux	Prof. CentraleSupélec, EM2C	Co-Directeur de thèse
O. Gicquel	Prof. CentraleSupélec, EM2C	Co-Directeur de thèse

Laboratoire d'Énergétique Moléculaire et Macroscopique, Combustion
CNRS, CentraleSupélec.

Abstract

Plasma-assisted combustion has received increasing attention in both plasma and combustion communities. Nanosecond Repetitively Pulsed (NRP) discharges are a promising and efficient technique to initiate and control combustion processes particularly when conventional ignition systems are rather ineffective or too energy costly. Even though a promising technique, the phenomena occurring in NRP discharges-assisted combustion are still poorly understood. The numerical studies presented in the literature are limited to 1-D and 2-D simulations in quiescent conditions. The problem complexity increases in practical configurations as ignition phenomena are also controlled by the flow and mixing field characteristics in and around the discharge channel. Direct Numerical Simulations (DNS) is a powerful research tool to understand these plasma/combustion/flow interactions. However, the computational cost of fully coupled detailed non-equilibrium plasma and combustion chemistry, and high Reynolds number simulations is prohibitive.

This thesis presents a model to describe the effects of non-equilibrium plasma discharges in the set of equations governing the combustion phenomena. Based on the results reported in the literature, the model is constructed by analyzing the channels through which the electric energy is deposited. The two main channels by which the electrons produced during the discharge impact the reactive mixture are considered: 1) the excitation and the subsequent relaxation of the electronic states of nitrogen molecules, which leads to an ultrafast increase of the gas temperature and dissociation of species; and 2) the excitation and relaxation of vibrational states of nitrogen molecules which causes a much slower gas heating. This high level model of NRP discharges allows DNS studies of plasma-assisted combustion / ignition in high turbulent Reynolds number. The complex physics underlying plasma-assisted ignition by multiple discharges in both quiescent and turbulent flow conditions are discussed in the present thesis.

Résumé

La combustion assitée par plasma a reçu une attention croissante dans les deux communautés de plasma et de combustion. Les décharges Nanoseconde Répétitive Pulsée (NRP) sont des techniques prometteuse et efficaces pour initier et contrôler les processus de la combustion en particulier quand les systèmes d'allumage conventionnels sont inefficaces ou trop coûteux en énergie. Néanmoins, les phénomènes rencontrés dans la combustion assistée par plasma sont encore mal connus. Les études numériques présentées dans la litérature sont limitées á des simulations 1-D et 2-D dans des conditions au repos. La complexité du problème augmente dans les configurations pratiques oú le phénomène d'allumage est contrôlé par le mouvement du fluide ainsi que le mélange autour de la zone de décharge. La simulations numérique directe (DNS) est un outil de recherche puissant pour la compréhension des interactions plasma/combustion/écoulement. Toutefois, le coût de calcul de la combustion turbulente avec un nombre de Reynolds élevé et la cinétique chimique détaillée couplée avec le plasma hors-équilibre est prohibitif.

Cette thèse présente un nouveau modèle de couplage plasma-combustion pour introduire les effets des décharges de plasma hors-equilibre dans le système d'équations qui décrit le phénomène de la combustion. Le modèle est construit en analysant les chemins par lesquels l'énergie électrique est transferrée au gaz. Ce modèle de décharges NRP permet des simulations multidimensionales DNS de la combustion et l'allumage assistés par plasma. Les phénomènes physiques complexes de l'allumage assisté par décharges multiples de plasma dans des dans mélanges au repot et en regime d'écoulement turbulent sont analysés dans cette thèse.

Contents

List of Publications

The work developed in this thesis was the object of two publications in peer-reviewed journals and several presentations in international conferences:

Peer-reviewed journals

M. Castela, S. Stepanyan, B. Fiorina, A. Coussement, O. Gicquel, N. Darabiha, C. O. Laux, *A 3-D DNS and experimental study of the effect of the recirculating flow pattern inside a reactive kernel produced by nanosecond plasma discharges in a methane-air mixture*, Accepted for publication in the Proceedings of the Combustion Institute - Seoul, Korea (2016).

M. Castela, B. Fiorina, A. Coussement, O. Gicquel, N. Darabiha, C. O. Laux (2016), Modelling the impact of non-equilibrium discharges on reactive mixtures for simulations of plasma assisted ignition in turbulent flows, *Combustion and Flame, 166, pp 133-147* .

Peer-reviewed conference publications

M. Castela, B. Fiorina, A. Coussement, O. Gicquel, N. Darabiha, C. O. Laux, *Mini-symposium on Safety related ignition processes*, **15^{th} International Conference on Numerical Combustion (ICNC15)**, Avignon, France, April 19-22, (2015).

M. Castela, B. Fiorina, A. Coussement, O. Gicquel, N. Darabiha, C. O. Laux, *Modelling the effects of non-equilibrium discharges on reactive mixtures*, **ATW Fundamentals of Plasma Assisted Combustion and Flow Control** - Les Houches, France, April 12-17, (2015).

M. Castela, B. Fiorina, A. Coussement, O. Gicquel, N. Darabiha, C. O. Laux, *Impact of nanosecond repetitively pulsed electric discharges on the*

ignition of methane-air mixture, **7th European Combustion Meeting (ECM2015)** - Budapest, Hungary, March 30 - April 2, (2015).

M. Castela, B. Fiorina, A. Coussement, O. Gicquel, N. Darabiha, C. O. Laux, *Modelling the impact of plasma discharges on turbulent reactive mixtures*, **International Conference organized by the Portuguese and Spanish Sections of the Combustion Institute** - Lisbon, Portugal, November 19-21, (2014).

M. Castela, B. Fiorina, A. Coussement, O. Gicquel, N. Darabiha, C. O. Laux, *Direct numerical simulations of combustion assisted by discharges in quiescent and turbulent flow conditions*, **10th International ERCOFTAC Symposium on Engineering Turbulence Modelling and Measurements (ETMM10)** - Marbella, Spain, September 17-19, (2014).

M. Castela, B. Fiorina, A. Coussement, O. Gicquel, N. Darabiha, C. O. Laux, *Direct numerical simulations of pulsed discharges assisted combustion in quiescent and turbulent flow conditions*, **10th International Symposium on special topics in chemical propulsion (ISICP-10)** - Poitiers, France, June 2-6, (2014).

Awards

Best poster award at RED - Reencontre Entreprise Doctorants, CentraleSupélec - France (2014)

List of Figures

Chapter 1

Introduction

This chapter provides an overview of the current challenges in combustion systems for which plasma-assisted combustion is a promising technology. The main characteristics of plasma discharges are presented with emphasis on short repetitively-pulsed discharges. Because of its characteristics, simulations of plasma-assisted combustion present additional challenges. To tackle these challenges, several strategies were developed and published in the literature and will be presented and discussed here. We also highlight in this chapter, some open questions regarding the modelling and the physics occurring in plasma-assisted combustion, some of which providing the motivation for this thesis.

Contents

1.1 Challenges of Novel Combustion Technologies

The rising global demand and the scarcity of fossil fuels along with the increasing stringent regulations on pollutant emission and environmental concerns, are the main motivations for the development and/or improvement of new combustion technologies. Worldwide long-term actions include promoting energy efficiency and the development of alternative fuel technologies to use sustainable fuels, including biofuels, in multiple sectors.

In the following sections some of the solutions investigated for combustion technologies to tackle these major challenges in the automobile, industrial and aerospatial/aeronautical sectors are briefly presented. As will be discussed, low-emission and highly-efficient energy technologies are still unable to overcome practical difficulties. Plasma-assisted combustion / ignition may provide the necessary control, improvement and/or the safety factor for a reliable implementation of these new combustion technologies in practical systems.

The fundamentals of plasma discharges are presented in section 1.2 where particular attention is given to nanosecond repetitively-pulsed (NRP) discharges. Base on the experimental and numerical results reported in the literature, the thermal, chemical and hydrodynamic effects induced by this kind of plasma discharges are described.

State-of-the-art numerical simulations of NRP discharges are then presented in sections 1.2.4 and 1.2.5. As will become clear, state-of-the-art numerical simulations of NRP discharges are mostly limited to one-dimensional simulations which are unable to unveil the physics underlying the ignition phenomena in practical combustion devices.

The motivations and the scope of the present thesis are finally given in

section 1.3 where the manuscript is also outlined.

1.1.1 Increase of combustion efficiency and control of pollutant emission

Several solutions have been proposed for industrial burners and automotive engines to reduce pollutant and particulate emissions, and to increase engines efficiency. Most of them rely on premixed or partially-premixed lean combustion regimes. As will be discussed below, the effective application of these new technologies to practical systems is still limited by the capability of controlling ignition and stabilizing the flame over a wide range of operational conditions..

Ground transportation

One of the solutions identified in the automobile industry to reduce soot and NO_x emissions (Taylor 2008) is the use of Homogeneous Charged Compression Ignition (HCCI) (Dec 2009), Partially-Premixed Compression Ignition (PPCI) or Reactivity Controlled Compression Ignition (RCCI) (Reitz and Duraisamy 2015). HCCI combustion engines rely on very lean premixed or partially-premixed combustion, which suppresses fuel-rich zones and consequently reduces soot formation. Lean combustion implies lower in-cylinder peak temperatures and therefore lower NO_x emissions. In HCCI engines, the thermal efficiencies are comparable to those of diesel engines, due to the high compression ratios, and the extremely low NO_x and soot emissions.

The practical implementation of these technologies to transportation engines is still limited by the capability to control auto-ignition timing in a wide range of operation conditions (Dec 2009). While in spark ignition (SI) engines the ignition is controlled by the spark-plug discharge timing, and in diesel compression engines the ignition phenomenon is controlled by the fuel intake, the control of ignition in HCCI engines is much more

challenging due to the lack of an external combustion trigger such as the spark or direct fuel injection. In these engines, ignition is generally based on auto-ignition conditions. Therefore, the combustion initiation in HCCI engines depends largely on the chemistry and thermal conditions inside the cylinder. The strategies to control mixture auto-ignition in HCCI, and thus the heat release rate for a wide range of engine operation conditions, include controlling the amount of exhaust gases recirculation (EGR) going into the cylinder (Dec 2009), the fuel stratification (Dec et al. 2011) and the use of variable compression ratios (Ryan et al. 2004). These strategies can be applied at the expense of increased mechanical complexity.

Advantages of HCCI engines also include the fuel flexibility, provided that certain restrictions on octane and cetane number are respected. Yet, at low loads the temperature inside HCCI engines may drop significantly, leading to the mixture partial burning and increasing unburned HC and CO emissions (Saxena and Bedoya 2013).

Ground power generation

In ground power generation or industrial furnaces MILD or flameless combustion regimes are a promising technique (e.g. Cavaliere and Joannon 2004). In these regimes fuel oxidation occurs within a distributed low temperature reaction zone and in ultra-lean conditions. MILD or flameless combustion regimes are characterized by low CO and NO_x emissions and by a distributed (colourless therefore flameless) reaction zone where the gas temperature and species concentration gradients are much lower than in conventional lean combustion regime, as experimentally observed in e.g. Verissimo et al. (2011). Because of this distributed reaction zone, MILD and flameless combustion regimes are especially suitable in industrial furnaces where a homogenous distribution of the gas temperature is desired (glass industry, for example).

Yang and Blasiak (2005) showed that flameless combustion regime can

only be reached if the inlet velocities of the reactants are high enough to establish recirculation zones inside the combustion chamber. However, increasing the reactant velocities, flame (or a flameless reaction zone) stabilization becomes more difficult. One of the solutions investigated in the literature to overcome these instability issues is to use reversed flow combustion chambers where the burner and the exhaust port are mounted at the same side of the combustion chamber. These geometries increase the flow residence time owing to higher recirculating flow rates. Castela et al. (2012) studied the combustion regimes occurring in a reversed flow combustion chamber. The authors showed that a stable flameless regime could be reached even at ultra-lean conditions and high inlet reactant velocities with this type of combustion chambers. However these reversed flow combustion chambers are not ideal for gas turbine engines. Thus the application of this regime to gas turbine engines or industrial furnaces still relies on the ability to stabilize a highly diluted reaction zone, in ultra-lean conditions for a wide range of operation conditions. The variation of the operation conditions may lead to mixture partial burning or misfire and to an increase of the thermo-acoustic instabilities.

1.1.2 Air transportation and development of Ram / Scramjet engines for air breathing vehicles

Aeronautical combustion systems

In air transportation, some of the solutions that are currently being investigated to increase aeronautical engines efficiency and to reduce pollutant emission are also associated with lean combustion regimes. The major drawback associated with these solutions is the in-flight relight capability at high altitudes and the increase of the thermo-acoustic instabilities.
Mixture ignition and flame stabilization inside an aeronautical engine are especially difficult. For jet engines, the flow velocity at the inlet of the combustion chamber is of the order of 150 m/s which is significantly higher than the turbulent flame velocity. It is therefore necessary to generate

low velocity regions in order to stabilize the flame. A common strategy is to use swirled injection systems to induce flow recirculation and therefore increase the flow residence time. Other solutions include the staged fuel injection and structural adapted flame holders. However, in lean and low NO_x engines design, these solutions may still not be sufficient to effectively stabilize the flame and avoid thermo-acoustic instabilities, as discussed in Lefebvre (1998).

Development of hypersonic air breathing vehicles

The development of hypersonic air breathing vehicles presents even more relevant technical difficulties. Mixture ignition and flame stabilization inside a supersonic combustion chamber is especially difficult. Indeed, in ram/ scramjet engines Mach numbers can easily reach values of the order of 2 to 3, at the inlet of the combustion chamber. As discussed in Macheret et al. (2005) at typical conditions of pressures $p = 0.5$ - 2 atm, static temperature of $T = 400$ - 1000 K and flow velocity of the order of 1000 to 2000 m/s, the auto-ignition delay of hydrocarbon-air mixtures is of the order of milliseconds which translates into an ignition length of the order of meters. Although mechanical wall steps, cavities and other surface alterations are capable of increasing the flow residence time to values close to the ignition delay times, these structural modifications are also responsible for a significant loss of thrust power.

1.1.3 Plasma-assisted combustion/ ignition technologies

As will be discussed in the following sections, the above-mentioned solutions such as staged fuel injection, structural adapted flame holders or swirled injection systems can be combined with energy-efficient plasmas for an effective mixture ignition and flame stabilization in the above described stringent combustion regimes. As recently summarized in comprehensive reviews of Ju and Sun (2015) and Starikovskiy and Aleksandrov

(2013), plasma-assisted combustion is a promising technique for combustion systems. Plasma discharges enhance combustion processes by promoting fuel oxidation at low gas temperatures and decreasing the ignition delay as will be discussed in detail in the following sections.

1.2 Fundamentals and background studies of plasma-assisted combustion

1.2.1 Ignition processes

The application of plasma discharges to ignition of fuel-air mixtures dates back to the first commercially successful internal combustion engine, created by Etienne Lenoir around 1859. The voltage pulse applied to the gas ignites the fuel-air mixture by promoting fuel oxidation and the release of the chemical energy of the fuel. The enhancement of exothermal chemical reactions increases the gas temperature and the gas pressure inside a confined combustion chamber, forcing the movement of some components of the engine. The conversion of the chemical energy into mechanical energy relies on the fact that ignition will occur.

In the first stage, the successful formation of the ignition kernel depends on the applied voltage and on the gas mixture composition, temperature and pressure (Maly and Vogel 1984; Ziegler et al. 1984; Kono et al. 1984; Tagalian and Heywood 1986; Lefebvre 1998).

The expansion and propagation of this ignition kernel will then depend on the flow field characteristics and on the mixture composition and temperature in the vicinity of the discharge zone (Ballal and Lefebvre 1975; Lefebvre 1998; Mastorakos 2009; Cardin et al. 2013).

The ignition dynamics is of an extreme importance in combustion systems (Lefebvre 1998). It has motivated several studies by numerous authors over the past decades in the context of gas turbines (Ballal and Lefebvre

1975, Bourgouin et al. 2013, Bach et al. 2013) and internal combustion engines (Tagalian and Heywood 1986; Dale et al. 1997).

The above mentioned works consider ignition by thermal equilibrium plasmas. However, plasmas in thermal non-equilibrium have comparatively different characteristics of those of thermal equilibrium plasmas. The mechanisms by which these thermal non-equilibrium plasmas impact ignition and combustion processes are still not fully understood and constitutes the main scope of the present thesis. A comparative description of the characteristics of thermal equilibrium and thermal non-equilibrium discharges is given next.

1.2.2 Equilibrium and non-equilibrium plasmas

When the voltage is applied to the electrodes, an electric field is formed inside the discharge zone causing an increase of the kinetic energy of free electrons. The energy exchange between electrons and other gas particles occurs through collisional processes. At the end of the discharge, if the temperature of the electrons, T_e, defined by their kinetic energy, is in equilibrium with the temperature of other particles, T_g, the plasma is categorized as a thermal equilibrium plasma ($T_e \approx T_g$). The plasma is said in thermal non-equilibrium if the temperature of the electrons remains much higher than the gas temperature ($T_e >> T_g$). Therefore, plasmas can be divided into thermal non-equilibrium and thermal equilibrium plasmas.

In equilibrium plasmas, the gas temperature is very high, reaching values in the range of 10 000 - 50 000 K, whereas in non-equilibrium plasmas, although the temperature of the electrons T_e can reach values of the order of 10 000 - 100 000 K, the gas remains at much lower temperatures: 300 - 3000 K. In these plasmas, the collisions between electrons and surrounding particles lead to the excitation of molecules into different energy modes and also to molecular dissociation. As in non-equilibrium plasmas

the electrons have higher energy than in thermal plasmas, the electron-impact with other molecules are much more efficient for the vibrational and electronic excitation of molecules, increasing the gas vibrational and electronic temperatures. The vibrational and electronic temperatures are higher than the neutral gas temperature, T_g, leading to thermal non-equilibrium.

The distribution of the discharge energy over different energy modes of molecules (for instance rotational, vibrational and electronic states) depends on the number density and on the kinetic energy (temperature) of the electrons and also on the gas composition. The electrons number density and their kinetic energy are a function of the electric field magnitude, applied during the discharge, and a function of the density of particles affected by this electric field. Therefore, the reduced electric field strength E/N, defined as the ratio of the electric field magnitude E to the gas number density N, is the key parameter that governs the rate of collisions of the electrons with surrounding particles. Therefore, the population of different energy modes of molecules is a function of the applied reduced electric field E/N. This parameter is expressed in Townsend units, with 1 Td = 10^{-17} Vcm^2.

Figure 1.1 shows the kinetic energy of the electrons and the reduced electric fields characteristics of different plasma discharges (Sun 2013). Spark discharges produce thermal equilibrium plasmas and internal combustion engines, gas turbines and most of the conventional combustion systems use this type of discharges to ignite the mixture. Discharges such as corona, dielectric barrier, and nanosecond pulsed discharges, produce non-equilibrium plasmas at atmospheric pressures.

Non-equilibrium plasmas at low gas pressures was experimentally investigated by the plasma group at Moscow Institute of Physics and Technology, in the form of 'fast ionization wave'. However, at high pressures (atmospheric pressures) collisional processes tend to equilibrate the electron

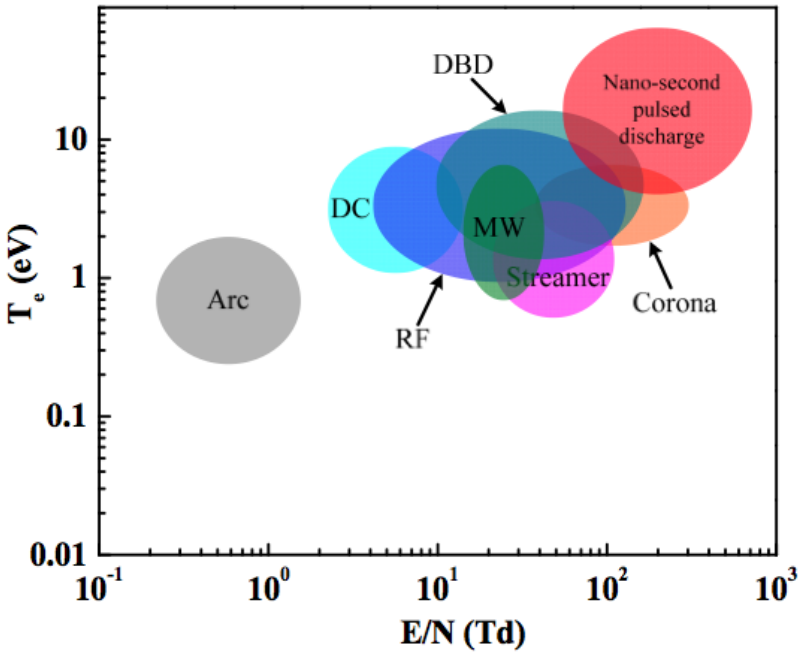

Figure 1.1: *Schematic comparison of the electron temperatures and reduced electric fields for different discharges: DC: direct current discharges, MW: microwave discharges, DBD: dielectric barrier dischargees, RF radio frequency discharges. Reproduced from Sun (2013).*

temperature and the gas temperature. Thus, the initial non-equilibrium state rapidly turns into thermal equilibrium and $T_e \approx T_g$, unnecessarily rising the gas temperature to values beyond the ones needed in most combustion applications. This represents a drawback for the application of non-equilibrium plasmas in practical combustion systems as in most devices combustion occurs at high pressures. The Stanford group Kruger, Laux, Yu, Packan, and Pierrot (2002) demonstrated that by reducing the duration of the discharge to few nanoseconds an by repetitively pulsing the electric discharges, it was possible to sustain a non-equilibrium plasma state at atmospheric pressures. These discharges are known as Nanosecond Repetitively Pulsed (NRP) discharges and are characterized by high-voltage pulses (from 5 to 20 kV) that last for few nanoseconds and are repeated at frequencies of the order of tens of kHz.

Ignition by NRP discharges in propane-air mixture was studied by Pancheshnyi et al. (2006). A train of NRP discharges were applied in a propane air mixture inside a confined laboratory combustion chamber. The results showed an increase of the fuel consumption rate during the initial state of the ignition kernel growth and a significant reduction of the ignition delay when NRP discharges were used over that with conventional spark. A comparative analysis of NRP discharges Vs. conventional spark ignition was performed by Xu et al. (2015). The results showed that with NRP discharges, the kernel expansion was faster compared with conventional spark.

The beneficial effects of using these non-equilibrium plasmas on premixed swirled burners, representative of aeronautical combustors, were recently observed by Barbosa et al. (2015). It was shown that with plasma discharges the burner lean extinction limit was four times lower than without plasma discharges, and that the flame remained robust and stable at these stringent ultra-lean combustion conditions. As in Pilla et al. (2006), the results presented in Barbosa et al. (2015) also unveiled the importance of the discharge repetition frequency on the combustion effectiveness. For instance, a strong effect was obtained by increasing the pulse frequency from 11 to 33 kHz, and therefore the plasma power by a factor of three. Nevertheless these works have shown that with an energy of less than 1% of the flame power, lean flammability limits can be significantly extended. Fig. 1.2 shows a comparison of the OH(A-X) emission with and without NRP discharges from the work of Pilla et al. (2006). When NRP discharges are applied inside the recirculation zone created behind the burner, the results show that the OH* emission is intensified. This means that plasma significantly increases the heat release even at ultra-lean conditions and helps stabilize the flame which otherwise would not be possible.

In supersonic combustion regimes, Do et al. (2010a) used NRP discharges located within a cavity to ignite a crossflow supersonic jet of hydrogen

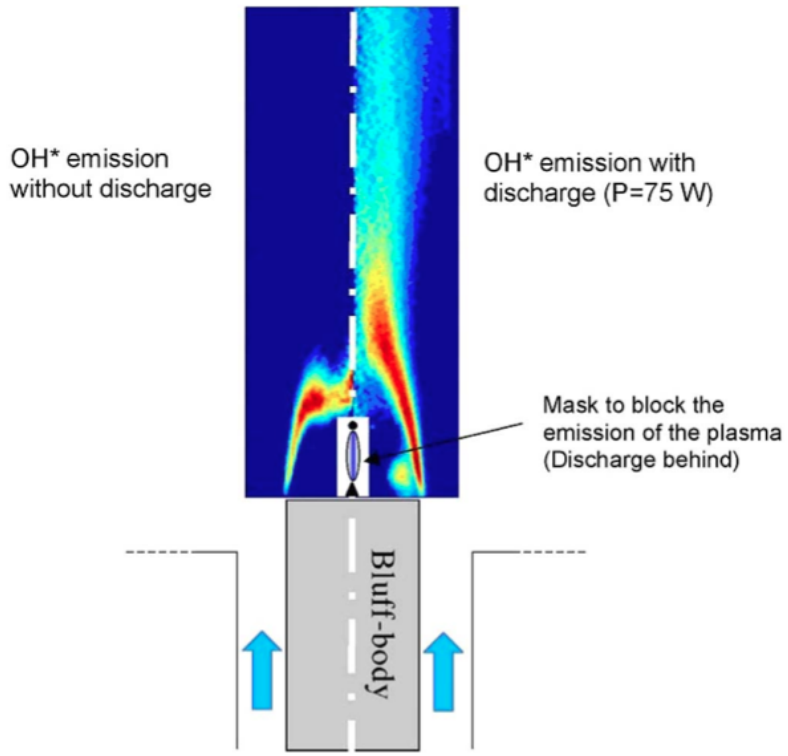

Figure 1.2: *Comparison of OH (A-X) emission with and without discharge after Abel transform; air: 14.7 m^3 h^{-1} , propane: 0.5 m^3 h^{-1} (ϕ = 0.83). Flame power: 12.5 kW, discharge power: 75 W. Emission of the plasma was blocked to prevent saturation of the ICCD. Reproduced from Pilla et al. (2006).*

and ethylene. A second study (Do et al. 2010b) showed that staged fuel injection combined with NRP discharges can also ignite/hold the flame even without structural adapted flame holders.

As will be further detailed in the next section, non-equilibrium plasmas are of particular interest for combustion applications. The ability to generate high amounts of excited species and radicals in a short characteristic time (of the order of nanoseconds) because of the high energy of electrons, will impact ignition and combustion processes. Moreover, radicals are generated at much lower gas temperatures compared to those reached in conventional spark ignition. For this reason, NRP discharges

are energy-efficient plasmas.

1.2.3 Thermal, chemical and hydrodynamic effects of NRP discharges

The energy of the electric discharge in non-equilibrium plasma discharges is spent on ultrafast ionization, excitation and dissociation of molecules rather than just in increasing the gas temperature (Nighan 1970; Aleksandrov et al. 1981). As previously shown in Fig. 1.1, NRP discharges are formed at high reduced electric fields. For values of reduced electric fields E/N in the range 100-400 Td (1 Td = 10^{-17} Vcm^2), the electrons accelerated by the electric field mainly produce electronically ($A^3\sum_u^+$, $B^3\Pi_g$, $C^3\Pi_u$, $a'^1\sum_u$ ...) and vibrationally excited molecular nitrogen (Nighan 1970; Aleksandrov et al. 1981). This is the case in air, but also in hydrocarbon-air mixtures, as shown by Starikovskiy and Aleksandrov (2013). (Further details will be given in chapter 2)

Thermal and chemical effects

The relaxation of electronically excited N_2 molecules by collisional quenching reactions with O_2 molecules results in an ultrafast (time scales of nanoseconds) increase of O atoms and gas temperature by about 1000 K inside the discharge channel. At atmospheric pressure, molecular oxygen can be almost fully dissociated in the inter-electrode region as demonstrated experimentally by Stancu et al. (2010); Lo et al. (2012) and Rusterholtz et al. (2013). Such a high concentration of O radicals is likely to have a positive effect on both ignition and flame stabilization. For instance, in the work presented by Sun et al. (2012) the effect of non-equilibrium plasma on the enhancement of CH_4 diffusion flames extinction limits at low gas pressure (60 Torr) was investigated. The authors argued that the formation of O radicals within the discharge time scale was the critical species for the extinction limits enhancement, due to its prompt recombination with CH_4 even at low gas temperatures.

Another study of plasma-flame interaction was presented by Nagaraja et al. (2015). Spatially resolved, quantitative OH mole fraction and temperature measurements were performed in the vicinity of a $H_2/O_2/N_2$ laminar flame also at low gas pressures (25 Torr). Along with experiments, numerical simulations were also performed. The numerical results showed an increase of the mixture reactivity due to the O and H radicals production inside the pre-heated zone of the laminar flame induced by the burst of 200-nanosecond plasma pulses. In this study gas heating by Joule effect was not able to explain alone the flame shifting towards the burner. The ultrafast formation of radicals by NRP discharges was also discussed in Yin et al. (2013) and Breden et al. (2013).

Hydrodynamic characteristics of NRP discharges

Besides these thermal and chemical effects, hydrodynamic effects are also induced by NRP discharges as it was observed in the experiments of Xu et al. (2011). During each nanosecond pulse, because of the ultrafast energy deposition, the gas temperature increases inside the discharge channel in a quasi-constant volume process also leading to an increase of the gas pressure inside the discharge channel. Following this temperature and pressure rise, the gas expands and a shock wave propagates outwards from the centre of the discharge channel. These hydrodynamic effects occurs in every single nanosecond discharge as shown in Fig. 1.3, and, therefore, after a sequence of nanosecond repetitively pulsed discharges it may result in flow turbulization around the discharge channel as shown in Fig. 1.4. The evolution of the hydrodynamic parameters (such as density, temperature and pressure) following a NRP discharge is described in detail in the work of Xu (2013). In Xu et al. (2015) it was suggested that these hydrodynamic effects can produce a wrinkling of the flame front, thus enhancing ignition, in particular at high pressures (10 atm).

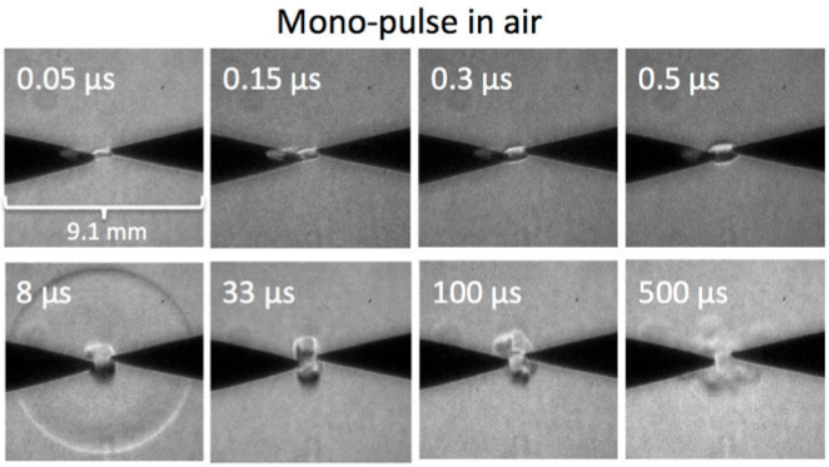

Figure 1.3: *Single-shot schlieren images capturing the hydrodynamic effects induced by a single NRP discharge in air. Reproduced from Xu (2013)*

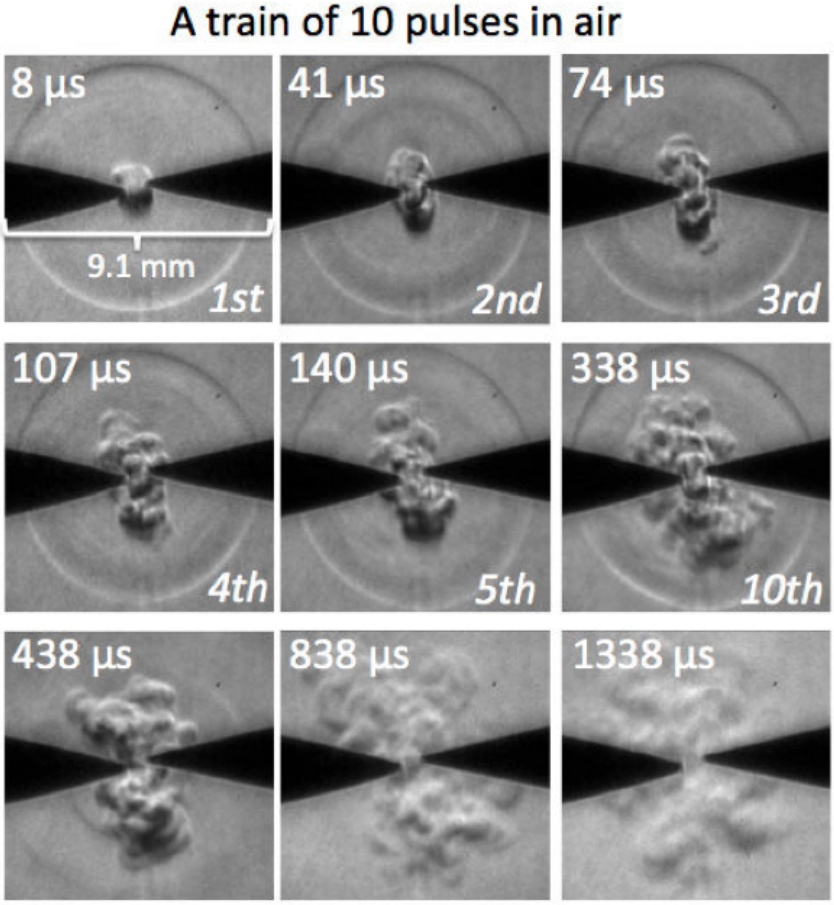

Figure 1.4: *Single-shot schlieren images capturing the hydrodynamic effects induced by a train of 10 nanosecond discharges in air applied at pulse repetition frequency of 30 kHz. Reproduced from Xu (2013)*

1.2.4 Coupling plasma and combustion numerical models

In the early 80's Ballal and Lefebvre (1981) developed a general model of spark ignition for gaseous and liquid fuel-air mixtures based on theoretical analysis and experimental observations (Ballal and Lefebvre 1975). In classical spark ignition models it is assumed that the spark creates a spherical volume of burnt gases which in order to create a self-sustained flame kernel, must be of sufficient size so the heat release within its volume exceeds the rate of heat loss to its surroundings. The minimum energy required to form this spherical flame kernel with a characteristic quenching diameter d_q, that successfully propagates through the surrounding fresh mixture, is defined as the Minimum Ignition Energy (MIE). This MIE can be computed or modelled as a function of the mixture composition and flow field characteristics provided that the chemical reaction mechanism and the fluid dynamics are known. Chemical reactions mechanisms will govern the evolution of the gas thermodynamics and transport properties.

Most reaction mechanisms to model combustion and ignition consider that the gas is in thermal equilibrium, i.e., species are in thermal equilibrium at a given gas temperature (even though species can be in chemical non-equilibrium). However, as discussed before, NRP discharges produce non-equilibrium plasmas and, therefore, the rotational, vibrational and electronic excited states are usually not in thermal equilibrium at overall gas temperature. Modelling NRP discharges along with combustion processes requires, therefore, coupling thermal and chemical non-equilibrium.

To accurately model the non-equilibrium chemical processes, the kinetic mechanisms must also include plasma reactions such as electron-impact excitation and ionization, as well as reactions associated with the relaxation of the excited states. Rate constants of electron-impact reactions are calculated as a function of the electron energy distribution function (EEDF) which depends on the value of the reduced electric field E/N dur-

ing the discharge. Rate constants associated with the relaxation of excited states can be obtained from fundamental experimental work (e.g. Stancu et al. 2010; Rusterholtz et al. 2013). The simulations of plasma-assisted ignition / combustion presented in the literature are mostly based on this methodology. Detailed plasma and combustion kinetic mechanisms will be further discussed in Chapter 2.

1.2.5 Multi-dimensional simulations of single / multiple plasma discharges in reactive mixtures

Multidimensional modelling of ignition kernel formation by conventional spark (thermal plasma) has been largely investigated, for instance, by Kravchik and Sher (1994); Kravchik et al. (1995) and later on by Thiele et al. (2000a, 2000b) and Nakaya et al. (2011). In these later works, 2-D numerical simulations in quiescent flow conditions with detailed chemistry, including ionization processes, were used to study the early development of the flame kernel and the fluid motion induced by a single spark discharge.

In Echekki and Kolera-Gokula (2007) 2-D numerical simulations were performed with a two-step global kinetic mechanism to analyse kernel - vortex interactions, where the ignition kernel was initialized as spherical flame in a homogeneous gas mixture. The authors identified four regimes for the ignition kernel development depending on the vortex strength: 1- laminar kernel regime, 2- the wrinkled kernel regime, 3- the breakthrough regime and 4 - the global extinction regime. These regimes were also observed in the 2-D DNS studies of turbulence-ignition kernel interactions performed by Reddy and Abraham (2013). 3-D DNS with simplified chemistry have been performed to study the impact of different turbulence intensities on spark ignition in inhomogeneous mixtures in Chakraborty et al. (2007). In the study performed by Fru et al. (2011), the development of the ignition kernel was also analysed by means of a 3-D DNS, for different levels of turbulence and mixture equivalent ratios. With the increase of turbu-

lence, these simulation results showed that the initial spherical flame was being stretched leading to the formation of hot gas pockets at the edges of the ignition kernel.

In all the above-mentioned studies, the ignition kernel is formed using a conventional spark energy deposition model or is modeled as spherical volume of burnt gases at the beginning of the computations.

Few multidimensional simulations of non-equilibrium plasmas in reactive mixtures are reported in the literature. In Breden et al. (2013) 2-D simulations were performed to study the propagation of streamers produced by non-equilibrium discharges in methane-air mixtures. The study was performed in a coaxial electrode and corona geometry and at high pressure conditions, as found in automotive combustion engines (10 atm). Simulation results showed that the propagation of the streamer resulted in a spatio-temporal production of radicals such as O and H and that the variation of the mixture equivalence ratio had a relatively small effect on the concentration of these radicals. A 2-D simulation of a single nanosecond spark discharge in a quiescent hydrogen/air mixture was performed by Tholin et al. (2014) using a detailed plasma/hydrogen-air kinetic mechanism coupled with streamer dynamics. In these two studies (Tholin et al. 2014 and Breden et al. 2013) non-equilibrium plasma effects on reactive mixtures were studied for a single pulse. The effects of nanosecond repetitively pulsed discharges on flame stabilization were numerically and experimentally investigated by Bak et al. (2012). Although a detailed plasma and combustion mechanism was used to capture non-equilibrium chemistry, the mesh grid used in these 2-D simulations only considered 2 points inside the discharge zone and, therefore, it was not clear if the hydrodynamic effects of repetitively pulsed discharges observed in Xu et al. (2011) were captured in these simulations.

To our knowledge, 2-D and 3-D DNS studies of ignition by multiple pulses have not been performed yet, either in quiescent or in turbulent flow con-

ditions. Although, simulations of ignition kernel formation and development have been performed for conventional spark ignition, as will be discussed in this manuscript, the physics underlying plasma-assisted ignition when ignition occurs after several pulses are significantly different from the physics governing conventional spark ignition.

1.3 Motivations and aim of the present work

1.3.1 Open questions in plasma-assisted ignition

Even though a promising technique, the phenomena occurring in NRP discharge-assisted combustion or ignition are still poorly understood, especially the gas dynamics and thermochemical coupling between the discharge and the reactive flow. The problem complexity increases when the formation of a sustainable ignition kernel occurs after several NRP discharges and not after a single pulse as in conventional spark ignition. The radicals formed by each pulse enhance chain-branching reactions, increasing the local concentration of intermediate combustion species pulse after pulse and, therefore, the mixture reactivity. In turbulent flows, the high-temperature and highly reactive kernel formed at each pulse may be stretched and convected away from the discharge zone before the next pulse, yielding a non-uniform distribution of temperature and concentration of radicals inside the discharge zone at the beginning of the following pulse. Depending on the characteristic time and length scales of turbulence and on the pulse repetition frequency, the synergistic effect of repetitively pulsed discharges may be reduced. Therefore, the number of pulses needed to ignite the mixture and the ignition delay may significantly increase.

1.3.2 Aim of the present thesis

The main objective of this thesis is to identify and understand the physics underlying plasma-assisted ignition, when ignition occurs after several

nanosecond pulses in quiescent and in turbulent flow conditions.

Direct Numerical Simulation (DNS) was the chosen research tool to understand the ignition phenomena by NRP discharges and capture the complex plasma /combustion / turbulence interactions. Yet, DNS is still CPU-limited and multi-dimensional simulations considering fully coupled detailed non-equilibrium plasma and combustion chemistry, and high Reynolds numbers are still out of reach.

The following strategies were developed during this thesis to achieve the proposed objective:

- **Development of a plasma-combustion model**
  A phenomenological model of non-equilibrium plasma discharges was developed to capture the non-equilibrium plasma effects on the set of multicomponent reactive flow balance equations governing the combustion phenomena. The proposed high level model of NRP discharges avoids including detailed non-equilibrium plasma kinetics. Yet, this model captures the essential effects of these discharges and, therefore, reduces the computational costs of high Reynolds flows DNS computations. Nevertheless, we still include a detailed chemical kinetic model for hydrocarbons-air mixtures as well as multispecies transport model to capture the transient characteristics of NRP discharge-assisted ignition.

- **2-D and 3-D DNS of NRP discharges in air and fuel-air mixtures in quiescent and turbulent conditions**
  The model was implemented in a DNS solver and validated against experimental results. Relatively simple numerical experiments were then designed to capture the most important physics observed in laboratory-scale experiments of NRP discharges in air and in methane-air mixtures.

1.4 Outline of the Dissertation

The manuscript is organized in 5 chapters, of which the present one provides the introduction, the motivation and the scope of this work.

In **Chapter 2**, the set of balance equations governing the combustion phenomena are first revisited. A review of plasma-assisted combustion models is then briefly presented. Base on the NRP discharge characteristics, and on the results reported in the literature, a general description and mathematical framework of a novel phenomenological plasma model is presented. Finally, an analytical formulation is proposed for model closure and the model is validated against experimental data.

In **Chapter 3** the DNS solver and the 2-D numerical domain is presented. The results of the 2-D DNS of NRP discharges in air are analysed and compared with the experimental results obtained in the steady state regime after a sequence of NRP discharges in air.

In **Chapter 4** the physics governing the plasma-assisted ignition phenomena are analysed by means of 2-D DNS computations of a train of NRP discharges in a methane-air mixture. Two series of test-cases are performed: the first one analyses the impact of NRP discharges on the ignition enhancement in quiescent conditions; the second series of test-cases investigates the impact of turbulence on the ignition kernel formation and development.

Finally **Chapter 5** presents a 3-D DNS and experimental studies of the effects of the recirculating flow pattern in the ignition kernel produced by a single nanosecond discharge.

Chapter 2

Phenomenological Model for Non-equilibrium Plasma Discharges in Reactive Mixtures

In this chapter, the principles and the mathematical framework of a novel plasma-combustion model are presented. The set of conservation equations governing the combustion phenomena is first described. The conventional strategy to model plasma-assisted combustion is then briefly presented. Based on plasma simulations computed with detailed plasma models, and on experimental observations, a phenomenological analysis is performed to identify the mechanisms by which the electric energy deposited during the discharge impacts the thermal and chemical state of the gas. A phenomenological model is then formulated to incorporate discharges effects into the system of equations governing plasma-assisted combustion phenomena.

Contents

2.1 Introduction

During each high voltage nanosecond pulse, the kinetic energy of the electrons increases. This kinetic energy is then transferred to the surrounding heavy particles through collisional processes. The rates at which these collisional processes occur depend on the reduced electric field E/N defined as the ratio of the electric field magnitude E to the gas number density N. Several detailed plasma kinetic mechanisms have been proposed in the literature (e.g. Popov 2001; Popov 2011b; Kosarev et al. 2012; Adamovich et al. 2015; Starik et al. 2015; Lefkowitz et al. 2015) to model the effects of non-equilibrium discharges on combustion processes. The method consists in solving the governing equations for the electric field and the electron energy distribution function, and the continuity equations for neutral and excited species, as well as the energy, mass and momentum balance equations for the gas mixture. At the end of the discharge, the thermodynamic state of the gas can be characterized using this modeling strategy provided that the plasma-related reaction rates are known. However, as will be discussed in this chapter, the chemical pathways in plasma-assisted combustion are still poorly understood. Moreover, strategies to model plasma-assisted combustion with the consideration of detailed plasma kinetics require intensive computational resources for multi-dimensional DNS computations.

To address these limitations, a model is presented in this chapter to provide physically realistic, yet computationally tractable method to enable multi-dimensional DNS studies of plasma-assisted combustion. This is possible because for reduced electric fields in the range of the typical values found in nanosecond pulsed discharges, the effects of the plasma on the gas mixture are well identified in the literature, as will be discussed in detail in this chapter.

2.2 Conservation equations for reactive flows without plasma discharges

In this section, the conservation equations for reactive flows in thermal equilibrium are briefly presented in order to give the thermochemical definitions and equations for the development of the phenomenological plasma model.

2.2.1 Balance equations

The conservation equations for multicomponent reacting systems, where N_{sp} species are in thermal equilibrium, can be written as follows:

$$\frac{\partial \rho}{\partial t} + \frac{\partial (\rho u_i)}{\partial x_i} = 0 \tag{2.1}$$

$$\frac{\partial (\rho u_j)}{\partial t} + \frac{\partial (\rho u_i u_j)}{\partial x_i} = -\frac{\partial p}{\partial x_j} + \frac{\partial \tau_{ij}}{\partial x_i} \tag{2.2}$$

$$\frac{\partial (\rho e)}{\partial t} + \frac{\partial (\rho u_i e)}{\partial x_i} = -\frac{\partial q_i}{\partial x_i} + \frac{\partial (\sigma_{ij} u_i)}{\partial x_i} \tag{2.3}$$

$$\frac{\partial (\rho Y_k)}{\partial t} + \frac{\partial (\rho u_i Y_k)}{\partial x_i} = -\frac{\partial (\rho V_{k,i} Y_k)}{\partial x_i} + W_k \dot{\omega}_k^c \tag{2.4}$$

where ρ is the density, u_i the velocity component in x_i spatial direction, p the pressure and τ_{ij} the viscous tensor defined by:

$$\tau_{ij} = -\frac{2}{3}\mu \frac{\partial u_l}{\partial x_l}\delta_{ij} + \mu \left(\frac{\partial u_i}{\partial x_j} + \frac{\partial u_j}{\partial x_i} \right) \tag{2.5}$$

with μ the dynamic viscosity and δ_{ij} the kronecker symbol.
In Eq. (2.3), e refers to the gas total energy per unit mass, defined as the sum of kinetic, thermal and chemical energies as follows:

$$e = \frac{1}{2} u_i u_i + \sum_{k=1}^{N_{sp}} (e_{sk} + \Delta h^o_{f,k}) Y_k \tag{2.6}$$

where e_{sk} and $\Delta h^o_{f,k}$ are the sensible energy and enthalpy of formation of

the k^{th} species, respectively, and Y_k is the mass fraction of the k^{th} species. σ_{ij} is given by:

$$\sigma_{ij} = \tau_{ij} - \frac{\partial u_j}{\partial x_i} p\delta_{ij} \tag{2.7}$$

The energy flux q_i is the combination of the Fourier flux and the enthalpy flux induced by species diffusion:

$$q_i = -\lambda \frac{\partial T}{\partial x_i} + \rho \sum_{k=1}^{N_{sp}} h_k Y_k V_{k,i} \tag{2.8}$$

where λ is the heat conduction coefficient of the mixture and $h_k = h_{s,k} + \Delta h^o_{f,k}$ is the sum of the sensible enthalpy and the enthalpy of formation of the k^{th} species.

The molecular diffusion term $\rho Y_k V_{k,i}$ in this equation and in Eq. (2.4) is computed assuming the Hirschfelder and Curtiss approximation, yielding:

$$\rho Y_k V_{k,i} = -\rho \left(D_k \frac{W_k}{W} \frac{\partial X_k}{\partial x_i} - Y_k V_i^c \right) \tag{2.9}$$

where W, W_k are the mixture and the k^{th} species molar masses, respectively. D_k represents the diffusion coefficient of the k^{th} species in the mixture and is given by:

$$D_k = \frac{1 - Y_k}{\sum_{j \neq k} X_j / \mathcal{D}_{jk}} \tag{2.10}$$

where $\mathcal{D}_{jk}$ is the binary diffusion coefficient of species k into j, and X_j is the mole fraction of species j. V_i^c is the correction velocity to ensure the global mass conservation:

$$V_i^c = \sum_{k=1}^{N_{sp}} D_k \frac{W_k}{W} \frac{\partial X_k}{\partial x_i} \tag{2.11}$$

In Eq. (2.4), $\dot{\omega}_k^c$ is the molar production rate of the k^{th} species due to combustion reactions described in the following subsection.

2.2.2 Chemical kinetics model

Considering a system composed by N_{sp} species that can react according to a specific reaction mechanism comprising the following I reactions:

$$\sum_{k=1}^{N_{sp}} \nu'_{ki}\chi_k \rightarrow \sum_{k=1}^{N_{sp}} \nu''_{ki}\chi_k \qquad \text{for } i = 1 \text{ to } I \tag{2.12}$$

where ν'_{ki} and ν''_{ki} are the stoichiometric coefficients of the k^{th} species appearing in the i^{th} reaction as a reactant and as a product, respectively. χ_k is the chemical symbol of species k. Mass conservation implies:

$$\sum_{k=1}^{N_{sp}} \nu'_{ki}M_k = \sum_{k=1}^{N_{sp}} \nu''_{ki}M_k \qquad \text{for } i = 1 \text{ to } I \tag{2.13}$$

The overall production rate of the k^{th} species $\dot{\omega}_k^c$ is therefore determined by the sum of all reaction rates of the I elementary reactions:

$$\dot{\omega}_k^c = \sum_{i=1}^{I} (\nu''_{ki} - \nu'_{ki})\mathcal{Q}_i \tag{2.14}$$

$$\text{with} \qquad \mathcal{Q}_i = K_{fi} \prod_{j=1}^{N_{sp}} [X_j]^{\nu'_{ji}} - K_{ri} \prod_{j=1}^{N_{sp}} [X_j]^{\nu''_{ji}}$$

where $\mathcal{Q}_i$ is the rate of progress of the i^{th} reaction, $[X_j]$ is the molar concentration of the j^{th} species, and K_{fi} and K_{ri} are the rate constants for forward and reverse i^{th} reaction given in Arrhenius form by:

$$K_{fi} = A_{fi}\, T_g^{b_i}\, \exp\left(-\frac{E_i}{RT_g}\right) \tag{2.15}$$

where A_{fi} is the pre-exponential factor, b_i a constant, E_i the activation energy, T_g the gas temperature and R the universal gas constant.

2.3 Review of plasma-assisted combustion models

The evolution of the system, described by the set of equations presented in the previous section, is based on the assumption of thermal equilibrium. This means that, at a given point of space and time, all species are at the same local kinetic temperature T_g. This assumption does not hold in plasma-assisted combustion where the discharge induces electron kinetic temperatures that are much higher than the gas kinetic temperatures.

The equations and models used to simulate plasma-assisted combustion in the literature are briefly presented in this section. The same thermodynamic formalism introduced in the previous sections is used. In addition to ground state species (as those found in most combustion models), electrons, excited and ionized species are also considered in the following set of balance equations.

2.3.1 Energy balance equation

First, the discharge energy deposition rate per unit volume $P(t)$ is added as a source term to the energy balance equation Eq. (2.3):

$$\frac{\partial(\rho e)}{\partial t} + \frac{\partial(\rho u_i e)}{\partial x_i} = -\frac{\partial q_i}{\partial x_i} + \frac{\partial(\sigma_{ij} u_i)}{\partial x_i} + P(t) \tag{2.16}$$

By definition, the discharge energy power $P(t)$ is computed with the applied voltage $V(t)$ and the induced discharge current $I(t)$ as follows:

$$P(t) = \frac{V(t)\, I(t)}{V_{discharge}} \tag{2.17}$$

where $V_{discharge}$ is the volume of the discharge channel.

Figure 2.1 shows a schematic representation of the strategy used to compute this discharge energy deposition rate $P(t)$. The basic concepts are

described below:

- The electric potential difference on the electrodes induces an electric field E between the electrodes. During the discharge, the spatial evolution of E can be computed by solving the Poisson's equation along with the drift-diffusion equations for electrons, positive and negative ions. In the studies of streamer dynamics (Celestin (2008) and Tholin (2012)) it is necessary to solve these equations in order to determine the streamer propagation phenomena. With typical streamer velocities of about 10^8 cm s^{-1} (Babaeva and Naidis (1997)), the characteristic time of streamer propagation in a gap with length $L_d = 1$ mm is about 1 ns. Therefore, in order to accurately resolve the streamer phenomena, very small integration time steps are required in the computations. The importance of the streamer phase in single spark formation is discussed, for example, in Marode (1975); Babaeva and Naidis (1997); Celestin (2008); Tholin (2012); Breden et al. (2013).

  An important result in nanosecond repetitively pulsed spark conditions is demonstrated in Pai et al. (2010). Based on experimental results, the authors demonstrated that the electric field is uniformly distributed in the inter-electrode region and that the development of the discharge is uniform along the gap. With this result, the computation of the electric field E becomes significantly simplified. Indeed, considering that E is uniformly distributed in the gap, its temporal evolution can be calculated from the temporal evolution of $V(t)$ as follows:

$$E(t) = \frac{V(t)}{L_d} \tag{2.18}$$

  where L_d is the inter-electrode distance, as represented in Fig. 2.1. In NRP spark conditions, this model for E avoids solving the Poisson's equation along with drift-diffusion equations that otherwise

would be needed to derive the spatio-temporal evolution of E during the discharge.

- Another simplification in NRP discharges is that the magnetic field induced by the discharge current is negligible compared with the magnitude of the electric field E, as discussed in Celestin (2008) and Tholin (2012).
  Therefore, accordingly to Ohm's law and assuming a negligible contribution of the magnetic field, the discharge current $I(t)$ is given by:

$$I(t) = e^{-} N_e \, v_{drift} \, E \, d\mathcal{S} \qquad \text{with } v_{drift} = \mu_e E \tag{2.19}$$

  where e^{-} is the value of the electric charge carried by the electrons (1.602×10^{-19} Cb), μ_e is the electron mobility, which varies as a function of the reduced electric field E/N, and N_e is the electron number density. E is the electric field which can be computed from Eq. (2.18), and $d\mathcal{S}$ is the cross-sectional area perpendicular to the electric field, as represented in Fig. 2.1. Fig. 2.2 shows a typical temporal evolution of the calculated discharge current from an imposed voltage, characteristic of a single nanosecond discharge pulse, reproduced from Tholin (2012).

Following the above-described characteristics, the discharge energy deposition rate per unit volume $P(t)$ is thus obtained by introducing Eqs. (2.18) and (2.19) into Eq. (2.17):

$$P(t) = e^{-} N_e(t) \mu_e E(t)^2 \tag{2.20}$$

The discharge energy power is, therefore, dependent on the temporal evolution of the pulse voltage $V(t)$ (in order to calculate the value of $E(t)$) and on the evolution of the electron number density N_e. To compute N_e it is necessary to solve the electron balance equation along with the ionized and excited species balance equations as described in the following

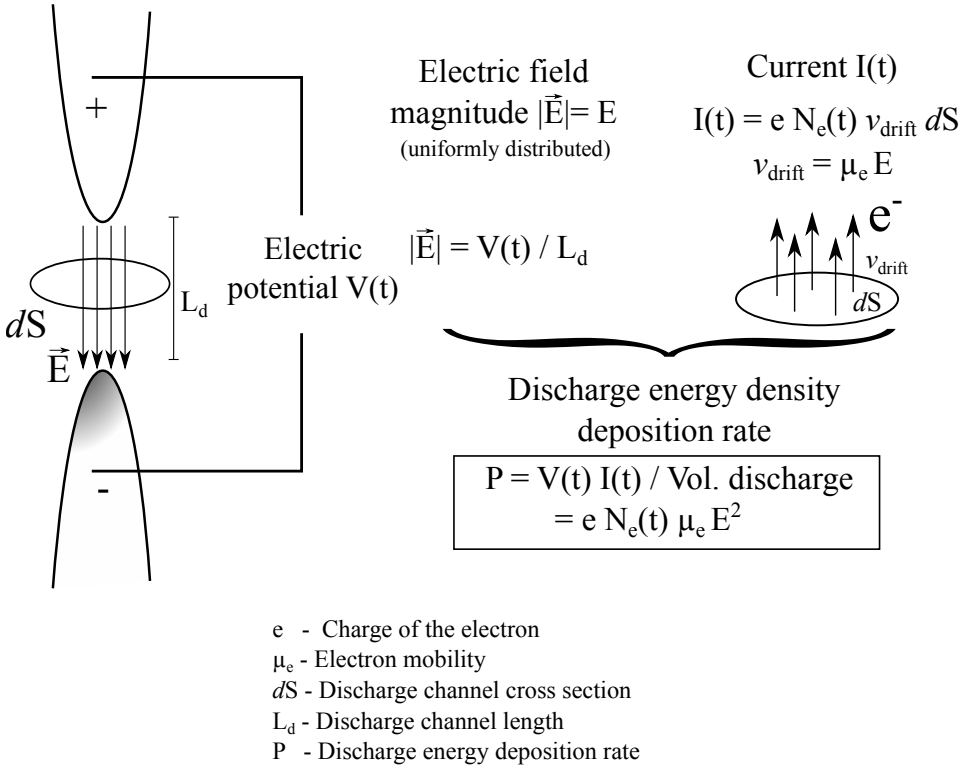

Figure 2.1: *Schematic representation of the discharge energy deposition rate model.*

section.

2.3.2 Electrons and excited species balance equations

The balance equation for the electrons, and each of the excited, ionized and ground state species can be written as Eq. (2.4):

$$\frac{\partial(\rho Y_k)}{\partial t} + \frac{\partial(\rho u_i Y_k)}{\partial x_i} = -\frac{\partial(\rho V_{k,i} Y_k)}{\partial x_i} + W_k \dot{\omega}_k^{c+p} \tag{2.21}$$

The difference between Eq. (2.4) and Eq. (2.21) is the kinetic model used to compute the species source terms $\dot{\omega}_k^c$ and $\dot{\omega}_k^{c+p}$. As discussed in the previous section, the molar production rate $\dot{\omega}_k^c$ refers to the combustion-related reactions. The molar production rate $\dot{\omega}_k^p$, on the other hand, corresponds to the plasma-related reactions. The overall molar production

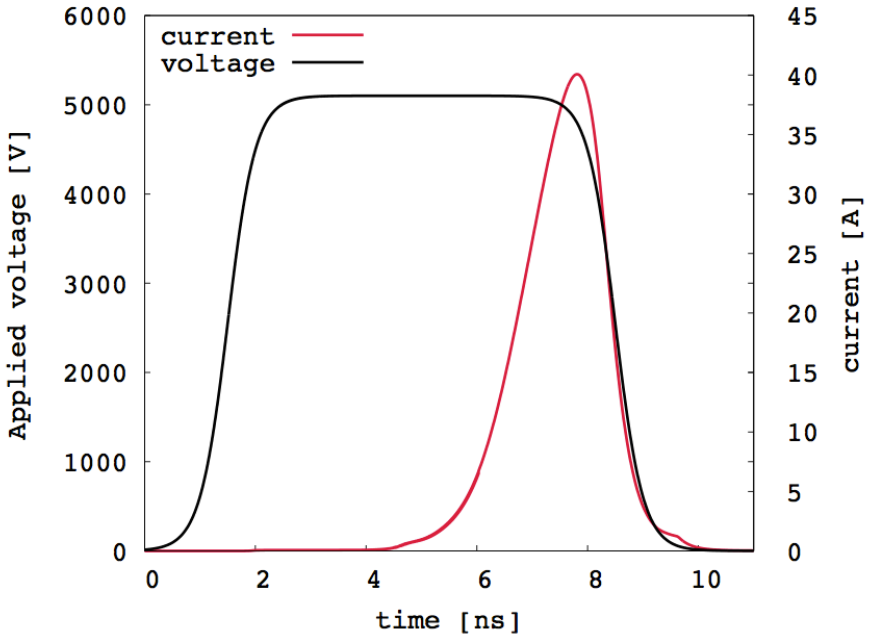

Figure 2.2: *Typical voltage model for a discharge with applied voltage of 5.1 kV, a maximum conductive current of 40 A and a pulse duration of 10 ns with a rise and a decrease time of 2 ns. Reproduced from Tholin (2012).*

rate $\dot{\omega}_k^{c+p}$ in Eq. (2.21) refers, therefore, to two different kinetic models corresponding to plasma-related reactions and to combustion-related reactions.

2.3.3 Kinetic models for plasma-assisted combustion

As an example, Fig. 2.3 shows the plasma-related reactions used by Bak et al. (2012) to perform 2-D computations of plasma-assisted flame stabilization of a methane/air mixture. The reduced plasma kinetic mechanism, which comprises 51 reactions and 10 excited and ionized species and electrons, is coupled with the skeletal combustion mechanism DRM19 containing 19 ground state species. As shown in Fig. 2.3, the plasma kinetic mechanism includes the following types of reactions and their corresponding rate constants:

- **Electron-impact ionization, dissociation and excitation of ground**

and ionized species:
The rate constants associated with these reactions depend on the electron energy distribution function (EEDF). They are calculated directly as a function of the reduced electric field E/N by solving the Boltzmann equation to obtain the EEDF. A two-term approximation solver for the Boltzmann equation, BOLSIG+ Bolsig (2005) is often used to this end, where the collision cross-sections are the input data. These collision cross-sections are available in the LxCat online database. Following this methodology, the reaction rates and the swarm parameters such as the electron mobility μ_e needed in Eq. (2.19) can finally be tabulated, as a function of the reduced electric field E/N, earlier computed in Eq. (2.18).

• **Ion-related reactions:**
- Ions conversion, recombination of electrons with positive ions;
The rate constants involving ions are widely available in the literature or can be adapted from these literature values. They are also calculated as a function of the electron temperature in the case of electron/ positive ions recombination/ionization, or as a function of the overall gas temperature T_g for charge transfer reactions. The electron temperature is that determined as a function of the reduced electric field using BOLSIG+.

• **Excited molecule-related reactions:**
- Quenching of excited states by ground state molecules;
Rate constants involving molecules in excited states are still an ongoing research field. The available rate constants are either constant values or dependent on the overall gas temperature T_g.

These detailed plasma kinetic mechanisms are then coupled with combustion mechanisms to compute the molar production rate $\dot{\omega}_k^{c+p}$ via the species balance equations. However, an important point of discussion is whether the combustion mechanisms are able to incorporate the outcome of the plasma-induced reactions. Combustion mechanisms are built for a certain gas temperature range and fuel composition, but plasma intro-

	Reaction	Rate coefficient
Electrons related reactions	$N_2 + e \rightarrow N_2(A) + e$	σ
	$N_2 + e \rightarrow N_2(B) + e$	σ
	$N_2 + e \rightarrow N_2(a') + e$	σ
	$N_2 + e \rightarrow N_2(C) + e$	σ
	$N_2 + e \rightarrow N_2^+ + 2e$	σ
	$O_2 + e \rightarrow 2O + e$	σ
	$O_2 + e \rightarrow O_2^+ + 2e$	σ
	$CH_4 + e \rightarrow CH_3 + H + e$	σ
	$CH_4 + e \rightarrow CH_4^+ + 2e$	σ
	$H_2O + e \rightarrow H_2O^+ + 2e$	σ
	$CO_2 + e \rightarrow CO_2^+ + 2e$	σ
Ions related reactions	$O_2^+ + e \rightarrow 2O$	$2 \times 10^{-7} (300/T_e)^{0.63}$ cm^3/s
	$CH_4^+ + e \rightarrow CH_3 + H$	$2.9 \times 10^{-7} (300/T_e)^{0.53}$ cm^3/s
	$H_2O^+ + e \rightarrow O + 2H$	$10^{-6} (300/T_e)^{0.5}$ cm^3/s
	$CO_2^+ + e \rightarrow O + CO$	$4 \times 10^{-7} (300/T_e)^{0.5}$ cm^3/s
	$e + e + N_2^+ \rightarrow e + N_2$	$10^{-19} (300/T_e)^{4.5}$ cm^6/s
	$e + N_2^+ + N_2 \rightarrow N_2 + N_2$	$6 \times 10^{-27} (300/T_e)^{1.5}$ cm^6/s
	$e + N_2^+ + O_2 \rightarrow N_2 + O_2$	$6 \times 10^{-27} (300/T_e)^{1.5}$ cm^6/s
	$e + e + O_2^+ \rightarrow e + O_2$	$10^{-19} (300/T_e)^{4.5}$ cm^6/s
	$e + O_2^+ + N_2 \rightarrow O_2 + N_2$	$6 \times 10^{-27} (300/T_e)^{1.5}$ cm^6/s
	$e + O_2^+ + O_2 \rightarrow O_2 + O_2$	$6 \times 10^{-27} (300/T_e)^{1.5}$ cm^6/s
	$e + e + H_2O^+ \rightarrow e + H_2O$	$10^{-19} (300/T_e)^{4.5}$ cm^6/s
	$e + H_2O^+ + N_2 \rightarrow H_2O + N_2$	$6 \times 10^{-27} (300/T_e)^{1.5}$ cm^6/s
	$e + H_2O^+ + O_2 \rightarrow H_2O + O_2$	$6 \times 10^{-27} (300/T_e)^{1.5}$ cm^6/s
	$e + e + CO_2^+ \rightarrow e + CO_2$	$10^{-19} (300/T_e)^{4.5}$ cm^6/s
	$e + CO_2^+ + N_2 \rightarrow CO_2 + N_2$	$6 \times 10^{-27} (300/T_e)^{1.5}$ cm^6/s
	$e + CO_2^+ + O_2 \rightarrow CO_2 + O_2$	$6 \times 10^{-27} (300/T_e)^{1.5}$ cm^6/s
	$N_2^+ + O_2 \rightarrow O_2^+ + N_2$	$6 \times 10^{-11} (300/T_g)^{0.5}$ cm^3/s
	$N_2^+ + H_2O \rightarrow H_2O^+ + N_2$	2.3×10^{-9} cm^3/s
	$H_2O^+ + O_2 \rightarrow O_2^+ + H_2O$	4.3×10^{-10} cm^3/s
	$CO_2^+ + O_2 \rightarrow O_2^+ + CO_2$	5.6×10^{-11} cm^3/s
Excited molecules related reactions	$N_2(A) + N_2 \rightarrow N_2 + N_2$	3×10^{-16} cm^3/s
	$N_2(B) + N_2 \rightarrow N_2 + N_2$	2×10^{-12} cm^3/s
	$N_2(B) + N_2 \rightarrow N_2(A) + N_2$	3×10^{-11} cm^3/s
	$N_2(B) \rightarrow N_2(A) + h\nu$	1.5×10^5 1/s
	$N_2(a') + N_2 \rightarrow N_2(B) + N_2$	1.9×10^{-13} cm^3/s
	$N_2(C) + N_2 \rightarrow N_2(a') + N_2$	10^{-11} cm^3/s
	$N_2(C) \rightarrow N_2(B) + h\nu$	3×10^7 1/s
	$N_2(A) + N_2(A) \rightarrow N_2(B) + N_2$	3×10^{-10} cm^3/s
	$N_2(A) + N_2(A) \rightarrow N_2(C) + N_2$	1.5×10^{-10} cm^3/s
	$N_2(A) + O_2 \rightarrow N_2 + 2O$	2.3×10^{-12} cm^3/s
	$N_2(B) + O_2 \rightarrow N_2 + 2O$	2×10^{-10} cm^3/s
	$N_2(a') + O_2 \rightarrow N_2 + 2O$	2.8×10^{-11} cm^3/s
	$N_2(C) + O_2 \rightarrow N_2 + 2O$	3×10^{-10} cm^3/s
	$N_2(A) + O \rightarrow N_2 + O$	2.1×10^{-11} cm^3/s
	$O + O + N_2 \rightarrow O_2 + N_2$	$10^{-33} (300/T_g)^{0.41}$ cm^6/s
	$O + O + O_2 \rightarrow O_2 + O_2$	$4 \times 10^{-33} (300/T_g)^{0.41}$ cm^6/s
	$CH_4 + N_2(A) \rightarrow CH_3 + H + N_2$	3.3×10^{-15} cm^3/s
	$CH_4 + N_2(B) \rightarrow CH_3 + H + N_2$	3×10^{-10} cm^3/s
	$CH_4 + N_2(a') \rightarrow CH_3 + H + N_2$	3×10^{-10} cm^3/s
	$CH_4 + N_2(C) \rightarrow CH_3 + H + N_2$	5×10^{-10} cm^3/s

Figure 2.3: *Example of the set of plasma-related reactions used in detailed plasma-assisted combustion models. The notation σ indicates that an electron impact cross-section σ is used in BOLSIG+ to determine the rate coefficient. Reproduced from Bak et al. (2012)*

duces many radicals early after the discharge at relatively low gas temperature conditions, that are outside of the temperature range for which the combustion mechanisms are valid. Therefore, the combustion mechanisms may not be suitable to the new highly reactive and low temperature gas conditions. For example, measurements in a low temperature flow reactor and 0-D numerical simulations were performed to study the methane/air low temperature oxidation during a nanosecond repetitively pulsed discharge in Lefkowitz et al. (2015). Although the model could accurately predict the fuel consumption and the production of major species such as H_2O, CO, CO_2, the model over-predicted the concentration of CH_3OH by an order of magnitude and the one of CH_2O by a factor of 4. The authors argued that the reaction of CH_2O with singlet oxygen $O(^1D)$, which was not considered in the kinetic mechanism, could play an important role on the CH_2O concentration predictions.

Along with the uncertainties related to the reaction rates of the kinetic model, detailed plasma kinetic models also increase the number of species and, therefore, the number of equations to solve during the numerical simulations. This increases greatly the computational cost associated with the DNS of plasma-assisted combustion. To illustrate this, in Appendix A an estimation of the computational costs of 2-D DNS and 3-D DNS is given as a function of the number of species considered in the kinetic mechanism.

The following sections of this chapter are dedicated to the development of a new plasma-assisted combustion model. As will shortly become clear, detailed plasma kinetic mechanism are not considered in the new model. This new modeling strategy reduces the uncertainties associated with the rate constants of plasma-related reactions. Finally, it enables a pragmatic study of the complex physics underlying the plasma-assisted combustion/ ignition phenomena that have not yet been examined in the literature.

2.4 Phenomenological plasma-assisted combustion model

Based on the simulation and experimental results reported in the literature, the new plasma model is constructed by analyzing the distribution of the electrical power over the different internal energy modes of molecules and the channels through which these excited states impact the thermochemical state of the gas when they relax.

2.4.1 Population of specific internal modes

Figures 2.4a and b show the results of 0-D computations of the discharge energy distribution over different internal modes of molecules as a function of the reduced electric field E/N (Starikovskiy and Aleksandrov (2013)). For these computations, a detailed plasma kinetic model coupled with a Boltzmann solver was used.

It is shown that, for values of E/N in the range 100 - 400 Td (1 Td = 10^{-17} Vcm^2), the electrons accelerated by the electric field mainly produce electronically ($A^3\sum_u^+$, $B^3\Pi_g$, $C^3\Pi_u$, a'$^1\sum_u^-$ ...) and vibrationally excited molecular nitrogen. The distribution of the electric energy over these excited states of N_2 is also shown in Nighan (1970) and Aleksandrov et al. (1981). Additional channels include processes such as electron-impact ionization, excitation of molecular oxygen, dissociation of molecular oxygen into ground (O^3P) and excited (O^1D) oxygen atoms, and dissociation of fuel molecules.

Figure 2.4a shows that, among these excitation and dissociation processes, those that consume most of the energy (about 90% of the discharge energy) are the ones associated with the population of vibrational and electronic states of N_2 molecules and the dissociation of O_2 molecules by direct electron impact. This is the case in air (Fig. 2.4a), but also to a large extent in hydrocarbon-air mixtures, since the mole fraction of hy-

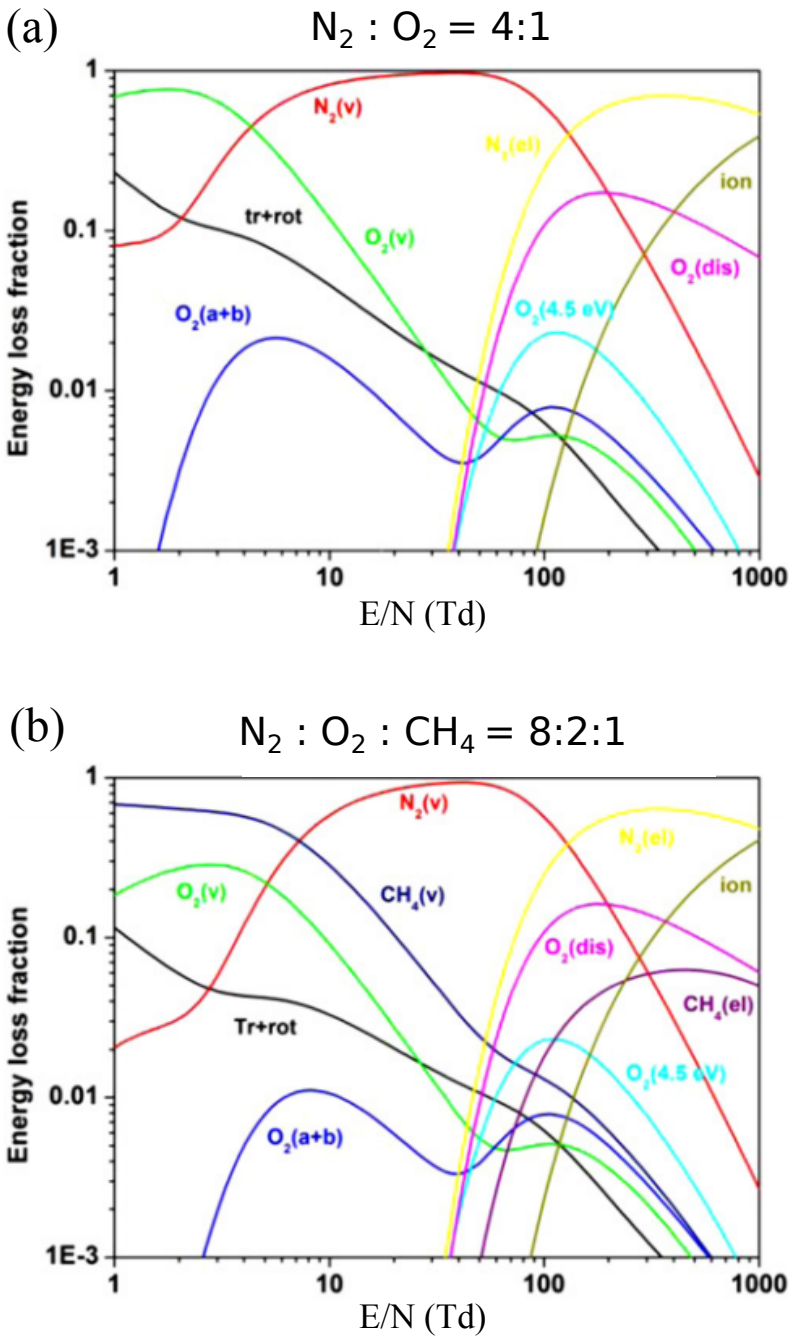

Figure 2.4: *Fractional power dissipated by electrons into various channels as a function of E/N. (a) Air; (b) methane-air stoichiometric mixture. Reproduced from Starikovskiy and Aleksandrov (2013).*

drocarbons represents only a small fraction of the mixture composition. Indeed, as shown in Fig. 2.4b, within the same range of values of E/N, the processes that consume most of the energy in a methane-air mixture are also the electronic and vibrational excitation of N_2 molecules as well as the dissociation of O_2 molecules through direct impact with the electrons. This is explained in part by the fact that, for instance, stoichiometric methane-air mixtures only contain 5.5% of methane in mass and, therefore, the collision probability of the electrons with N_2 is higher than with methane.

2.4.2 Modes of energy transferred into the gas

For values of E/N in the range 100 - 400 Td, the impact of the discharge energy on the combustion processes will be considered to be mostly associated with the impact of the vibrationally and electronically excited N_2 molecules as well as O atoms, on the mixture thermodynamics.

At the end of the discharge, the gas is in thermal non-equilibrium condition, which means that the temperatures of the excited N_2 molecules, such as the vibrational and electronic temperatures, are different from the translational temperature of the ground state molecules, defined as T_g. Electronically and vibrationally excited N_2 molecules eventually reach thermal equilibrium with the translational mode through collisional processes with ground state molecules. These processes are detailed next.

- **Electronic states of N_2 molecules:**

The mechanism of excitation and relaxation associated to electronic states N_2(A,B,C,a',...) is given by the following two-step reaction process (Popov (2001); Popov (2011a); Rusterholtz et al. (2013)):

$$N_2(X) + e^- \rightarrow N_2(A, B, C, a', ...) + e^- \tag{2.22}$$

$$N_2(A, B, C, a', ...) + O_2 \rightarrow 2O + N_2(X) + heat \tag{2.23}$$

In reaction 2.22, electrons e^- collide with ground state N_2 molecules N_2(X) exciting electronic states N_2(A,B,C,a',...). This reaction occurs within the discharge characteristic time scale when the electric field E is active. After the discharge, the relaxation of N_2(A,B,C,a',...) occurs mostly by dissociative quenching reactions with O_2 molecules, as represented by reaction 2.23. Reactions 2.22 and 2.23 ultimately result in ultrafast gas heating and ultrafast dissociation of O_2. The ultrafast gas heating and ultrafast dissociation of O_2 occur on time scales of a few tens of nanoseconds at atmospheric pressure. The details of this mechanism will be further discussed in subsequent sections.

• **Vibrational states of N_2 molecules:**

The vibrational excitation of N_2 molecules by electron-impact and the subsequent relaxation of these modes towards thermal equilibrium can be represented by the following mechanism:

$$N_2(X) + e^- \rightarrow N_2(v) + e^- \tag{2.24}$$

$$N_2(v) \rightarrow N_2(X) + heat \tag{2.25}$$

Reaction 2.24 also occurs within the discharge characteristic time scale, whereas the relaxation of vibrational states of N_2, through reaction 2.25, occurs on a much longer time scale and results in slow gas heating (Millikan and White (1963); Park (1993); Popov (2011a)).

According to this foregoing analysis, the two main channels through which the electrons produced during the discharge impact the gas are:

1) the excitation and the subsequent relaxation of electronic states of nitrogen molecules, leading to an ultrafast increase of gas temperature and species dissociation - reaction 2.23;

2) the excitation and relaxation of vibrational states of nitrogen molecules, causing a much slower gas heating - reaction 2.25.

Figure 2.5 shows a comparative schematic of the discharge energy pathways and the characteristic time scales found in detailed plasma models and in the phenomenological plasma model developed in this chapter. The energy transfer pathways represented by the black arrows refer to the detailed plasma models whereas the blue arrows refer to the new model.

In detailed models, excitation of electronic and vibrational states of N_2 occurs within the characteristic times τ_{electr} and τ_{vib} given by the rate constants of electron-impact reactions such as those of reactions 2.22 and 2.24, respectively. The energy stored in the electronic states of N_2 is then transferred to the gas as thermal and chemical energies. This process occurs at multiple characteristic time scales τ_{ET}, given by the quenching rates of each electronic state of N_2. Therefore, the contribution of the plasma to the increase of the gas thermal and chemical energies requires considering a number of excited states as well as several chemical time scales. Additional processes must be considered for the vibrationally excited N_2 which eventually produce a slower increase of the gas thermal energy.

The energy pathways represented in blue in Fig. 2.5 refer to the new modelling strategy where the plasma effects of ultrafast gas heating, ultrafast O_2 dissociation and slow gas heating, are captured without any additional electron-impact reactions or relaxation reactions. Thus, electronically and vibrationally excited N_2 are not modeled in the overall kinetic mechanism. The following sections give the major assumptions

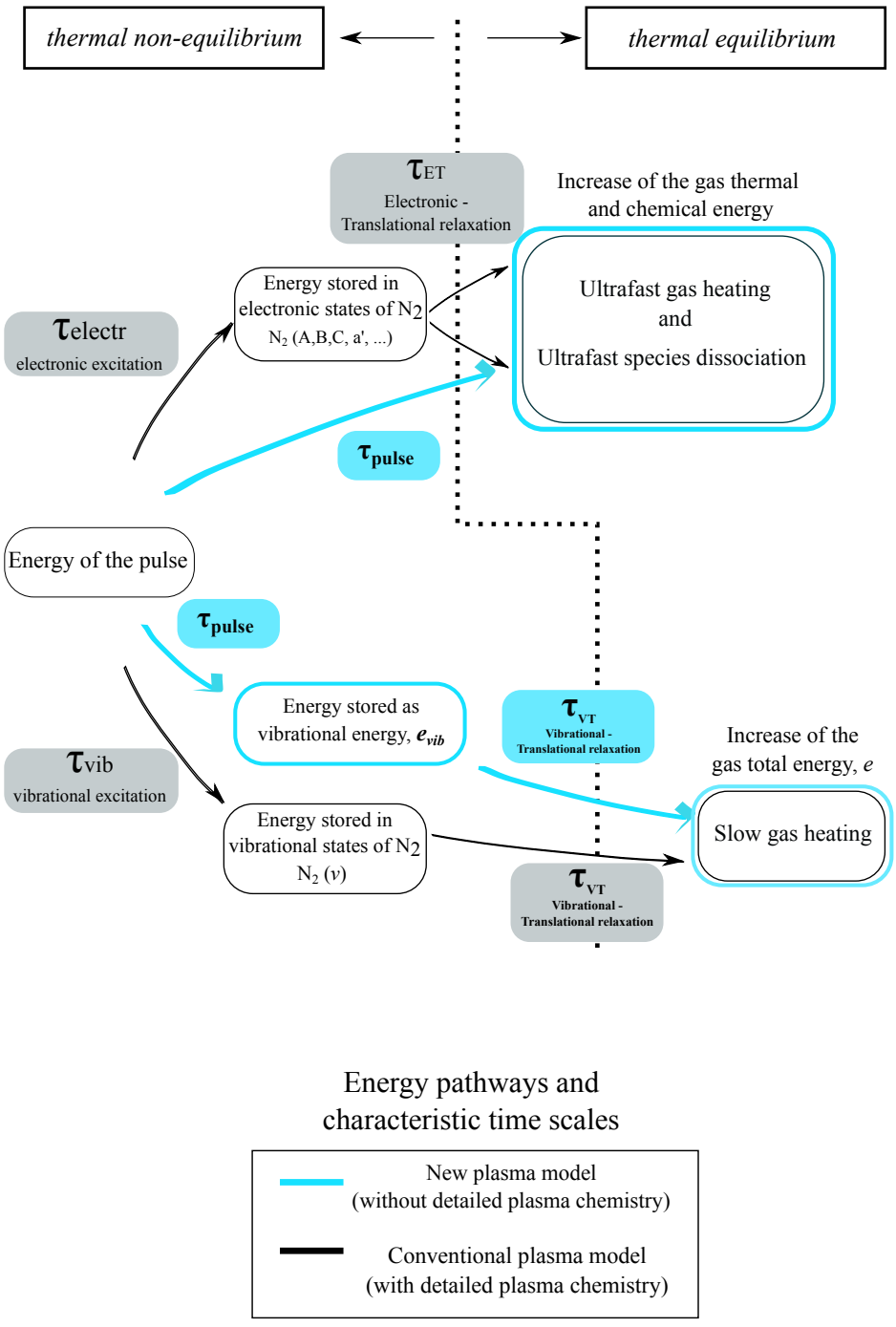

Figure 2.5: *Comparative schemes of the energy pathways and characteristic time scales considered in detailed plasma models and the ones considered in the present model. In the new model detailed plasma chemistry is by-passed.*

for this new modelling strategy.

2.4.3 Major assumptions

1. **Characteristic time scales:**

   The energy of the pulse is transferred to the gas total energy within two characteristic time scales, hereinafter referred as τ_{pulse} and τ_{VT}:

   - τ_{pulse}: The characteristic time scales of electron-impact reactions τ_{electr} and τ_{vib} (see Fig. 2.5) are of the order of the pulse duration, about 10 ns. The characteristic time scales of dissociative quenching reactions of electronic excited N_2 τ_{ET} are about 50 ns. Therefore, the model groups all these ultrafast processes into a single global process with a characteristic time scale $\tau_{pulse} \approx \tau_{ET}$.

   - τ_{VT}: is the characteristic time associated with slow processes and is of the order of the vibrational relaxation time of N_2 molecules (time scales of the order of 1-100 microseconds);

2. **Rate of discharge energy distribution**:

   Figure 2.6 shows a schematic representation of the rate of discharge energy distribution considered in the model. The impact of the discharge energy on the combustion governing equations (thermal equilibrium state) is captured by additional species and heat source terms.

   All the energy of the discharge is deposited within τ_{pulse} and leads to:

   - An ultrafast dissociation of certain species and, therefore to

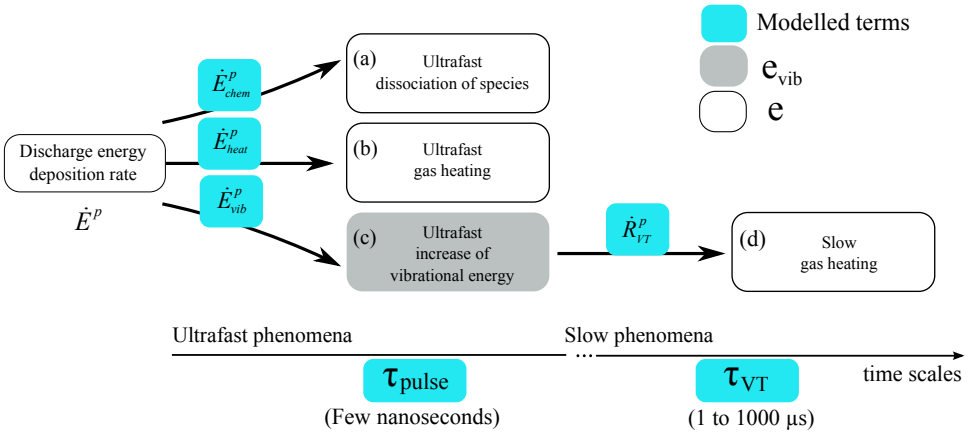

Figure 2.6: *Schematic representation of the energy source terms considered in the present model formulation. The discharge energy is assumed to be deposited into (a) gas chemical, (b) thermal and (c) vibrational energies within the pulse characteristic time τ_{pulse}. The relaxation of vibrational energy leads to (d) a slower increase of gas thermal energy within a characteristic time τ_{VT}.*

the change of the chemical energy of the gas at a rate $\dot{E}^p_{chem}$;

- An ultrafast increase of the gas temperature leading to an increase of the sensible energy at a rate $\dot{E}^p_{heat}$;
- An ultrafast increase of the vibrational energy of the gas at a rate $\dot{E}^p_{vib}$.

The discharge energy deposition rate per unit volume, referred as $\dot{E}^p$, can therefore be written as the sum of three contributions:

$$\dot{E}^p = \dot{E}^p_{chem} + \dot{E}^p_{heat} + \dot{E}^p_{vib} \tag{2.26}$$

In the present model we assume that vibrational energy is stored in a single energy variable e_{vib}. This strategy avoids including multiple states of vibrationally excited N_2 molecules in the kinetic mechanism.

The contributions $\dot{E}^p_{chem}$ and $\dot{E}^p_{heat}$ are directly added to the energy equation, Eq. (2.3), since the total energy, e, is defined as the sum of

chemical, sensible and kinetic energies, and because the characteristic time of these energy deposition rates, τ_{pulse}, is extremely small compared with the flow and combustion characteristic times. On the other hand, the vibrational contribution $\dot{E}^p_{vib}$ cannot be considered directly in the energy balance equation as it impacts the gas total energy only when it relaxes into gas heating and its relaxation is a slow process. The foregoing analysis leads to the next assumption.

3. **Rate of vibrational energy deposition**

The vibrational energy e_{vib} is transferred into the gas total energy within τ_{VT} at a rate $\dot{R}^p_{VT}$ (see Fig. 2.6).
The vibrational modes of N_2 molecules eventually reach thermal equilibrium with the translational mode within a characteristic time τ_{VT}. In Millikan and White (1963) and Park (1993), τ_{VT} of N_2 molecules was studied for a wide range of gas temperatures and atomic and molecular oxygen concentrations. The results showed that τ_{VT} is very sensitive to the partial pressure of atomic oxygen and the mixture temperature. Therefore, in turbulent reactive flow conditions, τ_{VT} may vary significantly depending on the local conditions of mixture temperature and species concentrations. If τ_{VT} is of the same order as the flow characteristic time, the vibrational energy is transported by the flow while heating up the gas mixture. Therefore, an additional transport equation for the vibrational energy e_{vib} is considered in the present formulation to close the relaxation rate of the vibrational energy $\dot{R}^p_{VT}$.

The transport equation for the vibrational energy e_{vib}, is then written as follows:

$$\frac{\partial(\rho e_{vib})}{\partial t} + \frac{\partial(\rho u_i e_{vib})}{\partial x_i} = \frac{\partial}{\partial x_i}\left(\rho \mathcal{D} \frac{\partial e_{vib}}{\partial x_i}\right) + \dot{E}^p_{vib} - \dot{R}^p_{VT} \quad (2.27)$$

where $\dot{E}^p_{vib}$ is the discharge power that increases the vibrational energy of the gas within τ_{pulse} (see Fig. 2.6). As most of the vibrational energy is carried by N_2 molecules, the diffusion coefficient $\mathcal{D}$ is assumed to be equal to that of N_2 molecules.

2.4.4 Plasma-assisted combustion model equations

Accordingly, the proposed set of balance equations to model NRP discharges in reactive mixtures is as follows:

$$\frac{\partial \rho}{\partial t} + \frac{\partial (\rho u_i)}{\partial x_i} = 0 \tag{2.28}$$

$$\frac{\partial (\rho u_j)}{\partial t} + \frac{\partial (\rho u_i u_j)}{\partial x_i} = -\frac{\partial p}{\partial x_j} + \frac{\partial \tau_{ij}}{\partial x_i} \tag{2.29}$$

$$\frac{\partial (\rho e)}{\partial t} + \frac{\partial (\rho u_i e)}{\partial x_i} = -\frac{\partial q_i}{\partial x_i} + \frac{\partial (\sigma_{ij} u_i)}{\partial x_i} + \dot{E}^p_{chem} + \dot{E}^p_{heat} + \dot{R}^p_{VT} \tag{2.30}$$

$$\frac{\partial (\rho e_{vib})}{\partial t} + \frac{\partial (\rho u_i e_{vib})}{\partial x_i} = \frac{\partial}{\partial x_i}\left(\rho \mathcal{D} \frac{\partial e_{vib}}{\partial x_i}\right) + \dot{E}^p_{vib} - \dot{R}^p_{VT} \tag{2.31}$$

$$\frac{\partial (\rho Y_k)}{\partial t} + \frac{\partial (\rho u_i Y_k)}{\partial x_i} = -\frac{\partial (\rho V_{k,i} Y_k)}{\partial x_i} + W_k \dot{\omega}^c_k + W_k \dot{\omega}^p_k \tag{2.32}$$

Eqs. (2.28-2.30) and (2.32) correspond to Eqs. (2.1-2.4), with the additional plasma source terms. In Eq. (2.32), $\dot{\omega}^p_k$ is the molar production rate associated with the ultrafast species dissociation by the plasma discharge. The models for $\dot{E}^p_{chem}$, $\dot{E}^p_{heat}$, $\dot{E}^p_{vib}$, $\dot{R}^p_{VT}$ and $\dot{\omega}^p_k$ are discussed below.

2.4.5 General description of the model

- **Ultrafast species dissociation and temperature increase - models for $\dot{E}^p_{heat}$, $\dot{E}^p_{chem}$ and $\dot{\omega}^p_k$:**

  The distribution of the discharge power $\dot{E}^p$ over $\dot{E}^p_{chem}$ and $\dot{E}^p_{heat}$ depends on the local species concentrations $X_{k=1,..,N_{sp}}$, the temperature T, and the pressure p of the gas mixture prior to the pulse. The fractions $\dot{E}^p_{chem}$ and $\dot{E}^p_{heat}$ of the discharge energy deposition rate $\dot{E}^p$ can be expressed as follows:

$$\dot{E}^p_{heat} = g_{heat}\left(X_{k=1,..,N_{sp}}, T, p\right) \cdot \dot{E}^p \tag{2.33}$$

$$\dot{E}^p_{chem} = g_{chem}\left(X_{k=1,..,N_{sp}}, T, p\right) \cdot \dot{E}^p \tag{2.34}$$

where g_{heat} and g_{chem} are the fractions of the discharge energy transferred into sensible and chemical energy, respectively.
On the other hand, $\dot{E}^p_{chem}$ corresponds to the ultrafast dissociation of species and can be expressed in terms of the rate of production of species k, $\dot{\omega}^p_k$, associated with the plasma chemical processes occurring during the pulse:

$$\dot{E}^p_{chem} = \sum_{k=1}^{N_{sp}} e_k \, W_k \, \dot{\omega}^p_k \tag{2.35}$$

where e_k is the energy of species k.

For each species k, $e_k \dot{\omega}^p_k$ corresponds to a fraction g^k_{chem} of the discharge power and reads:

$$e_k \, W_k \, \dot{\omega}^p_k = g^k_{chem}\left(X_{k=1,..,N_{sp}}, T, p\right) \cdot \dot{E}^p \tag{2.36}$$

and

$$g_{chem} = \sum_{k=1}^{N_{sp}} g^k_{chem} \tag{2.37}$$

The rate of production of the k^{th} species during the pulse can then be written as:

$$\dot{\omega}^p_k = g^k_{chem}\left(X_{k=1,..,N_{sp}}, T, p\right) \cdot \frac{\dot{E}^p}{e_k \, W_k} \tag{2.38}$$

- **Vibrational energy increase and its relaxation - models for $\dot{E}^p_{vib}$ and $\dot{R}^p_{VT}$:**

The rate of increase of vibrational energy, $\dot{E}^p_{vib}$, is given by the

fraction of the discharge power that is not transferred into $\dot{E}^p_{heat}$ and $\dot{E}^p_{chem}$ within τ_{pulse}. From Eqs. (2.26), (2.33) and (2.34), $\dot{E}^p_{vib}$ is therefore expressed as:

$$\dot{E}^p_{vib} = [1 - (g_{heat} + g_{chem})] \cdot \dot{E}^p \tag{2.39}$$

The relaxation rate of the vibrational energy into total energy, $\dot{R}^p_{VT}$, depends on the local species concentration, $X_{k=1,..,N_{sp}}$, temperature T, and pressure p, and also on the local vibrational energy e_{vib}. $\dot{R}^p_{VT}$ can be expressed as follows:

$$\dot{R}^p_{VT} = f\left(X_{i=1,..,N_{sp}}, T, p, e_{vib}\right) \tag{2.40}$$

Once the functions g_{heat}, g^k_{chem}, f and $\dot{E}^p$ are known, the terms $\dot{E}^p_{chem}$, $\dot{E}^p_{heat}$ and $\dot{R}^p_{VT}$ in the energy balance equation Eq. (2.30), as well as $\dot{\omega}^p_k$ in the species balance equation Eq. (2.32) and $\dot{E}^p_{vib}$ in the vibrational energy balance equation Eq. (2.31) are closed. These functions can be deduced either from detailed plasma kinetic simulations or from semi-empirical models. In the following section, an analytical closure is proposed for the above general functions g_{heat}, g^k_{chem} and f based on the experimental and simulation values discussed in the literature.

2.5 Model closures

As previously discussed, the excited electronic states of N_2 are rapidly quenched, mostly by dissociative quenching reactions with O_2, which take place in time scales of the order of a few nanoseconds at atmospheric pressure. The mechanism is given by the following reactions, already mentioned in section 2.4.2 and recalled here for convenience :

$$N_2(X) + e^- \rightarrow N_2(A, B, C, a', ...) + e^- \tag{2.41}$$

$$N_2(A, B, C, a', ...) + O_2 \rightarrow 2O + N_2(X) + heat \tag{2.42}$$

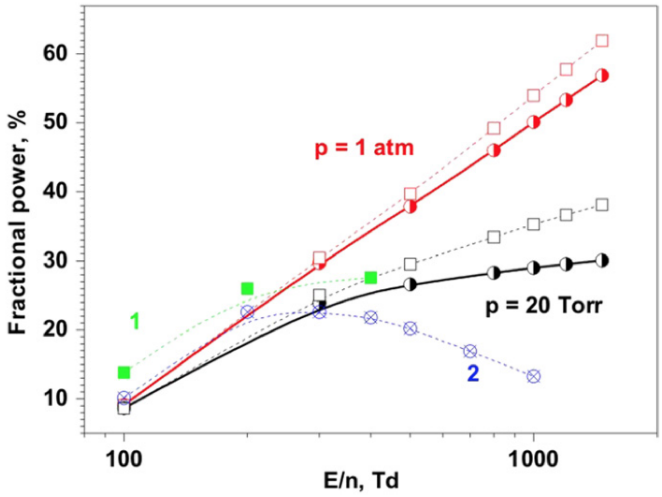

Figure 2.7: *The fraction of the total electron power transferred into heat in dry air at 20 Torr and 1 atm as a function of the reduced electric field at which the energy was deposited in a high-voltage nanosecond discharge. The calculations were carried out for* $n_{ef} = 10^{15}$ cm^{-3} *(solid curves) and* 10^{14} cm^{-3} *(dash curves). Curve 1 corresponds to calculations of Flitti and Pancheshnyi (2009) and curve 2 corresponds to the calculations of Popov (2001) assuming that 28% of the energy that was spent on the excitation of electronic* N_2 *and* O_2 *states was quickly transferred into gas heating. Reproduced from Aleksandrov et al. (2010).*

where, N_2(A,B,C,a',...) refers to the electronic excited states and N_2(X) the ground state of N_2 molecules. This two-step mechanism, which is an extension of the one proposed by Popov (2001) results in ultrafast heating of the gas and ultrafast dissociation of O_2. Figure 2.7 shows a comparative analysis of the 0-D numerical simulations performed by various authors (Popov (2001), Flitti and Pancheshnyi (2009) and Aleksandrov et al. (2010)) of the fraction of the total electron power transferred into fast heating, in dry air at 20 Torr and 1 atm, as a function of the reduced electric field. It is shown that 10 to 30% of the electron energy is transferred into ultrafast gas heating for 100 < E/N < 400 Td at atmospheric pressure. This is in agreement with the experimental observations of Rusterholtz et al. (2013) who determined a fraction of about 20±5% in that same range of reduced electric fields.

The second important parameter is the fraction of energy going into O_2 dissociation. The dissociation energy of O_2 is about 5.2 eV, and the energies of the $N_2(B)$ and $N_2(C)$ states, which are the main contributors to the ultrafast mechanism, are about 7.4 eV and 11 eV, respectively. Thus, for reaction (2.42) with $N_2(B)$, the ratio of energy going into dissociation (5.2 eV) over the energy going into heating (7.4-5.2 = 2.2 eV) is approximately 2.4. For $N_2(C)$, this ratio is about 0.9. It is therefore expected that the overall ratio will lie between these two values, but closer to the high end of the range because of the higher population of $N_2(B)$. In the experiments of Rusterholtz et al. (2013) and simulations of Popov (2013), this ratio was found to be about 1.75 (35±5% into dissociation and 20±5% into heating), which is consistent with the foregoing analysis. Thus, this model will be based on the experimental and simulation values of 35% of energy going into ultrafast dissociation, and 20% into ultrafast heating. Finally, it is considered that the rest of the discharge energy, i.e. about 45%, is spent on the vibrational excitation of N_2 by electron impact. The energy stored in vibrational states of N_2 will then impact the thermal-equilibrium system through a slow heat release.

Following these values and the models presented in section 2.4.5, we consider the following sub-models:

- **Ultrafast characteristic time τ_{pulse}**:

  The ultrafast characteristic time defined in the model as τ_{pulse}, is chosen to approximately represent the characteristic production time of O radicals ≈ 50 ns, as observed in the experimental work of Rusterholtz et al. (2013). Its exact value is not critical, as long as it is much shorter than the acoustic characteristic time scales (Vasquez-Espí and Liñan (2001));

- **Plasma processes and species reaction rates**:

Only the dissociation process $O_2 \rightarrow 2O$ occurs within τ_{pulse}. Therefore the species considered in Eq. (2.35) are only O_2 molecules and O radicals.
As the mass conservation of combustion species production is ensured by $\sum_{k=1}^{Nsp} M_k \dot{\omega}_k^c = 0$, the conservation of the mass of species involved in this plasma reaction implies:

$$\dot{\omega}_{O_2}^p = -\frac{W_O}{W_{O2}} \dot{\omega}_O^p \tag{2.43}$$

and

$$\dot{\omega}_k^p = 0 \qquad \text{if } k \neq O_2 \text{ , O} \tag{2.44}$$

- **Chemical energy deposition rate:**

Following Eqs. (2.34) and (2.36) the discharge energy consumed in the dissociation process is written as:

$$\dot{E}_{chem}^p = (g_{chem}^O + g_{chem}^{O_2})\, \dot{E}^p \tag{2.45}$$

$$= e_O\, W_O\, \dot{\omega}_O + e_{O_2}\, W_{O_2}\, \dot{\omega}_{O_2} \tag{2.46}$$

The reaction rate of O_2 dissociation involved in the plasma reaction depends on the available quantity of O_2, therefore g_{chem}^O is assumed to be proportional to the ratio $Y_{O_2}/Y_{O_2}^f$ where $Y_{O_2}^f$ represents the mass fraction of O_2 in the fresh mixture:

$$g_{chem}^O = \eta\, \frac{Y_{O_2}}{Y_{O_2}^f} \tag{2.47}$$

where η is the fraction of the discharge power leading to O_2 dissociation, with $\eta = 0.35$ as justified above.

From Eq. (2.38) the molar production rate $\dot{\omega}_O^p$ can then be expressed

by:

$$\dot{\omega}_O^p = \eta \frac{Y_{O_2}}{Y_{O_2}^f} \frac{\dot{E}^p}{e_O W_O} \tag{2.48}$$

This means that when all O_2 molecules are locally consumed, $\dot{\omega}_O^p$ will vanish.

Finally, introducing Eqs. (2.48) and (2.43) into Eq. (2.46) one obtains the expression for $\dot{E}_{chem}^p$:

$$\dot{E}_{chem}^p = \eta \frac{Y_{O2}}{Y_{O2}^f} \left(1 - \frac{e_{O_2}}{e_O}\right) \dot{E}^p \tag{2.49}$$

- **Thermal energy deposition rate:**

The sum of the power going into ultrafast dissociation ($\dot{E}_{chem}^p$) and ultrafast heating ($\dot{E}_{heat}^p$) is equal to the power going into the electronic excitation of N_2. Thus it is proportional to $\dot{E}^p$:

$$\dot{E}_{chem}^p + \dot{E}_{heat}^p = \alpha \dot{E}^p \tag{2.50}$$

In our model, we assume $\alpha = 0.55$ (i.e 0.35 for ultrafast dissociation plus 0.20 for ultrafast heating). By combining Eqs. (2.49) and (2.50), we have:

$$\dot{E}_{heat}^p = \left[\alpha - \eta \frac{Y_{O2}}{Y_{O2}^f} \left(1 - \frac{e_{O_2}}{e_O}\right)\right] \dot{E}^p \tag{2.51}$$

Therefore, the fraction $\dot{E}_{heat}^p$ increases when Y_{O_2} decreases, and reaches $\alpha \dot{E}^p$ when O_2 vanishes. This is physically reasonable because the relaxation of electronically excited N_2 will then occur by collisions with ground state N_2, which is still an ultrafast heating process with a characteristic time of 10-100 ns (*see* Tables 5 and 6 in Rusterholtz et al. (2013)).

- **Vibrational energy deposition rate**:

  The rate of vibrational energy increase, $\dot{E}_{vib}$ is given by substituting Eq. (2.50) into Eq. (2.26):

$$\dot{E}_{vib} = (1 - \alpha)\, \dot{E}^{p} \tag{2.52}$$

- **Vibrational energy relaxation rate**:

  The vibrational-translational energy exchange rate, $\dot{R}^{p}_{VT}$ in Eqs. (2.30) and (2.31) is modeled considering the Landau-Teller harmonic oscillator approach:

$$\dot{\mathrm{R}}^{p}_{VT} = \rho \frac{e_{vib} - e^{eq}_{vib}(T)}{\tau_{VT}} \tag{2.53}$$

  in which the equilibrium value of the vibrational energy at a given mixture temperature, $e^{eq}_{vib}(T)$, is defined as:

$$e^{eq}_{vib}(T) = \frac{r\,\Theta_1}{e^{\Theta_1/T} - 1} \tag{2.54}$$

  where $\Theta_1 = 3396$ K is the vibrational temperature corresponding to the first quantum vibrational state of N_2 and $r = R/W_{N_2}$, with R the gas constant and W_{N_2} the nitrogen molar mass. τ_{VT} is computed as a function of τ^{k}_{VT} given by the experimental correlation of Millikan and White (1963):

$$\tau_{VT} = \left(\frac{1}{\tau^{O}_{VT}} + \frac{1}{\tau^{O_2}_{VT}} + \frac{1}{\tau^{N_2}_{VT}} \right)^{-1} \tag{2.55}$$

$$\tau^{k}_{VT} = c/p_k \, \exp[a_k \, (T^{-1/3} - b_k) - 18.42] \tag{2.56}$$

  where τ^{k}_{VT} is the vibrational-translational relaxation time of N_2 molecules by the k^{th} collisional species partner (O_2, O and N_2). $c = 1$ atm·s, p_k is the partial pressure of the k^{th} species and a_k

and b_k are experimental constants depending on the k^{th} species (*see* Table 2.1).

Colliding species	a_k	b_k
N_2	221.0	0.029
O_2	229.0	0.0295
O	72.4	0.015

Table 2.1: *Vibrational constants a_k and b_k for kth species N_2, O_2 and O used in Eq. (2.56).*

2.5.1 Temporal and spatial distribution model for $\dot{E}^p$

The above model is characterized by two semi-empirical parameters α and η (Eqs. (2.50) and (2.49)), as well as by the temporal and spatial distribution function of the discharge energy deposition rate $\dot{E}^p$. Figure 2.8 shows a schematic relation of the pulses temporal parameters. The discharge energy deposition rate $\dot{E}^p$ is applied at a given frequency f, to simulate the repetitively pulsed regime of NRP discharges. Therefore, at each pulse, a given energy per unit volume, referred hereinafter as σ_{pulse}, is deposited inside the discharge volume within the characteristic τ_{pulse}. Given σ_{pulse} and assuming that this energy is uniformly deposited within the characteristic time, τ_{pulse}, the energy deposition power $\dot{E}^p$ can be modelled as follows:

$$\dot{E}^p(t_{per}, x_i) = \begin{cases} \frac{\sigma_{pulse}}{\tau_{pulse}} \cdot \mathcal{F} & \text{if } t_{per} \leq \tau_{pulse} \\ 0 & \text{if } t_{per} > \tau_{pulse} \end{cases} \tag{2.57}$$

where t_{per} refers to the time in the pulse referential (i.e. related to the beginning of each pulse, determined by the pulse frequency f). The spatial function $\mathcal{F}$ defines the shape and the location in the computational domain of the discharge energy deposition. Figure 2.9 shows a schematic representation of the multiple discharge channel spatial functions $\mathcal{F}$ that can be considered. For each discharge channel shape (number 1, 2 and 3 in Fig. 2.9), the function $\mathcal{F}$ defines the computational zone where the

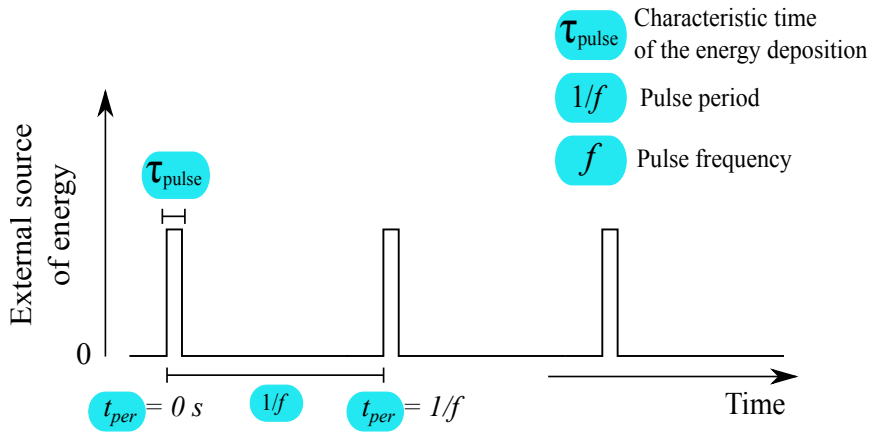

Figure 2.8: *Temporal parameters considered in the phenomenological model to set the frequency of the discharge energy deposition rate for simulations of nanosecond repetitively pulsed discharges.*

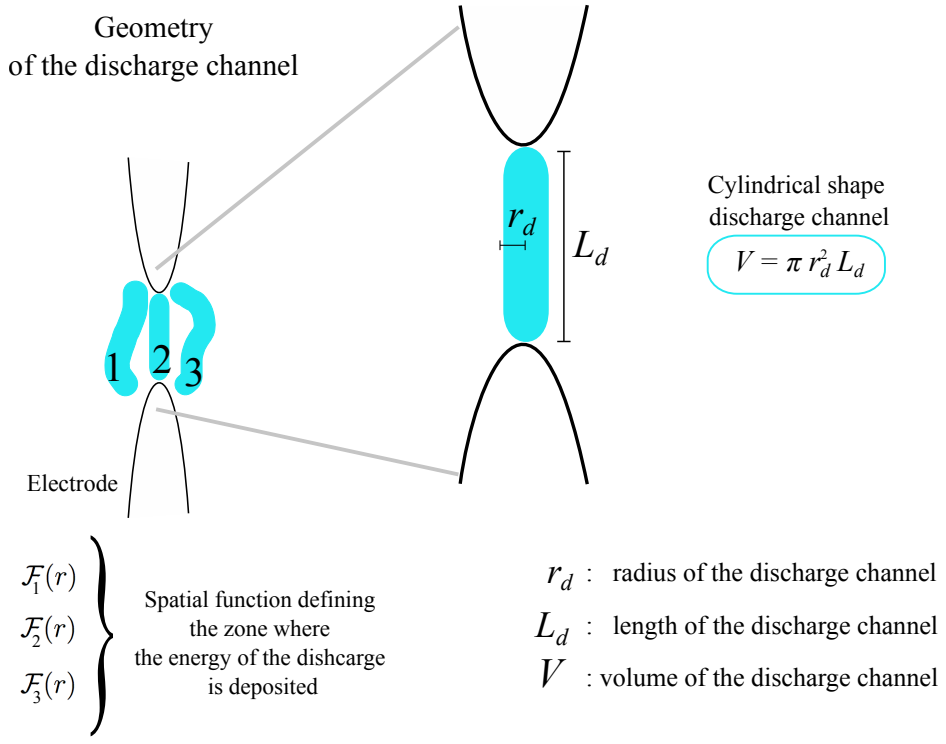

Figure 2.9: *Spatial parameters considered in the phenomenological model to set the shape and location of the discharge energy deposition rate in the computational domain.*

energy of the discharge will be deposited. It defines the value of σ_{pulse} given the discharge energy per pulse E_p as follows:

$$\sigma_{pulse} = \frac{E_p}{\iiint_{Channel} \mathcal{F}\, \mathrm{d}x\, \mathrm{d}y\, \mathrm{d}z} \tag{2.58}$$

In the present work, we considered that the discharge channel has always a cylindrical shape. Thus, the spatial function $\mathcal{F}$ is computed so that the volume of the discharge is given by $V = \pi r_d^2 L_d$, with r_d and L_d the characteristic radius and length of the discharge channel, respectively.

$$\iiint_{Channel} \mathcal{F}\, \mathrm{d}x\, \mathrm{d}y\, \mathrm{d}z = \pi r_d^2 L_d \tag{2.59}$$

Thus, from Eqs. (2.58) and (2.59) the value of σ_{pulse} is given by:

$$\sigma_{pulse} = \frac{E_p}{\pi r_d^2 L_d} \tag{2.60}$$

Note that r_d usually depends on the temperature and pressure (Naidis 2008). This dependency is neglected here but will be taken into account in future work.

2.5.2 Model validation

A preliminary test-case is performed to validate the model behaviour during a single discharge pulse. For this, 0-D simulations are compared with the experimental results obtained by Rusterholtz et al. (2013).

2.5.2.1 Experimental set-up and results

In Rusterholtz et al. (2013), nanosecond pulsed discharges were initiated in a flow of atmospheric pressure air preheated to 1000 K, between two pins separated by an inter-electrode gap distance of 4 mm. The gas was injected from the grounded cathode side with a velocity of 2.6 m/s. The high-voltage pulses of full width half maximum (FWHM) 10 ns duration,

pulse frequency $f = 10$ kHz and voltage $V = 5.7$ kV amplitude were produced by a FID Technology FPG 30-100MS pulse generator.

Figure 2.10 shows the temporal evolution of a) voltage, b) current, c) gas temperature and d) atomic oxygen density, measured in the steady-state pulse regime. The energy deposited per pulse was obtained by first multiplying the measured voltage and current signals and then by integrating in time over the pulse duration. The obtained value was about 670 ± 50 μJ. The plasma diameter was obtained based on the number density profiles of electronic excited nitrogen $N_2(B)$ and $N_2(C)$ species, shown in Fig. 2.11. A detailed description of the method can be found in Rusterholtz et al. (2013). The plasma channel diameter, defined as the FWHM of these density profiles, was approximately 450 ± 20 μm, at $t = 9$ ns after the beginning of the discharge.

2.5.2.2 Initial conditions, model parameters and 0-D equations

The 0-D simulations results are compared with the experimental results shown in Fig. 2.10. The considered initial conditions and the discharge energy density are the following:

Initial conditions

- gas temperature: $T = 1500$ K; This value is higher than the temperature of the preheated gas because previous pulses produce additional heating at steady state.
- pressure: $p = 1$ atm;
- At the beginning of the pulse about 15% of the O_2 has been dissociated by the previous discharges, therefore, the considered mole fractions of the mixture before each pulse are: $X_O = 0.063$, $X_{O_2} = 0.1785$ and $X_{N_2} = 0.7585$

Discharge energy density σ_{pulse}

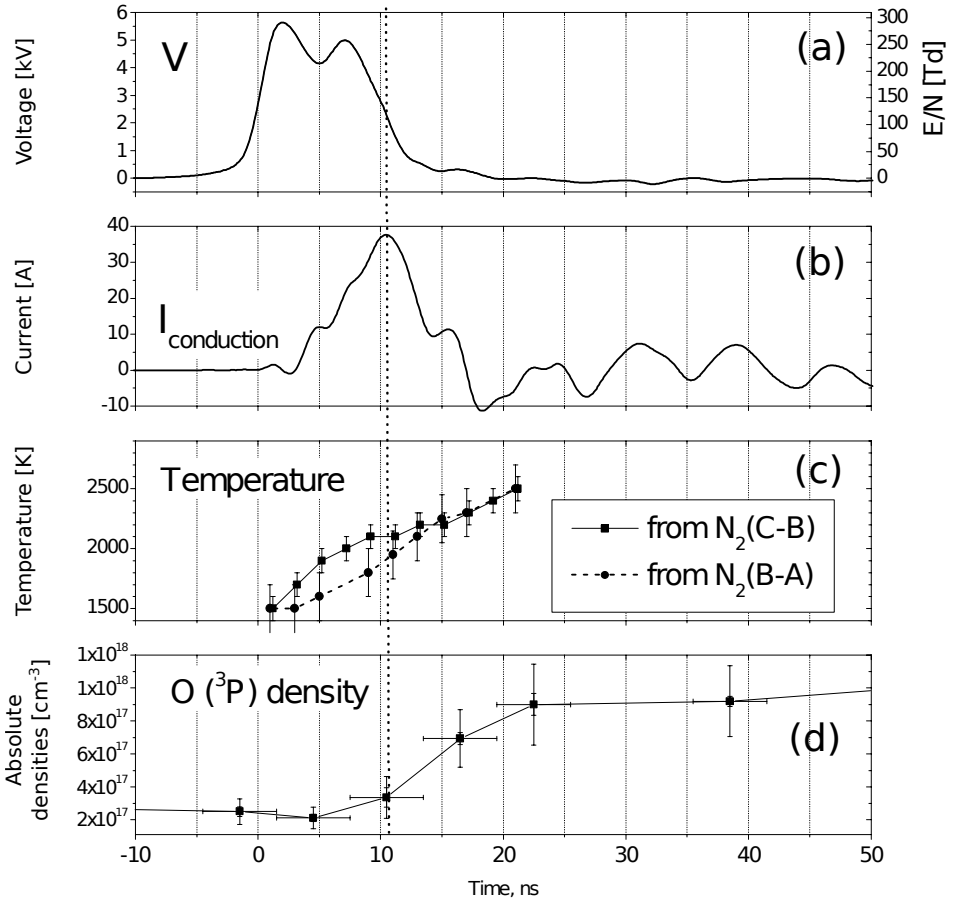

Figure 2.10: *Measurements of (a) pulse voltage and corresponding reduced electric field E/N, (b) conduction current, (c) temperature and (d) O density. These data were obtained for the reference conditions: atmospheric pressure air preheated at 1000 K, V = 5.7 kV, gap distance = 4 mm, pulse frequency = 10 kHz, air flow velocity = 2.6 ms^{-1} and energy per pulse = 670 ± 50 μJ. Reproduced from Rusterholtz et al. (2013).*

Assuming a cylindrical volume of the plasma channel $V_d = \pi {r_d}^2 L_d$, the discharge energy density is given by $\sigma_{pulse} = E_{pulse}/V_d = 1.05 \times 10^6$ J/m^3; where we considered the following values:

- discharge energy per pulse $E_{pulse} = 670$ μJ;
- discharge channel radius and length, $r_d = 225$ μm and $L_d = 4$ mm.

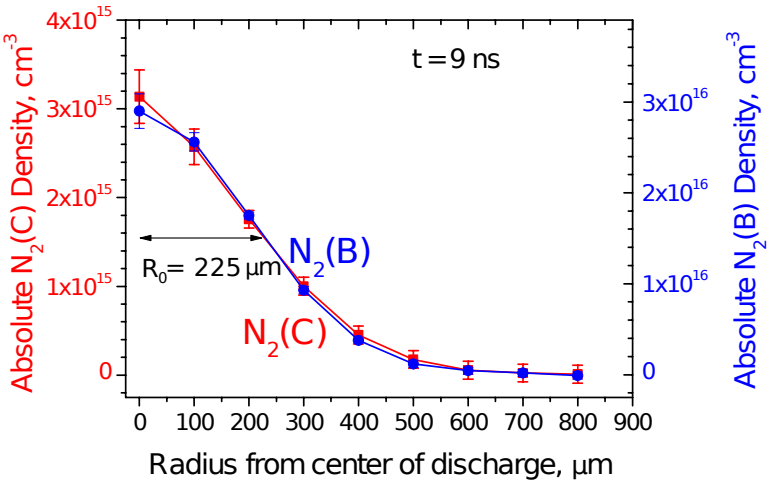

Figure 2.11: *Measured radial profiles at $t = 9$ ns of the $N_2(B)$ and $N_2(C)$ density. Reproduced from Rusterholtz et al. (2013).*

Model parameters α and η

As shown in Pai et al. (2010), the electric field is uniformly distributed inside the discharge channel for the NRP spark discharges considered in this work. Therefore, the reduced electric field E/N is obtained by:

$$\frac{E}{N} = \frac{V}{L_d\, N} \tag{2.61}$$

where $V = 5.7$ kV is the applied voltage, $L_d = 4$ mm is the inter-electrode gap distance and N is the number density of the gas given by $p/k_B T$, where p is the atmospheric pressure, k_B is the Boltzmann constant and T is the gas temperature. In the experimental work, during each pulse, the discharge energy is deposited within 10 ns, which is much shorter than the time scale of the gas expansion. Therefore, the process occurs at constant gas density with a value of the gas density $N = 4.9 \times 10^{18}$ cm^{-3} corresponding to the gas conditions of $p = 1$ atm and $T = 1500$ K, at the beginning of the pulse. For these conditions, the value of the reduced electric field $E/N = 290$ Td lies within the validity interval of the model ($100 < \mathrm{E/N} < 400$). For values of E/N in this range, the model parameter $\alpha = 0.55$ is retained but two values of the model parameter

η (0 and 0.35) are also analyzed to understand the impact of the early distribution of the discharge energy into $\dot{E}^p_{chem}$ and $\dot{E}^p_{heat}$.

0-D equations in REGATH solver

As discussed above, the gas density remains constant during the pulse so the process of the discharge energy deposition can be assumed to be a constant volume process. The model validation was performed with the 0-D REGATH solver (Candel et al. (2011)) which uses the same formalism as that of CHEMKIN.

During the first 100 nanoseconds only the ultrafast phenomena impact the species concentrations and gas temperature evolution. Therefore, the relaxation of the vibrational energy is not considered in the 0-D model. The temporal evolutions of the gas temperature T and of the O and O_2 mass fractions are obtained by solving the following equations:

$$\frac{\partial T}{\partial t} = \frac{1}{\rho C_v}\left[-\sum_{k=1}^{N_{sp}} \left\{ W_k(\dot{\omega}_k^{air} + \dot{\omega}_k^p)\, e_k \right\} + \underbrace{\dot{E}^p_{heat} + \dot{E}^p_{chem}}_{\substack{\text{from Eq. (2.50)} \\ \text{it is equal to } \alpha \dot{E}^p}} \right] \tag{2.62}$$

$$\frac{\partial Y_k}{\partial t} = \frac{W_k\,(\dot{\omega}_k^{air} + \dot{\omega}_k^p)}{\rho} \tag{2.63}$$

where the constant volume heat capacity C_v is given by:

$$C_v = \sum_{k=1}^{N_{sp}} Y_k C_{vk} \tag{2.64}$$

The molar production rate $\dot{\omega}_k^{air}$ refers to the reactions in the air kinetic mechanism with rate constants modelled by the standard Arrhenius equation. The plasma molar production rate $\dot{\omega}_k^p$ is given as follows:

$$\dot{\omega}_O^p = \eta \frac{\dot{E}^p}{e_O} \tag{2.65}$$

$$\dot{\omega}_{O_2}^p = -\frac{W_O}{W_{O_2}} \dot{\omega}_O^p \tag{2.66}$$

$$\dot{\omega}_k^p = 0 \qquad \text{if } k \neq \text{O, O}_2 \tag{2.67}$$

The discharge energy deposition rate $\dot{E}^p$ is given by:

$$\dot{E}^p(t) = \begin{cases} \frac{\sigma_{pulse}}{\tau_{pulse}} & \text{if } t \leq \tau_{pulse} \\ 0 & \text{if } t > \tau_{pulse} \end{cases} \tag{2.68}$$

where it is considered that τ_{pulse}= 50 ns and σ_{pulse} = 1.1 × 10^6 J/m^3 (as computed earlier at the beginning of this section).

2.5.2.3 Model results

Figure 2.12 shows the experimental and simulation results of the evolution of the gas temperature, pressure and O radical concentration during the pulse.

For the reference case, where η is set to 0.35 (meaning 35% of the pulse energy is routed to the dissociation of O_2), the pressure rises up to 2 atm, the temperature increases by about 1100 K, and O radical concentration rises from 0.3 up to 0.9×10^{18} particles/cm^3, as expected. The results are in good agreement with experimental values apart from the characteristic rise time of the gas temperature that was considered here equal to τ_{pulse} = 50 ns against the experimental value of 25 ns (shown in Fig. 2.10c). This value is a good compromise regarding the characteristic rise time of O radicals in the model and in the experiments (shown in Fig. 2.10d) and since we are only considering a single step τ_{pulse} to capture all the plasma reactions characteristic time scales that lead to the gas temperature increase and O_2 dissociation. Nevertheless, we see that, at the end of τ_{pulse}

= 50 ns, the gas temperature and O atom concentration predicted by the model agree well with experimental data after the discharge.

When η is set to 0, meaning that all the 55% of the discharge energy is transferred directly into $\dot{E}^p_{heat}$ (and $\dot{E}^p_{chem} = 0$), the gas pressure rises up to 2.8 atm and the temperature increases by about 1900 K, overestimating the experimental results of Rusterholtz et al. (2013). In addition, no O radicals are formed during the pulse because $\eta = 0$. Therefore these simulation results show that the model reproduces the impact of plasma discharges on the early dissociation of O_2 molecules as well as on the gas temperature increase.

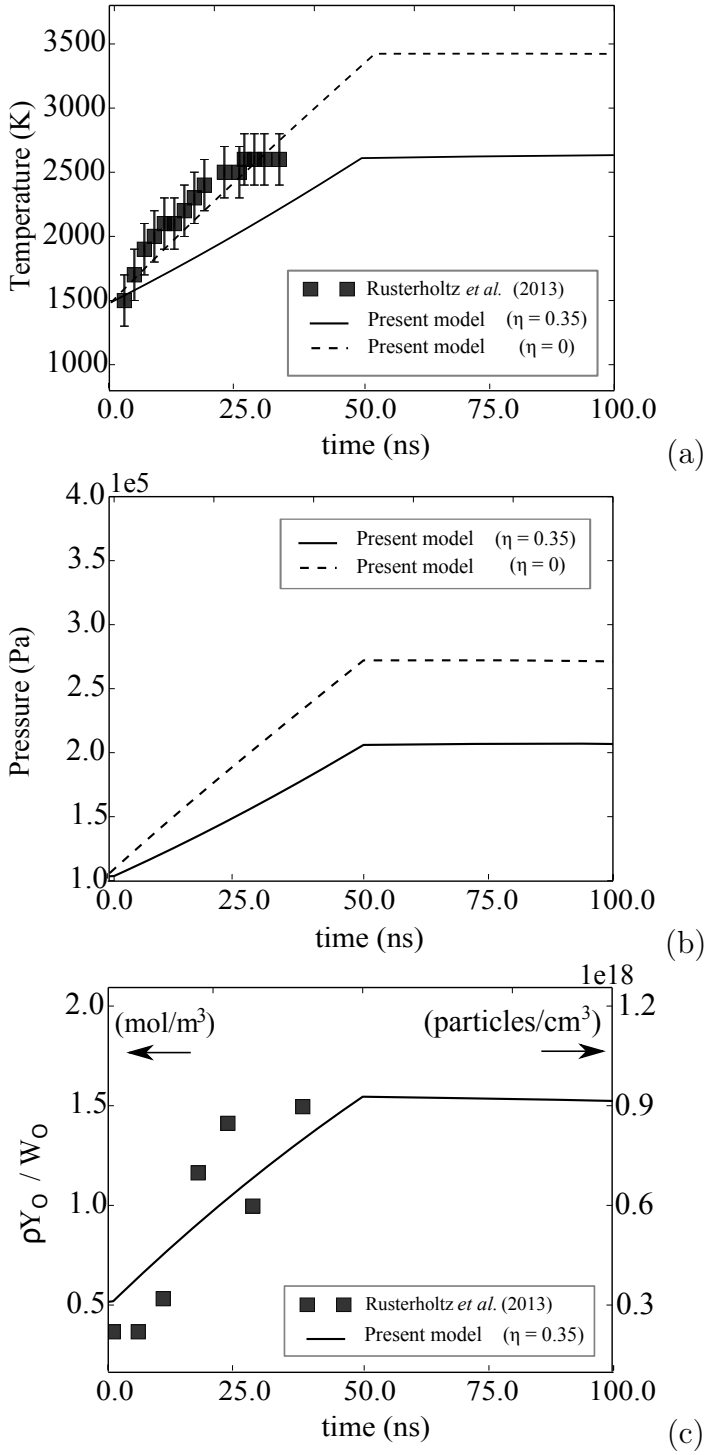

Figure 2.12: *Temporal evolution of the maximum value of (a) gas temperature, (b) pressure and (c) O radical concentration during the pulse. Model results are compared with the experimental results obtained in Rusterholtz et al. (2013).*

Chapter 3

DNS solver and 2-D DNS of NRP discharges in air

This chapter presents the DNS solver used for the multidimensional DNS of NRP discharges in reactive mixtures in quiescent and turbulent flow conditions. 2-D DNS of NRP discharges in air are analyzed, where a train of nanosecond pulses is applied at ambient temperature and pressure. These simulations highlight the gas expansion phenomenon after each pulse and the diffusion effects within the pulse interval. Good agreement between the model results and available experimental data is obtained for the values of the gas temperature and oxygen concentration in the steady-state regime. The impact of vibrational energy relaxation on the increase of the gas thermal and chemical energies is also analyzed.

Contents

3.1 Introduction

Simulations of nanosecond repetitively pulsed (NRP) discharges, in reactive flows representative of practical combustion systems, require detailed research in multi-scale modelling and model validation.

The ignition phenomena by NRP discharges is often associated with plasma channel diameters of the order of few tens of micrometers and characteristic time scales of energy deposition of the order of 10 nanoseconds. The length scales associated with the combustion processes are those of the combustion chambers that can vary from tens of meters down to centimetres. Furthermore, in some cases the geometric details of the combustion chamber and burners additionally increases the length scales associated to the combustion processes. At the Reynolds numbers of practical combustion systems, fluid dynamics length scales can then range from 0.1 to 10 meters down to smallest scales at a factor of 10^{-2}. In terms of time scales, flow residence times are of order of 10^{-3} to 1 s down to a factor of 10^{-2}. In addition, combustion processes are intrinsically linked to hydrocarbons chemistry time scales which range from 10^{-10} s for radicals-related reactions up to tens of milliseconds associated with pollutants formation processes. The ignition phenomena by NRP discharges in practical combustion systems is, therefore, an extremely complex process in terms of both length and time scales.

The first natural step to obtain the multi-scale models for ignition by NRP discharges is to build relatively simple numerical experiments that capture the most important physics observed in laboratory-scale experiments. Direct numerical simulation (DNS) is a powerful tool to design these numerical experiments in order to understand plasma-chemistry-turbulence interaction, especially when these interactions are difficult to investigate in laboratory experiments. However, DNS is still CPU-limited and the computational domain size of state-of-the-art numerical experiments remains one order of magnitude smaller than laboratory experi-

ments or practical combustion devices.

As already been stated in chapter 2, full DNS of plasma assisted-ignition, with detailed plasma and combustion chemistry at Reynolds numbers representative of practical systems, remains out of reach. DNS resolves the governing equations by means of spatial discretisation and temporal integration methods without filtering or averaging the solution vector. It therefore requires full spatial and temporal scales resolution of the phenomena in order to accurately unveil the physics underlying the ignition by plasma discharges. In turbulent combustion / ignition, the computations become particularly challenging since the full range of turbulent length and time scales must also be resolved. Furthermore, the most CPU demanding processes in DNS are still the ones related to the chemistry. The phenomenological plasma model developed in the previous chapter already represents an effort for chemistry reduction and, therefore, a step forward for multi-dimensional DNS studies of plasma-assisted ignition.

The DNS solver will be briefly presented in section 3.2 of this chapter. The phenomena governing the evolution of scalars in a sequence of nanosecond plasma discharges in air are then analyzed by means of 2-D numerical experiments in section 3.3. The numerical results are compared with the experimental data obtained in the laboratory-scale experiments of Rusterholtz et al. (2013).

3.2 DNS solver

The DNS numerical solver used in the present thesis to perform multi-dimensional simulations of NRP discharges in reactive systems is the YWC code. The code has been previously developed by Axel Coussement (Coussement (2012)) and Jean Caudal (Caudal (2013)), during their PhD thesis at the EM2C Laboratory.

During the present thesis, the YWC code was upgraded in order to inte-

grate the phenomenological plasma model presented in chapter 2. Along with the traditional mass, momentum, species and energy balance equations, and the plasma model source terms in the energy and species balance equations, the vibrational energy equation is also solved.

The code is dedicated to compressible reactive flow simulations and is based on detailed chemistry and multicomponent mixture-averaged transport properties. These properties are obtained through the Fortran 90 REGATH library (Candel et al. (2011)), where routines are comparable to those of the CHEMKIN library.

As previously discussed in the *Introduction*, experimental (Xu et al. 2011) and simulation results (Tholin 2012; Xu et al. 2014) showed that following the discharge, a shock wave propagates outwards from the centre of the discharge channel. Therefore, in order to capture these stiff pressure waves induced by each plasma discharge, the hyper-viscosity technique developed by Cook and Cabot (2004); Cook and Cabot (2005) and Fiorina and Lele (2007) was applied.

The numerical methods, boundary conditions and other characteristics of the YWC code are described in detail in Caudal (2013). A brief overview is given below.

3.2.1 Spatial derivatives discretization and temporal integration

A structured mesh is used in the computational domain in order to facilitate the implementation of high-order numerical methods. These high-order numerical methods reduce the numerical errors associated with the spatial derivatives discretization and temporal integration. The spatial derivatives are computed with a 4th-order centered finite-difference scheme. An 8th order explicit filtering scheme is used for stability pur-

poses. The code is explicit in time using a 4th-order Runge-Kutta method.

3.2.2 Integration time-step

The integration time-step is determined so as to ensure the numerical stability of the convective and diffusive terms of the equations. The CFL condition for the diffusive, conductive, convective and viscous terms is therefore evaluated. For the present study of repetitively pulsed discharges in reactive mixtures, we also impose a constant time-step of 10^{-10}s during the energy deposition time τ_{pulse}. The integration time-step is finally given by the most restrictive of these time-steps from the CFL and plasma conditions.

3.2.3 Boundary conditions

DNS simulations of NRP discharges pose additional challenges in setting the boundary conditions of the computational domain. In fact, the ultrafast energy deposition induces a shock wave propagating outwards from the centre of the computational domain. As the computational domain size is limited by the CPU costs, the attenuation of the pressure wave over a small domain length may not be sufficient to avoid its reflection at the boundaries back into the interior of the domain. In compressible DNS, non-reflecting outflow boundary conditions are therefore needed to suppress these nonphysical reflections of the pressure waves generated by each pulse. The adopted strategy in the YWC solver is to employ the 3-D Navier-Stokes Characteristic Boundary Conditions (3-D-NSCBC) treatment for non-reflecting outflow boundary conditions. The detailed formulation of the 3-D-NSCBC implemented in the YWC code is given in Coussement et al. (2012).

3.2.4 Code parallelisation

The code is parallelized through the MPI method, where the computational domain is divided into multiple parts and each of these parts is solved by a dedicated processor. In parallel computing, the real simulation time corresponds therefore to the time taken by a single processor to perform its computational charge τ_p and the time consumed during the processor's communications with the other processors τ_{com}, where ideally $\tau_{com} << \tau_p$. As shown in Caudal (2013), the YWC code has a perfect scalability and is therefore suitable for massively parallel computing, as performed in the present work.

The simulations performed in this work were only possible with the IDRIS (CNRS) cluster allocated hours. An estimation of the CPU hours required for the simulations can be consulted in Table A.1 presented in the Appendix A.

3.3 2-D DNS of NRP discharges in air

3.3.1 Test-case conditions and numerical set-up

In this section, the repetitively pulsed regime of plasma discharges in air is analysed. For this, the same discharge characteristics as those used in the experimental work of Rusterholtz et al. (2013) are retained. A sequence of discharge pulses is applied at pulse frequency $f = 10$ kHz in air in quiescent conditions. The initial conditions are $p = 1$ atm and $T = 300$ K, respectively, and each pulse has an energy of 670 μJ. It is assumed that the plasma channel formed by each pulse has a cylindrical shape with radius $r_d = 225$ μm and length $L_d = 4$ mm, corresponding to the experimental conditions described in Section 2.5.2.

Since $r_d \,/\, L_d << 1$, the axial gradients of gas temperature and species density are negligible compared to the radial gradients and, therefore, a 2-D computational domain perpendicular to the inter-electrode axis

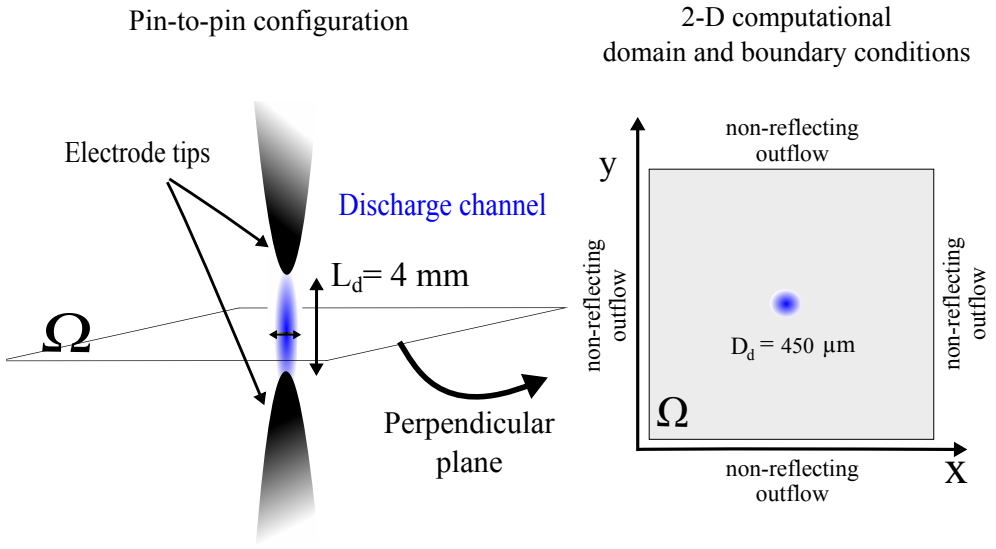

Figure 3.1: *Schematic of a pin-to-pin configuration of NRP discharges device. The 2-D computational domain is a plane perpendicular to the inter-electrode axis.*

is considered, as shown in Fig. 3.1. This 2-D computational domain thus represents the cross-section of an infinitely long cylindrical-shape discharge channel.

The computational zone where the energy of the discharge is deposited is defined by the spatial function $\mathcal{F}$ given by:

$$\mathcal{F}(r) = \text{erfc}\left(\frac{r}{a}\right)^b \tag{3.1}$$

where r refers to the radial distance from the discharge axis and a and b are geometric parameters. These geometric parameters are computed so that the area defined by this function is equal to πr_d^2, with r_d the discharge radius. The volume of the discharge is thus given by the equivalent volume $V = \pi r_d^2 L_d$, with L_d the discharge length.

As already mentioned, each pulse generates a pressure wave that prop-

agates outwards from the centre of the discharge channel. Due to the restrictions on computational domain size for feasible 2-D DNS studies, and in order to simulate the experimental conditions of repetitively pulsed discharges in open flow conditions, the outflow NSCBC are chosen to avoid the reflection of these pressure wave back into the centre of the domain.

The size of the computational domain ensures that the boundary conditions do not impact the solution. This has shown to be particularly critical in the repetitively pulsed regime, since the discharge radius is small and even the smallest perturbation of the solution can result in the displacement of the plasma channel axis away from its original axis at the centre of the computational domain.

A domain size of 5.12 $\times$ 5.12 mm ensured that the cross-section of the plasma channel remained centred in the domain for the number of pulses applied during the simulations. A uniform grid with a mesh size $\Delta x = 10$ μm is considered, in order to capture the steep spatial gradients inside the discharge channel.

Table 3.1 summarizes the NRP discharge characteristics and the model parameters studied in the present configuration.

Table 3.1: *NRP discharge characteristics and model parameters used in the 2-D DNS of NRP discharges in air.*

Mixture	η	α	f	$\sigma_{pulse}(\mathrm{J/m^3})$	Nb pulses	flow
Air	0.35	0.55	10	1.1×10^6	10	quiesc.
Air	0.00	0.55	10	1.1×10^6	10	quiesc.

3.3.2 Results

3.3.2.1 Temporal evolution of the gas temperature and O atom concentration in a sequence of 10 discharge pulses

Figure 3.2 shows the temporal evolution of the gas temperature and oxygen concentration at the centre of the discharge zone for a sequence of 10 discharge pulses. The results show an ultrafast increase of the gas temperature by about 1000 to 2000 K during each pulse. The temperature progressively decreases between pulses due to the gas expansion and diffusion effects. At the end of each pulse period, the value of the gas temperature is higher than that of the previous period. Nevertheless, this minimum temperature reaches a quasi-stationary value of about 1600 K after eight pulses when diffusive fluxes are balanced with the heat released by the discharge. This value of the gas temperature is in good agreement with the experimental one, $T_{exp} = 1500$ K, measured in Rusterholtz et al. (2013) (discussed in Section 2.5.2).

The evolution of the O radical concentration shows that, during each pulse, its concentration rapidly increases and then decreases due to gas expansion, diffusion and to the recombination of O radicals into O_2 molecules. The minimum and the maximum values of the O radical concentration in the stationary regime are also in good agreement with the ones observed in the experimental work of Rusterholtz et al. (2013).

When the model parameter η is set to 0, the simulation results show that, in the steady-state regime $t>$ 700 μs, the variation of the gas temperature during the pulse is about 3000 K, for example at $t = 800$ μs the gas temperature increases from 2000 to 5000 K. Therefore, these simulation results obtained with $\eta = 0$ strongly overestimate the 1000 K temperature variation observed in the experimental results.

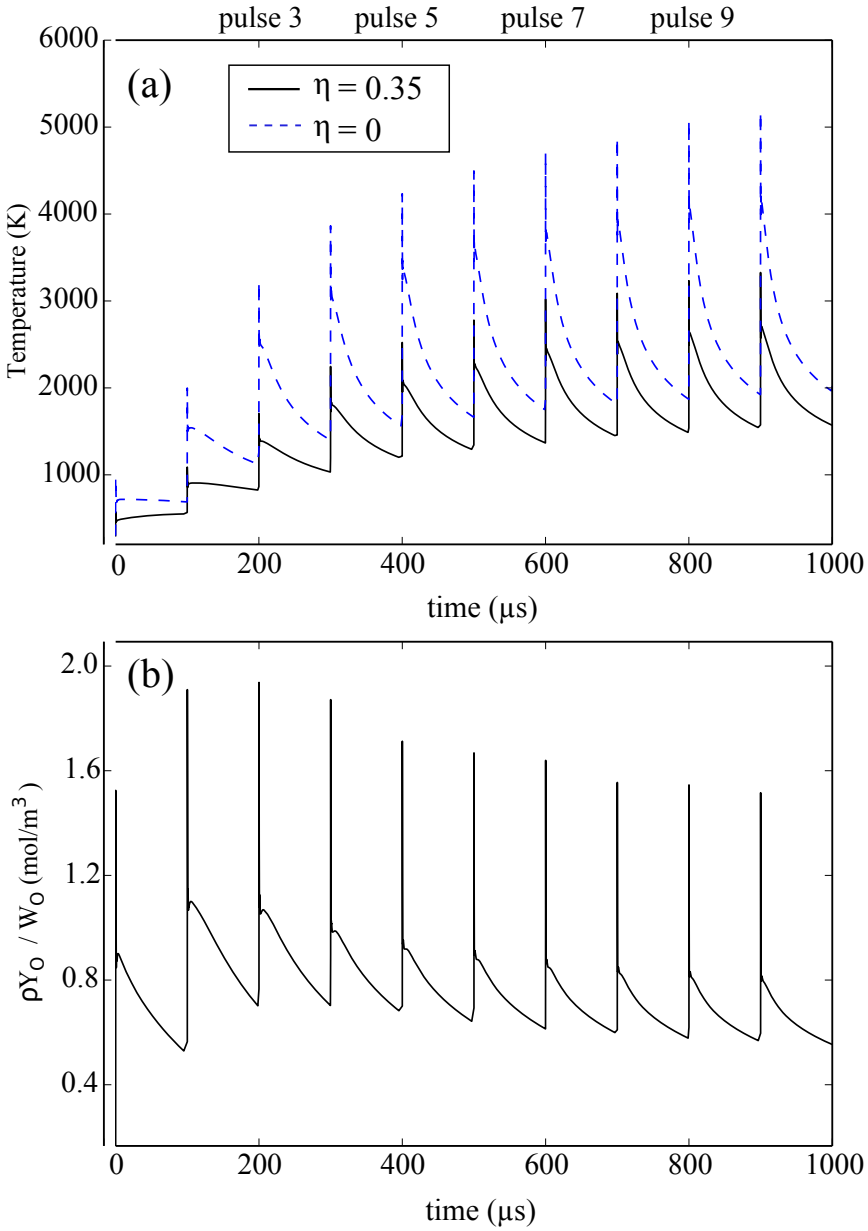

Figure 3.2: *Temporal evolution of (a) the gas temperature and (b) the oxygen concentration at the centre of the discharge channel in a sequence of 10 pulses in air. The following parameter values were used: pulse repetition frequency f = 10 kHz, energy density per pulse $\sigma_{pulse} = 1.1{\times}10^6$ J/m^3 and model parameters: $\alpha = 0.55$ and two values of η: 0.35 and 0.*

3.3.2.2 Vibrational energy relaxation

The early dissociation of O_2 also impacts the relaxation rate of gas vibrational energy. Indeed, as expected from the experimental results of Millikan and White (1963), through the empirical correlation of the vibrational energy relaxation time τ_{VT} given in Eq. (2.56), the rate of V-T transfer is highly increased in the presence of O atoms.

To quantify this impact, Fig. 3.3a shows the temporal evolution of the gas energy (thermal plus chemical energies), normalised by the energy density deposited during each pulse, σ_{pulse}. The results show that within the first pulse period (first 100 μs), for both values of η, the discharge energy deposited into vibrational modes (e_{vib}) does not contribute to the increase of the gas thermal and chemical energies up to the end of the pulse period. Which means that 45% of the pulse energy remains stored as vibrational energy during this first pulse period. However, after the second discharge, the increase of both the gas temperature and O atoms concentration observed for $\eta = 0.35$ in Fig. 3.2, leads to a faster relaxation of this vibrational energy into gas thermal and chemical energies. As shown in Fig. 3.3b for $\eta = 0.35$, after the 3rd pulse, most of the vibrational energy deposited during each pulse is relaxed before the next one. Although higher gas temperatures are reached in the case $\eta = 0$, the absence of O atoms produced during the discharge leads to an underestimation of the vibrational energy relaxation rate. For $\eta = 0$, the relaxation of vibrational energy is much slower than the pulse period.

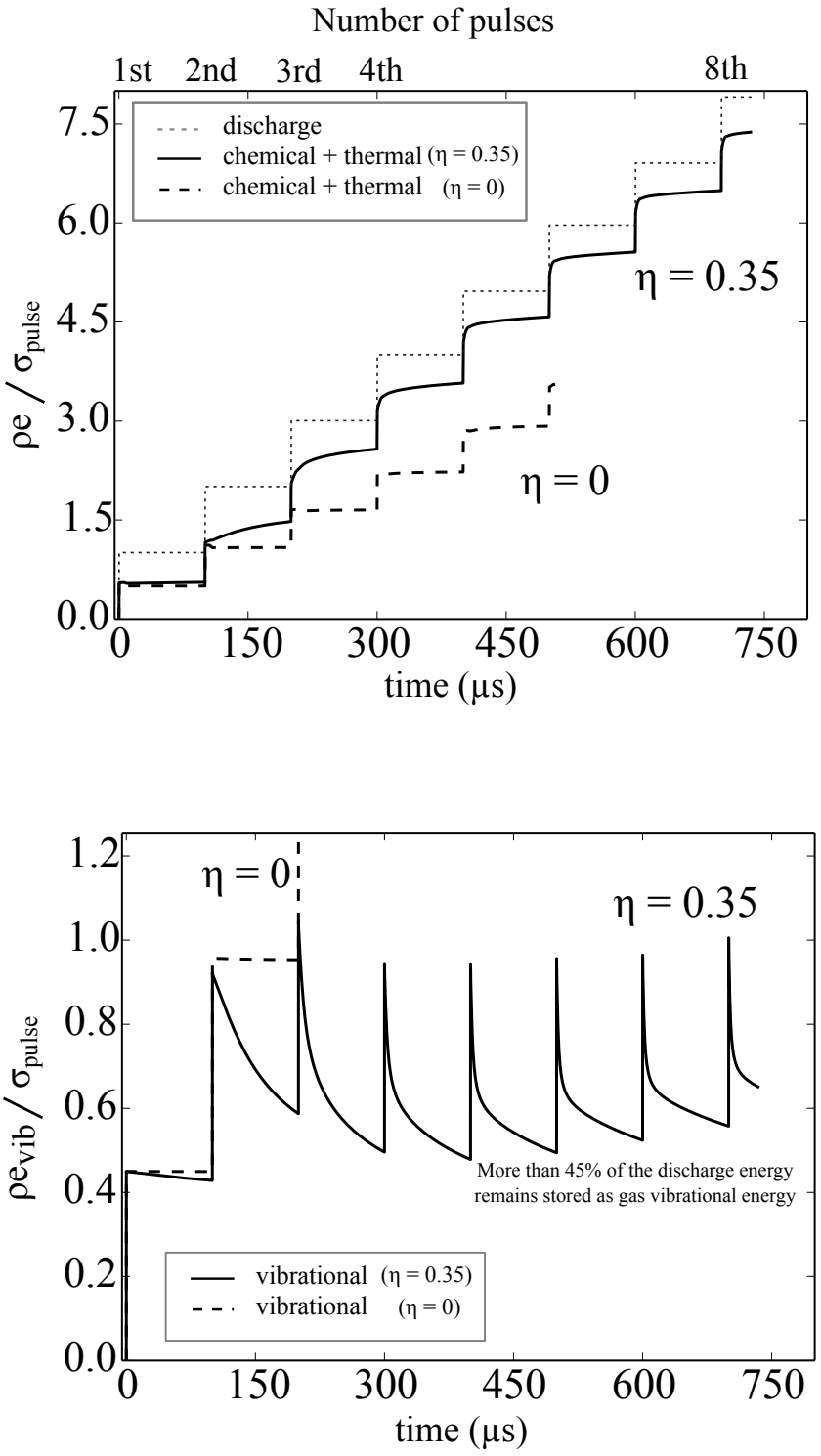

Figure 3.3: *Temporal evolution of (a) gas thermal plus chemical energy normalised by the energy of a single discharge; and (b) gas vibrational energy; in a sequence of NRP discharges in air for two values of the model parameter η.*

Nevertheless, it should be noted that the V-T rate defined by Popov (2011a):

$$\tau_{VT} = \frac{1}{p_O} k_B T / k_{VT} \tag{3.2}$$

where k_B is the Boltzmann constant and:

$$k_{VT} = 4.5 \times 10^{-15} \left(\frac{T}{300} \right)^{2.1} \tag{3.3}$$

is faster than the one used here; about 220 times faster at 300 K and 10-20 faster between 1000 and 2000 K. Therefore, the vibrational energy may relax even faster than predicted here.

3.3.2.3 Single pulse analysis: induced shock-wave

Due to the ultrafast energy deposition (within $\tau_{pulse} = 50$ ns), compressible effects occur at each discharge pulse, as shown experimentally by Xu et al. (2011). For a better understanding of the gas dynamic effects occurring at each single pulse, Fig. 3.4 shows the temporal evolution of the gas pressure and density radial profiles following the 5^{th} discharge of this sequence of pulses. Two values of the model parameter η (0 and 0.35) are analyzed.

Figure 3.4a shows that, after the fast increase of the pressure, the gas expands and an initial shock wave separates at approximately $t = 0.25$ μs and propagates outwards through the surrounding air. Because the external source of energy ceases after the pulse and because the energy must be spread over an ever-increasing radius (2-D computations), the shock strength diminishes due to both the expansion and the viscous dissipation.

As can be inferred from the slope of the temporal evolution of the pressure wave radius shown in Fig. 3.5, when the shock wave leaves the discharge zone, its Mach number is slightly larger than 1 and then decreases to-

wards unity. Therefore, the initially weak shock wave quickly decays into a pressure wave. When $\eta = 0$, the pressure wave separates faster because of its higher initial velocity. Figure 3.4a also shows that the pressure waves are rapidly attenuated right after leaving the discharge zone: at r = 2.4 mm, their amplitude is of the order of 1.2 atm for both values of η.

Figure 3.4b shows that the separation time of the density wave is about $t = 1$ μs. This characteristic time depends on the size of the heated channel and, therefore, on the number of pulses previously applied. It also depends on the amount of the discharge energy going into the ultrafast increase of gas temperature during the discharge, as discussed in Xu et al. (2014). Due to these pressure waves created by the plasma discharge, part of the deposited energy leaves the discharge zone as acoustic energy. For $\eta = 0.35$ about 10% of the pulse energy is converted into acoustic energy, whereas for $\eta = 0$ this value increases to about 20%. These values are obtained by integrating the value of the gas energy over the computational area πR^2, with $R = 2r_d$, centred at the discharge axis, immediately before and after the gas expansion. It is, therefore, interesting to emphasise that by transferring part of the pulse energy into chemical energy, the losses by acoustic energy runaway from the discharge zone are reduced.

3.4 Conclusions

In this chapter, we have performed 2-D DNS of NRP discharges in air, and the simulation results were compared with available experimental data from Rusterholtz et al. (2013). The simulations were performed for two values of the model parameter η: $\eta = 0$, meaning that O_2 dissociation does not occurs during the pulse, and $\eta = 0.35$ meaning that 35% of the energy of each pulse is spent on ultrafast O_2 dissociation.

The simulation results were in good agreement with the experimental data for the set of model parameters $\alpha = 0.55$ and $\eta = 0.35$. The gas temperature obtained in the steady state at the end of each pulse period

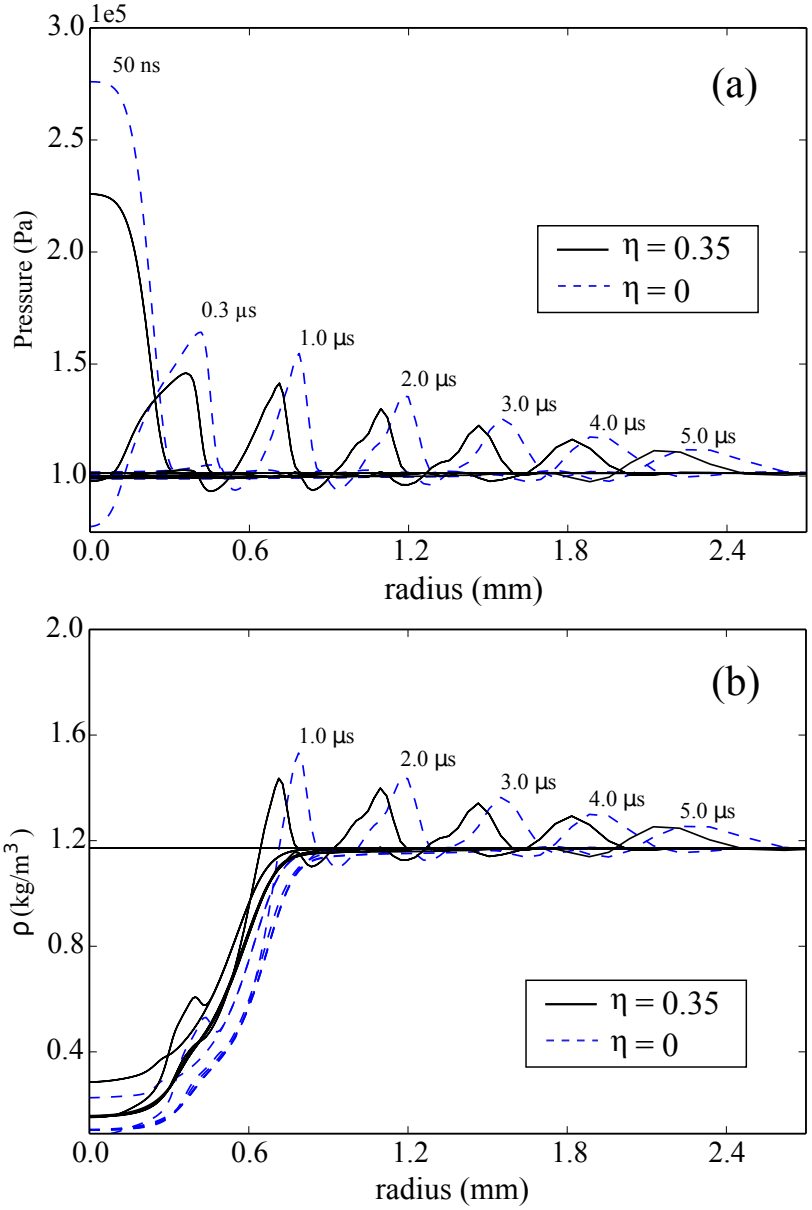

Figure 3.4: *Time series of the (a) pressure wave and (b) the gas density radial profiles after the* 5^{th} *pulse. Two values of the model parameter* η *are considered:* $\eta = 0$ *and* $\eta = 0.35$.

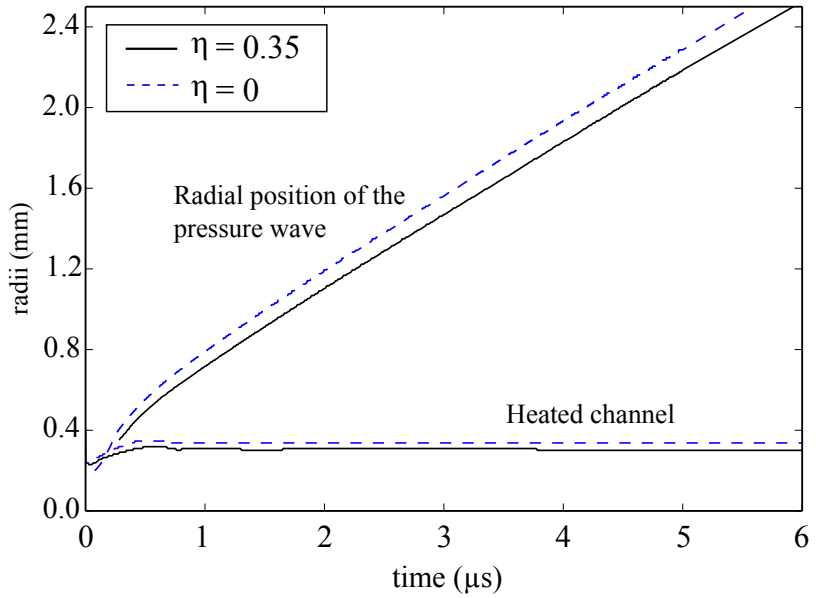

Figure 3.5: *Temporal evolution of the radial position of the pressure wave and the heated channel after the* 5^{th} *pulse. Two values of the model parameter* η *are considered:* $\eta = 0.35$ *and 0.*

was about $T = 1600$ K, which compares very well with the experimental value $T_{exp} = 1500$ K. The percentage of the O_2 dissociation right before a pulse of about 15% also agrees well with the experimental value of 10 to 15%. The evolution of the gas temperature and O atom concentration is governed by the ultrafast phenomena within the pulse characteristic time, and by gas expansion and diffusion effects between two consecutive pulses. Therefore, 0-D computations are not able to capture these phenomena without a diffusion and gas expansion model. It was also shown that, part of the discharge energy is lost as acoustic energy due to the formation of a pressure wave and that this acoustic energy is rapidly dissipated around the discharge zone. Finally, the results showed that after 3 discharge pulses, the gas temperature at the centre of the discharge channel is above 1000 K which, combined with a high concentration of O atoms, will certainly have an impact on the ignition of reactive mixtures, as will be studied in the following Chapters.

Chapter 4

2-D DNS of NRP discharge-assisted ignition in quiescent and turbulent flow conditions

In the present chapter, the ignition of a methane-air mixture under nanosecond repetitively pulsed discharges is analyzed. Plasma-combustion-turbulence interactions are studied by means of 2-D DNS of NRP discharges in a lean methane-air mixture in both quiescent and turbulent flow conditions. For the latter one, the impact of the turbulence on mixture ignition is analyzed under two Reynolds numbers conditions. The influence of the initial distribution of the turbulent eddies relative to the centre of the discharge channel is also analyzed. To capture the transient ignition phenomena, multicomponent mixture-averaged transport properties and detailed combustion chemistry were considered. The ultrafast increase of the gas temperature and the dissociation of O_2 molecules increase the mixture reactivity during the discharge pulse, whereas gas expansion, diffusion and the convection of the hot kernel within the pulse interval act on the opposite way.

Contents

4.1 Introduction

A sequence of NRP discharges are applied at a pulse frequency of $f = 10$ kHz in methane-air mixture. It is assumed that the energy of each pulse is 670 μJ and that the radius of the discharge channel $r_d = 225$ μm is constant for all the applied discharges.

These pulse characteristics are the same as those studied in chapter 3 for NRP discharges in air. A 2-D computational domain perpendicular to the electrode tips is also considered, as shown in Fig. 3.1. The spatial function $\mathcal{F}$, which defines the shape and the location of the discharge energy deposition in the computational domain, is also given by Eq. (3.1). Nonreflecting outflow NSCBC boundary conditions are applied in all directions, in order to avoid the reflection of the pressure waves at the boundaries back into the computational domain.

4.2 Test-cases description and numerical set-up

A methane-air mixture with an equivalence ratio $\phi = 0.8$ is uniformly distributed over the 2-D computational domain at the beginning of the computations. The initial conditions of mixture pressure and temperature are $p = 1$ atm and $T = 300$ K, respectively. The detailed combustion mechanism (Lindstedt (1998)) which comprises 29 species and 141 elementary reactions is used to capture the transient ignition phenomena.

The above described pulse characteristics and mixture initial conditions are applied to all the test-cases performed in this chapter. Table 4.1 summarizes the flow characteristics and model parameters used in each test-case described in detail below.

Table 4.1: *Flow characteristics and model parameters used in the 2-D DNS of NRP discharges in methane-air mixture.*

flow	$\mathbf{Re}_{lt}$	**u' (m/s)**	α	η	**nb of pulses**
quiescent	-	-	0.55	0.35	2
quiescent	-	-	0.55	0.0	4
turbulent	44	2	0.55	0.35	2
turbulent*	395	6	0.55	0.35	3 to 4

Pulse frequency, $f = 10$ kHz;
Deposited energy density per pulse $\sigma_{pulse} = 1.1 \times 10^6$ J/m^3
* four different homogenous isotropic turbulence are analyzed

- **2-D DNS of NRP discharges in methane-air mixture in quiescent conditions:**

  The aim of the test-cases performed in quiescent conditions is to evaluate the impact of the ultrafast O_2 dissociation and ultrafast gas heating after each plasma discharge on the ignition phenomena. The evolution of the gas temperature and species concentrations, close to the discharge zone, are analyzed and compared for two values of the model parameter: $\eta = 0$ and $\eta = 0.35$. The impact of the ultrafast O_2 dissociation on the flame kernel formation is, therefore, isolated by changing this value of η.

- **2-D DNS of NRP discharges in methane-air mixture in turbulent flow conditions:**

  The second set of test-cases is designed to study the plasma/ combustion/ turbulence interactions during the ignition process. The formation and development of the ignition kernel is analyzed when a train of nanosecond repetitively pulsed discharges is applied under turbulent flow conditions. Homogeneous isotropic turbulence characterized by turbulent Reynolds numbers of $\mathrm{Re}_{lt} = 44$ and $\mathrm{Re}_{lt} = 395$ is applied at the beginning of the computations. The turbulence then decays over time. To mimic the chaotic nature of turbulent ignition, we also analyze the impact of different distributions of the

turbulent eddies relative to the discharge channel. For this, four different velocity fields are imposed at the beginning of the computations for the same flow Reynolds number. The details of the homogeneous isotropic turbulence will be further described in section 4.4.

4.3 2-D DNS of NRP discharges in methane-air mixture in quiescent conditions

4.3.1 Impact of the ultrafast O_2 dissociation and gas temperature increase on the ignition phenomena

Figure 4.1 shows the temporal evolution of the maximum value of the gas temperature in the computational domain for $\eta = 0$ and $\eta = 0.35$ simulations. This maximum value of the gas temperature coincides with the value of the gas temperature at the centre of the discharge zone, since the discharge energy is always deposited at the centre of the computational domain.

The simulation results for $\eta = 0.35$, where 35% of the pulse energy is spent on the ultrafast O_2 dissociation, show an ultrafast increase of the gas temperature after the first discharge. After this first pulse, the gas temperature increases from $T = 550$ K up to $T = 750$ K and remains approximately constant until $t = 100$ μs. When the second discharge is applied at $t = 100$ μs, the temperature further increases and then follows an asymptotic decrease towards the adiabatic flame temperature. Therefore, mixture ignites after a sequence of two discharge pulses.

When the ultrafast O_2 dissociation is not considered in the simulations $\eta = 0$, the results show that the evolution of the gas temperature after the

first pulse is similar to that observed for $\eta = 0.35$. However, the mixture ignites only after four discharge pulses. In this case of $\eta = 0$, the gas temperature significantly decreases after the second and the third pulses. It is also interesting to note that the gas temperature decreases much significantly right after each pulse, compared to the decrease observed for $\eta = 0.35$. This is explained by the gas expansion and the acoustic energy runaway from the discharge zone, as previously discussed in chapter 3 for 2-D DNS of NRP discharges in air.

The results also show that, preceding the pulses leading to mixture ignition, the gas temperature of T= 1200 K in the case $\eta = 0$ is comparatively higher than that of T = 750 K needed to ignite the mixture in the case of $\eta = 0.35$.

Nevertheless, at the beginning of the second discharge at $t = 100$ μs, the value of the gas temperature is similar in both cases. The difference of the gas temperatures: T = 700 K for $\eta = 0$ and T= 760 K for case $\eta = 0.35$, does not explain why in $\eta = 0.35$ the mixture ignites following two discharges whereas in $\eta = 0$ the mixture does not ignite.

4.3.2 Mixture reactivity on pulse-to-pulse coupling

To further understand the phenomena, Figs. 4.2 and 4.3 show the species mass concentrations at the centre of the discharge channel for $\eta = 0.35$ and $\eta = 0$, respectively. In these figures, only the 1-D half-domain radial profiles are plotted since the solution is axisymmetric around the centre of the discharge channel at $r = 0$ mm. These radial profiles are captured at four different time instants.

The results plotted in Figure 4.2 are captured at (a) the end of the first pulse $t = 50$ ns, (b) at the beginning of the second pulse $t = 100$ μs, (c) at the end of the second pulse $t = 100$ μs + 50 ns and (d) when the mixture is already ignited.

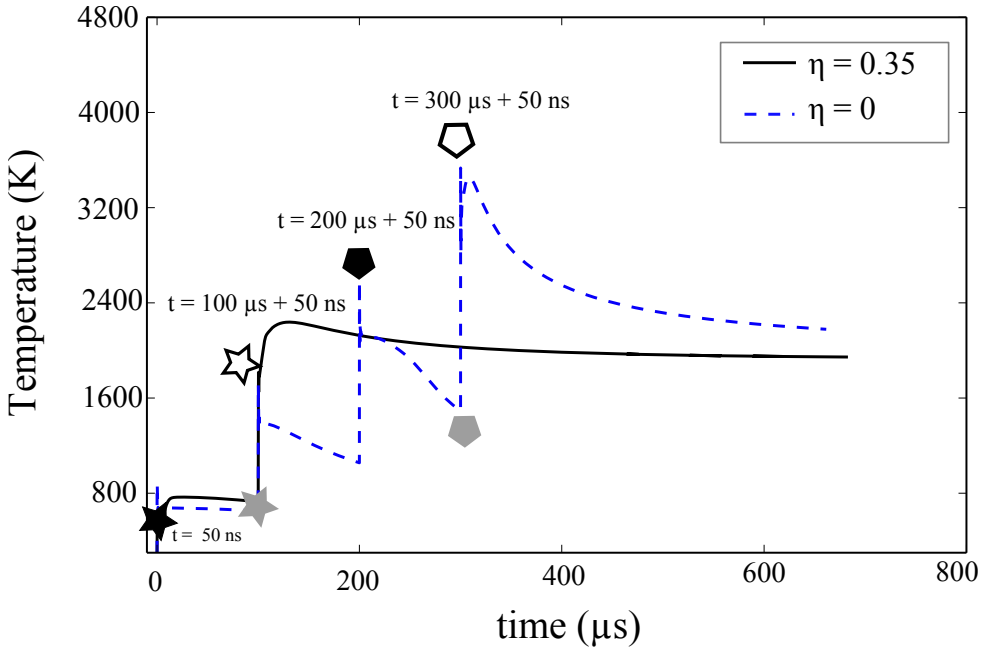

Figure 4.1: *Temporal evolution of the maximum value of gas temperature. Mixture ignites after two discharges if* $\eta = 0.35$ *(solid line) whereas four discharges are needed if* $\eta = 0$ *(dashed line).*

Figure 4.2a shows that, when the ultrafast O_2 dissociation is considered, at the end of the first pulse, along with the ultrafast increase of O radical produced by the plasma, small quantities of OH, CH_2O, HCO, H_2O and other intermediate combustion species are also formed inside the discharge zone. This means that within τ_{pulse}, a small quantity of O radical is rapidly recombined with CH_4 initiating chain-branching reactions and giving rise to radicals such as CH_2O and OH. Even though in small quantities, these radicals will recombine with O atoms to form CO_2 and H_2O, and other intermediate combustion species like CH_2O and CH_3O, increasing the chemical reactivity of the mixture, during the pulse interval. By the time of the second discharge at $t = 100$ μs, Fig. 4.2b shows that the gas composition at the centre of the discharge channel is no longer a pure methane-air mixture but rather a pool of radicals that have been enhanced by the former discharge pulse. Indeed, the concentrations of CH_2O and CH_3O shown in Fig. 4.2b are higher than those shown in Fig. 4.2a at the

end of the first pulse, whereas the concentrations of O and OH radicals are lower due to their recombination with intermediate species.

Nevertheless, regarding CH_4, combustion has barely started up to the second discharge and only after the second pulse, as shown in Figs. 4.2c and d, the concentration of CH_4 decreases consistently, leading to an effective ignition event. Figure 4.2d shows the well defined reaction zone formed after the ignition event, which propagates outwards from the centre of the discharge channel.

Figure 4.3 shows the simulation results in the case where the ultrafast O_2 dissociation during the pulse is not considered. The time instants captured in Fig. 4.3 show the species radial profiles only after the third discharge: (a) at the end of the third pulse t= 200 + 50 ns, (b) at the beginning of the fourth pulse t= 300 μs, (c) at the end of the fourth pulse t= 300 μs + 50 ns, and (d) when the mixture is already ignited.

Figure 4.3a shows that intermediate combustion species only become significant after the 3^{rd} pulse. When O atoms are not formed by the plasma discharge the chemical reactivity of the mixture is considerable lower than that observed after the first discharge in the case of $\eta = 0.35$ even at a lower gas temperatures (see Fig. 4.2a). Chain-branching reactions will be triggered only when the gas temperature rises up to $T \approx 2800$ K after the third pulse $t = 200\ \mu s + \tau_{pulse}$. Between the third and the fourth pulses the chemical reactivity of the mixture increases, and the radicals formed during the third pulse recombine with intermediate combustion species even if the gas temperature decreases during this period. As shown in Figs.4.3b and c a significant amount of radicals are produced by the former pulse and mixture ignites after the fourth pulse when the gas temperature further increases up to $T = 3500$ K as previously shown in Fig. 4.1 for $\eta = 0$. Therefore, the difference of the chemical composition of the mixture in the case $\eta = 0$ and $\eta = 0.35$ at the beginning of the second discharge explains the ignition failure and the ignition success of simulations.

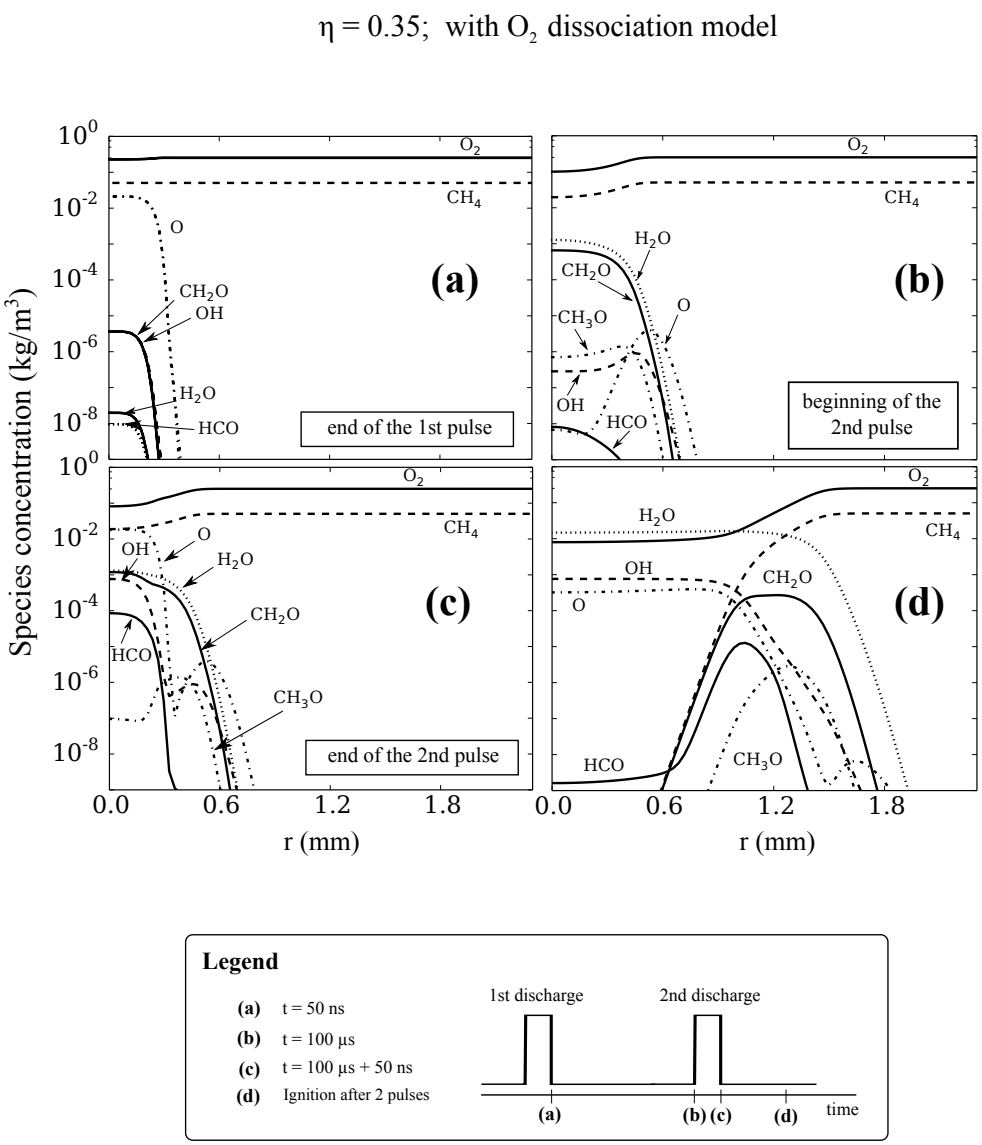

Figure 4.2: *Radial profiles of species concentrations considering the ultrafast O_2 dissociation during the discharge pulses, $\eta = 0.35$. Results are presented at 4 different instants (a) at the end of the first pulse - $t = 50$ ns, (b) immediately before the second pulse at $t = 100$ µs, (c) at the end of the second pulse - $t = 100$ µs + 50 ns and (d) after the mixture ignition when the flame kernel propagates outwards from the centre of the discharge channel.*

4.3.3 Delay and energy of ignition

These simulation results show that O radical plays a major contribution on the ignition enhancement at low gas temperature, leading to a decrease of the ignition delay and the external source of energy needed to ignite. Different ignition delays and ignition energies (number of discharge pulses) are obtained whether the O_2 dissociation model is considered or not. For the present conditions, if only the ultrafast increase of the gas temperature is considered as a result of the plasma discharge, ignition will occur only after 4 discharge pulses. In this case, the temperature threshold to trigger combustion chain-branching reactions is much higher ($T = 3000$ K) than that observed when O atoms are also produced by the discharge. Therefore, the dissociative quenching reactions of electronic states of N_2 molecules by O_2 molecules increase the chemical reactivity of the mixture. It induces an ultrafast recombination of O atoms with CH_4 molecules and the production of H and OH radical. The increase of radicals and intermediate combustion species inside the discharge zone leads to mixture ignition after only two discharge pulses and at comparatively lower gas temperatures ($T = 750$ K).

4.4 2-D DNS of NRP discharges in methane-air in turbulent flow conditions

The same sequence of NRP discharges is now applied to the same methane-air mixture but under turbulent flow conditions. Two initial flow fields characterized by turbulent Reynolds numbers of $\mathrm{Re}_{lt} = 44$ and $\mathrm{Re}_{lt} = 395$ are imposed at the beginning of the simulations in order to study the impact of turbulence on mixture ignition. The model parameters $\alpha = 0.55$ and $\eta = 0.35$ are kept constant in all simulations.

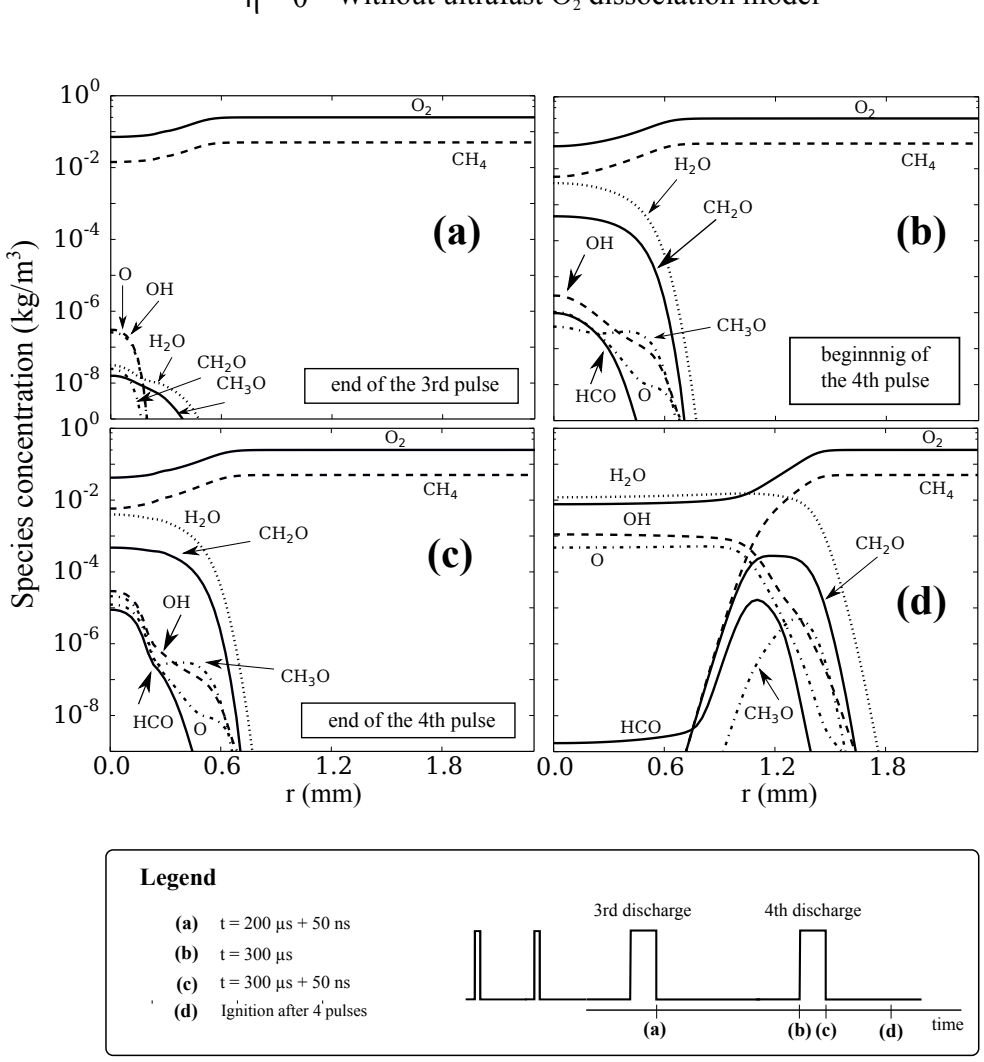

Figure 4.3: *Radial profiles of species concentrations when the ultrafast O_2 dissociation during the discharge pulses is not considered, $\eta = 0$. Results are plotted at 4 different time instants (a) at the end of the third pulse - $t = 200\ \mu s + 50$ ns, (b) immediately before the fourth pulse - $t = 300\ \mu s$, (c) at the end of the fourth pulse - $t = 300\ \mu s + 50$ ns, and (d) after mixture ignition when the flame kernel propagates outwards from the centre of the discharge channel.*

4.4.1 Homogeneous Isotropic Turbulence

4.4.1.1 Initialization

The initial homogeneous isotropic turbulence is initialized using the Passot-Pouquet spectrum with a constant value of the most energetic scale, $l_e = 6.25\times10^{-4}$ m and u' given in Table 4.1. The turbulent Reynolds number is defined as $\mathrm{Re}_{lt} = \frac{l_t \cdot u'}{\nu}$, where l_t is the integral length scale and ν is the air viscosity computed for the initial conditions of the simulations.

4.4.1.2 Mesh and boundary conditions

The computational domain is chosen so that the smallest scales of turbulence, of the order of the Kolmogorov scale, are resolved and so that the turbulent integral scales are smaller than 1/4 of the solution domain length, to avoid the influence of boundary conditions. In the test-cases of $\mathrm{Re}_{lt} = 44$ and $\mathrm{Re}_{lt} = 395$, the Kolmogorov scales are $\eta_k = 24.4$ μm and $\eta_k = 14.1$ μm, respectively. The integral length scales of $l_t = 0.416$ mm and $l_t = 1.23$ mm require that the solution domain should be at least 4×1.23 mm.

Following this foregoing analysis of the turbulent scales, the 2-D DNS of NRP discharges in turbulent reactive flow conditions are performed on a 512×512 uniform grid, with mesh size $\Delta x_i = 10$ μm. The value of Δx_i ensures that the Kolmogorov scale condition is satisfied, as Δx_i is smaller than the smallest scales of turbulence ($\Delta x = 0.7\eta_k$). The integral scale condition is also satisfied by the computational domain size $L = 5.12$ mm, as $L > 4\times1.23$ mm.

Figure 4.4a shows an example of the flow vorticity imposed at the beginning of the computations for $\mathrm{Re}_{lt} = 44$ and $\mathrm{Re}_{lt} = 395$, note that only the colour scale changes for the two Reynolds numbers. Figures 4.4b and c show the velocity magnitude referent to this vorticity field for $\mathrm{Re}_{lt} = 44$ and $\mathrm{Re}_{lt} = 395$ test-cases, respectively, the same colour scale is used in these figures.

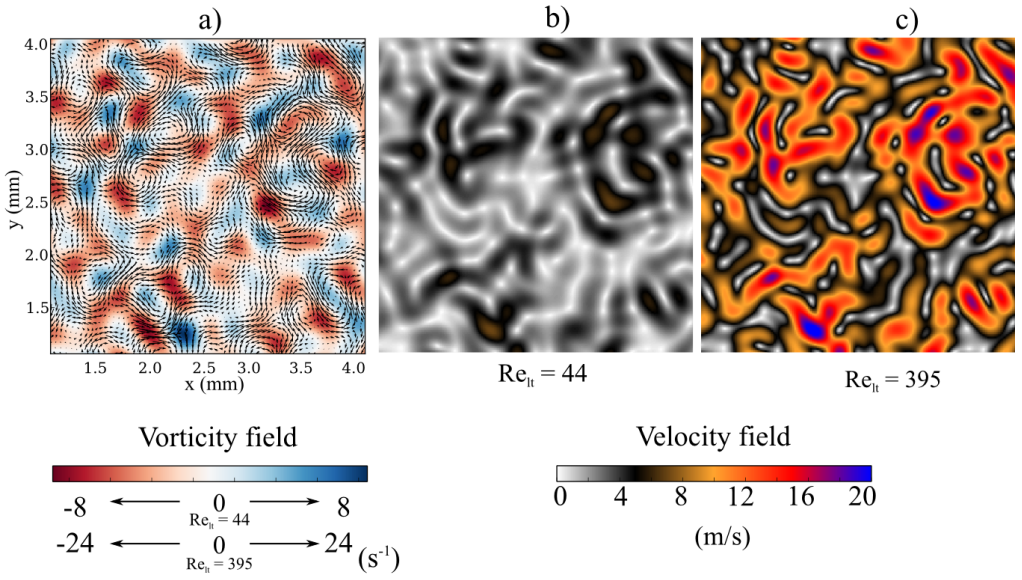

Figure 4.4: *Flow characteristics at the beginning of the computations: a) vorticity field; and velocity field at b) Re_{lt} = 44 and c) Re_{lt} = 395.*

4.4.2 Results and discussion

4.4.2.1 Impact of different turbulence intensities on the plasma-assisted ignition phenomena

Figures 4.5 and 4.6 show the evolution of the gas temperature field for Re_{lt} = 44 and Re_{lt} = 395 simulations, respectively. Four time instants are captured: *a*) at the end of the first discharge (t = 50 ns), *b*) at the beginning t = 100 μs, *c*) at the end of the second discharge t = 100 μs + 50 ns, and *d*) at t = 200 μs. The results show that, although turbulence does not have an impact during the short characteristic time of the discharge (τ_{pulse} = 50 ns), it impacts the temperature field between two consecutive discharges. As shown in Fig. 4.5, at low turbulent Reynolds number, Re_{lt} = 44, after the first discharge the temperature field is not much affected by the turbulence, yielding a homogeneous hot spot formation during the second discharge, shown in Fig.4.5c. In this case, the evolution of the maximum gas temperature and species concentrations inside the discharge zone are close to those observed in quiescent conditions shown in Fig. 4.1 and Fig. 4.2, respectively. Therefore, as in the

quiescent case, at $\mathrm{Re}_{lt} = 44$ the mixture also ignites after two pulses.

However, at higher turbulent Reynolds number the simulation results presented in Fig. 4.6 for $\mathrm{Re}_t = 395$, show that the hot spot created during the first discharge is stretched and engulfed by the surrounding fresh gases due to the turbulence. By the time of the second pulse at $t = 100$ μs (Fig. 4.6b), the thermochemical conditions inside the discharge zone are not homogeneous anymore and, in some locations inside the discharge channel they are even similar to those seen by the first pulse. Thus, it clearly shows that when repetitively-pulsed discharges are applied at pulse frequencies lower than 10 kHz in turbulent flows at Reynolds number of the order of $\mathrm{Re}_{lt} = 395$, the cumulative effect of multiple pulses on the temperature increase is drastically reduced. In fact, in conditions of forced turbulence, the thermochemical conditions seen by repetitively-pulsed discharges may always be those of fresh gases. In this case, unless ignition occurs after a single pulse, at an expense of a higher energy deposition, at these turbulence levels, mixture is unlikely to ignite. Nevertheless, in the present study as the turbulence intensity decays and as the cumulative effect of multiple pulses becomes more significative, mixture ignites after 4 discharges as seen in Fig. 4.7.

Figure 4.8 also shows the impact of the turbulence on the evolution of the *a*) CH_2O and *b*) vibrational energy concentrations at $Re_{lt} = 395$ conditions. Simulation results are captured at 6 instants, the left columns of both Figs. 4.8a and b, refer to the conditions at the beginning of the second, third and fourth pulses, whereas the right columns refer to the conditions at the end of each of these pulses.

Although some species such as O and OH radicals still recombine quickly within two consecutive discharges, Fig. 4.8a shows that CH_2O is being accumulated and spread around the discharge zone within each pulse interval. The vibrational energy is also transported by the turbulence towards regions where the gas temperature and the O radicals concentra-

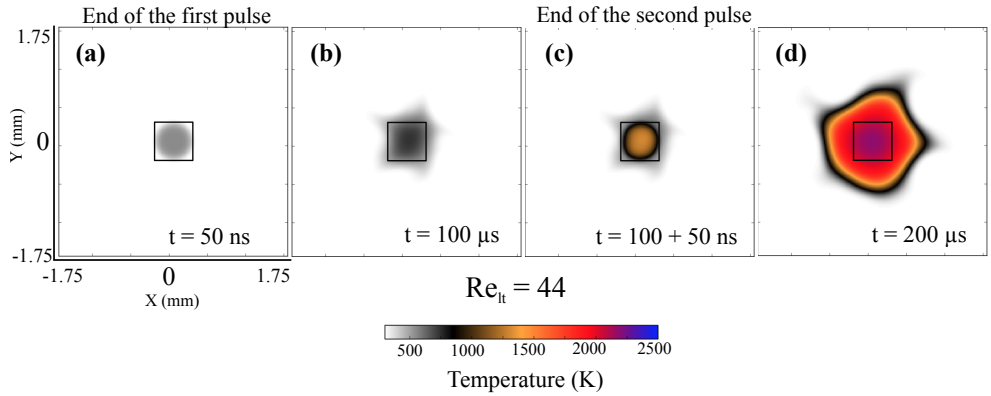

Figure 4.5: *Impact of turbulence on the temporal evolution of the gas temperature in the near-field of the discharge zone for a turbulent flow characterised by Re_{lt} = 44. The time instants captured correspond to (a) the end of the first discharge t = 50 ns, (b) the beginning of the second discharge t = 100 µs, (c) the end of the second discharge t = 100 µs + 50 ns and (d) t = 200 µs.*

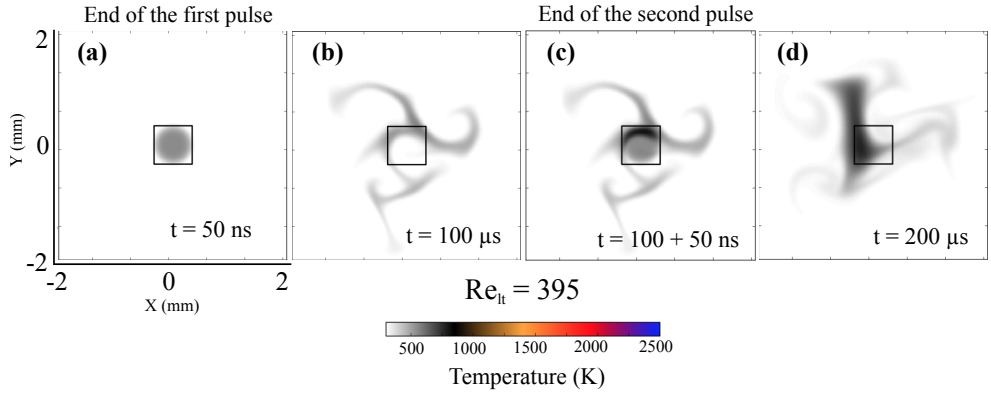

Figure 4.6: *Impact of turbulence on the temporal evolution of the gas temperature in the near-field of the discharge zone for a turbulent flow characterised by Re_{lt} = 395. The time instants captured correspond to (a) the end of the first discharge t = 50 ns, (b) the beginning of the second discharge t = 100 µs, (c) the end of the second discharge t = 100 µs + 50 ns and (d) t = 200 µs.*

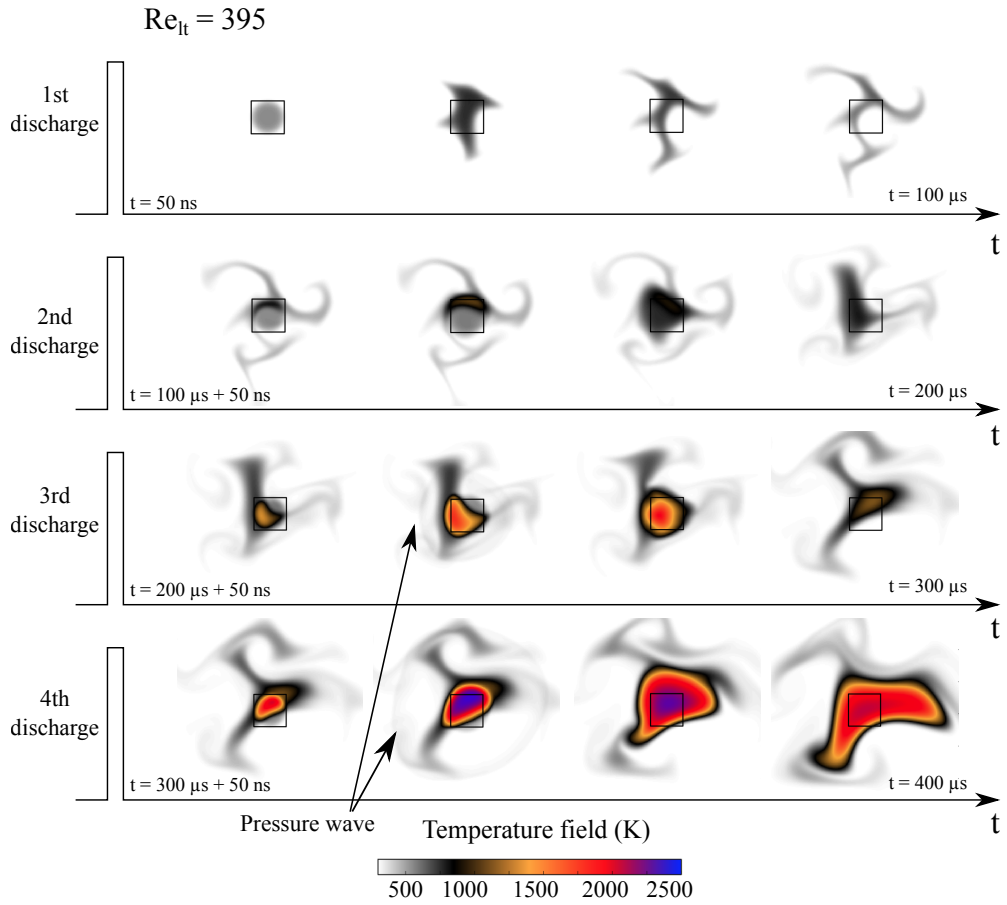

Figure 4.7: *Impact of turbulence on temperature field at $Re_{lt} = 395$. Four time instants are captured within each pulse period for a sequence of four discharge pulses. Mixture ignition occurs only after four discharge pulses.*

tion are too low to induce its relaxation into gas heating and, therefore, its contribution to the mixture ignition becomes less important.

All these turbulence effects lead to an increase of the number of pulses needed to ignite the mixture. In this simulation ($Re_{lt} = 395$), characterized by a given initial distribution of the velocity field, four discharge pulses are needed to ignite the mixture. However, this number may vary for different turbulent events at $Re_{lt} = 395$ as it will be discussed below.

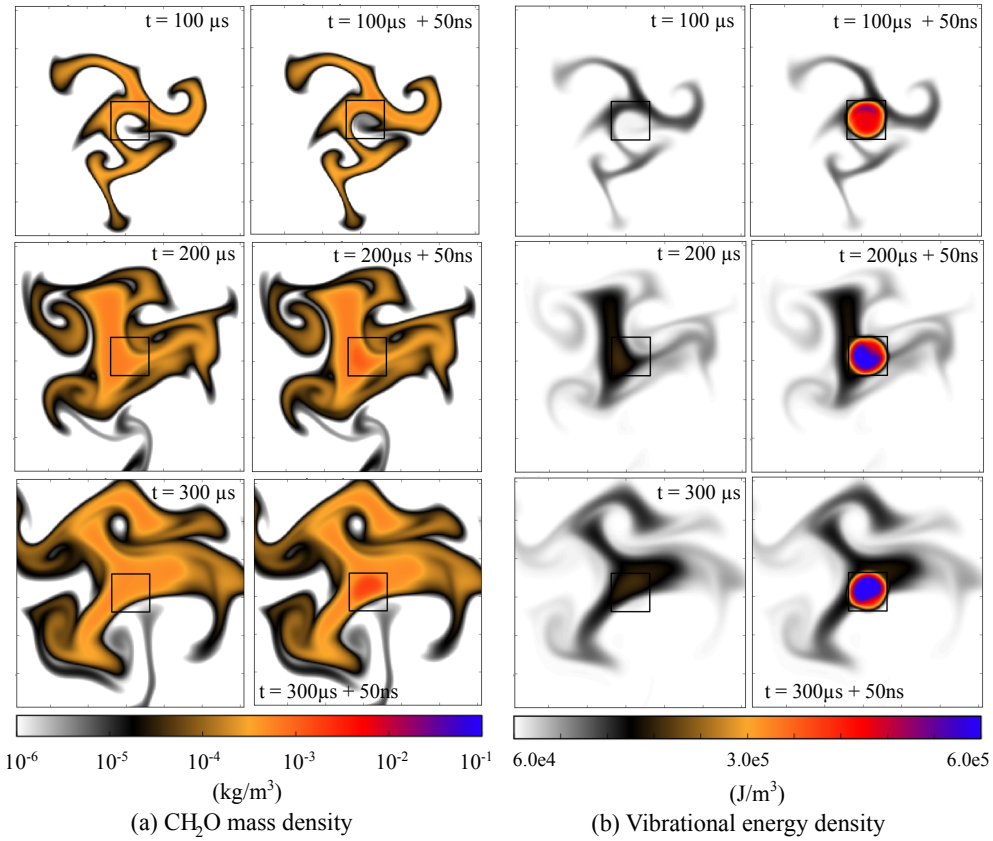

Figure 4.8: *Impact of turbulence on CH_2O mass density and gas vibrational energy density at the beginning and at the end of three consecutive discharges.*

4.4.2.2 Impact of the initial distribution of the turbulent eddies relative to the discharge channel

To mimic the chaotic nature of the turbulence and to better understand the ignition phenomena under repetitively-pulsed discharges in turbulent conditions, four distinct turbulent events are simulated. Figure 4.9 shows the vorticity fields of each of these four turbulent events where the same Reynolds number of $\mathrm{Re}_{lt} = 395$ is retained in all cases. As shown in Figs. 4.9, each turbulent event is characterized by a given spatial distribution of the turbulent eddies relative to the discharge zone (represented by the black square) at the beginning of the computations.

Figures 4.10 shows the simulation results of each of these initially im-

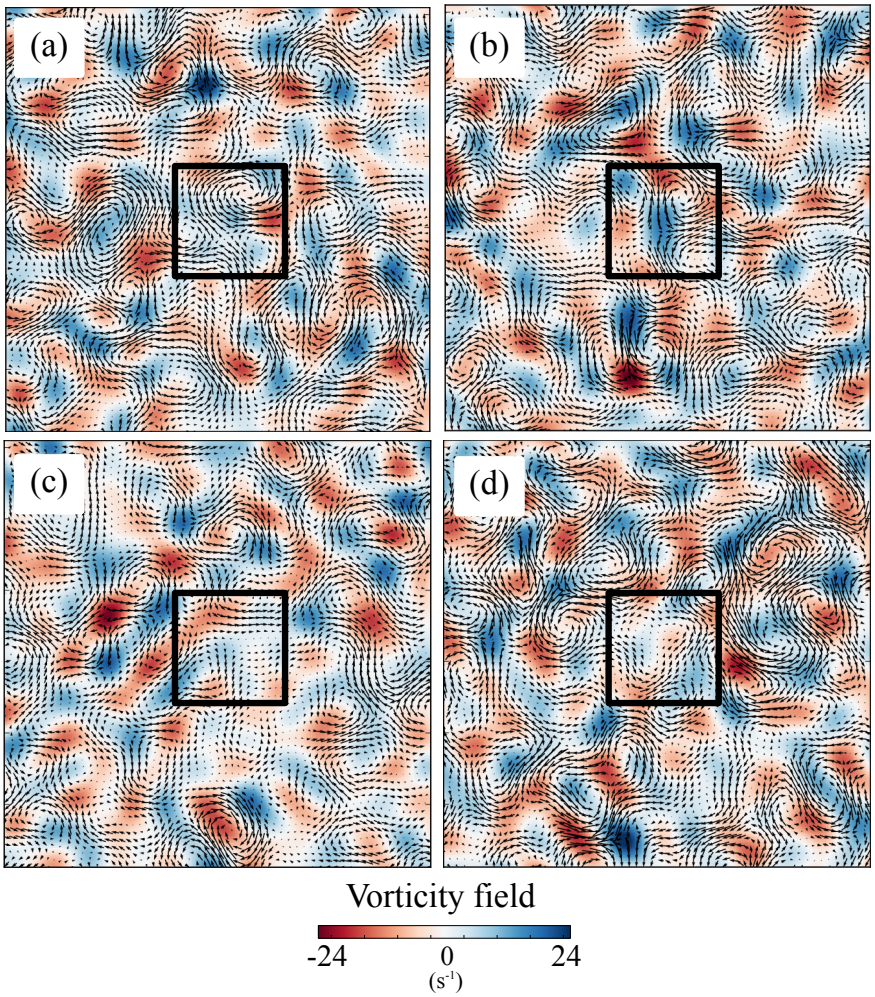

Figure 4.9: *Initial vorticity fields in four turbulent events characterized by the same turbulent Reynolds number $Re_{lt} = 395$. The initial spatial distribution of the turbulent eddies, relative to the discharge zone (identified by the black square), is changed at the beginning of the computations.*

posed vorticity fields. In each subfigure, the temporal evolution of three different temperatures are compared:

- the maximum value of the gas temperature in the domain (not fixed in space, it can be transported by the turbulence);
- the gas temperature at the centre of the discharge channel (fixed in space);
- the maximum value of the gas temperature in quiescent conditions

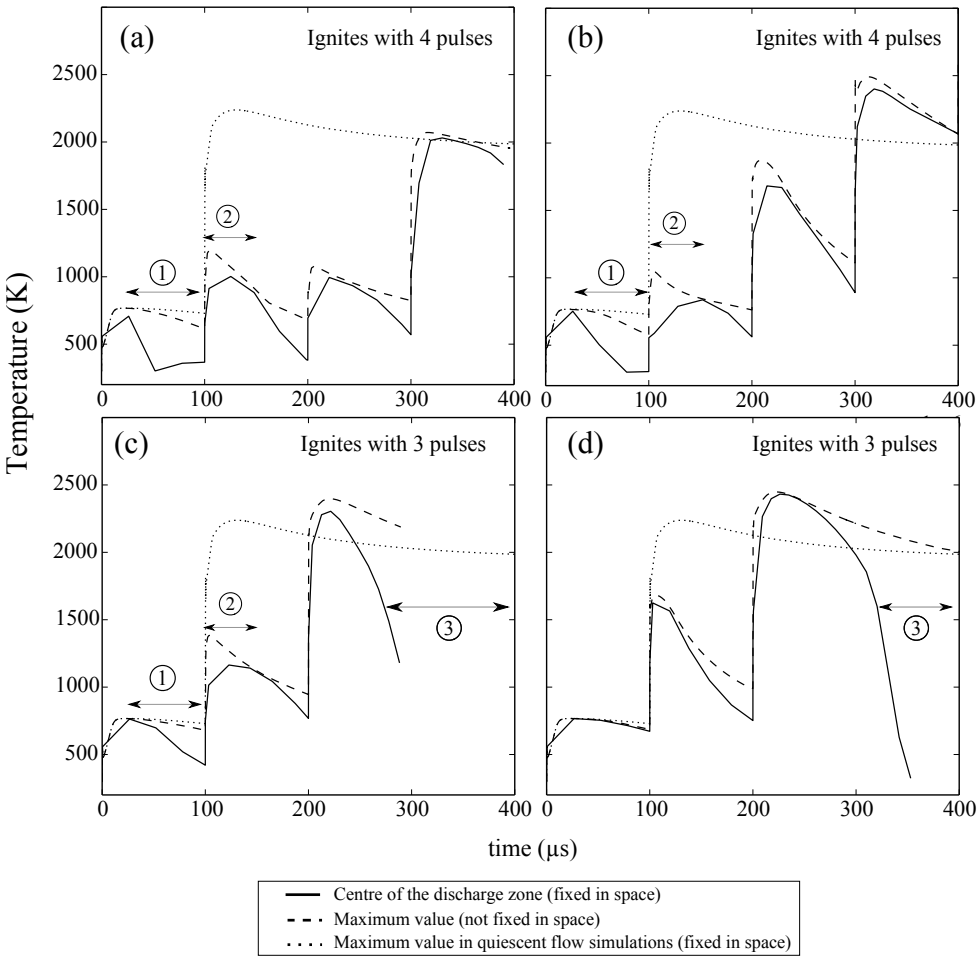

Figure 4.10: *Temporal evolution of the maximum value of gas temperature inside the computational domain (dashed lines) and gas temperature at the centre of the discharge zone (solid lines) in four different initial conditions of the velocity field. Results are compared to quiescent flow condition (dotted lines).*

(fixed in space, this evolution of the gas temperature in quiescent conditions was already discussed and presented in Fig. 4.1 for $\eta = 0.35$, it is reproduced here for comparison purposes).

In the simulations presented in Figs. 4.10a and b mixture ignites after 4 discharge pulses, whereas in the simulations presented in Figs. 4.10c and d, mixture ignites after 3 discharge pulses. In all simulations, within $t = 0$ - 100 μs, the maximum value of the gas temperature in the domain is not much different from the one in quiescent simulations, thus showing

a minor impact of the diffusion within the pulse interval $\Delta t = 100\ \mu s$. Yet, the gas temperature at the centre of the discharge channel drops significantly within the timespan $t = 0 - 100\ \mu$s in Figs. 4.10a, b and c (see the timespan identified by 1). This means that, the hot spot created by the first pulse is convected away from the discharge zone between the first and the second pulses. Consequently, at the moment of the second discharge, the gas temperature seen by the pulse at the centre of the discharge channel is close to the fresh gas temperature. Indeed, as shown in Figs. 4.9a, b and c, the vorticity inside the discharge zone in these cases is more intense than that observed in the case of Fig. 4.9d. In this latter case, the vorticity is almost zero inside the discharge zone and, therefore, turbulence is less effective on the convection of the initial hot spot away from the centre of the discharge zone. This is observed in Fig. 4.10d by comparing the values of the maximum gas temperature and the one at the centre of the computational domain at $t = 100\ \mu$s.

In the timespan identified by 2 in Figs. 4.10a, b and c, the results show that the gas temperature at the centre of the discharge increases again in two steps. The first step occurs within the pulse characteristic time and is due to the ultrafast gas heating phenomena of the non-equilibrium plasma. The second step, occurring within $t \approx 101 - 120\ \mu s$, is explained by the turnover of the high-temperature hot spots (that were convected around the discharge zone during the first pulse interval) from outside into the discharge zone, as well as by the enhancement of exothermal reactions at the centre of the discharge zone. Indeed, the maximum value of the gas temperature in the domain matches the one at the centre of the discharge at $t \approx 120\ \mu s$.

Finally, the results presented in Fig. 4.10d show that the mixture does not ignite after the second pulse even though the value of the gas temperature at the centre of the discharge is close to the one of the quiescent flow simulations at $t = 100\ \mu$s. As already discussed in the quiescent case, radicals concentrations play a major role on mixture ignition. As was also

discussed, at higher turbulent Reynolds numbers, CH_2O (*see* Fig. 4.8a), and other intermediate combustion species such as CO and CO_2, are being accumulated and spread around the discharge zone. Therefore, their concentrations inside the discharge zone are necessarily lower than those observed in the quiescent case. Moreover, the simulations were performed considering Le $\neq 1$ and so, the heat and the species diffusivities are not the same.

Another important observation is that, under turbulent conditions, the vibrational energy is also being spread around the discharge channel. Thus, as the relaxation of the vibrational energy will occur over a larger domain, its local concentration inside the discharge zone also decreases. Therefore, the amount of the vibrational energy that contributes to the gas heating inside the discharge zone will be smaller than that observed in the quiescent case, vibrational relaxation occurs mostly during τ_{pulse}. Regarding the results presented in Fig.4.10 and also those obtained in the quiescent conditions case in Fig. 4.1, ignition has always occurred right after a given discharge but before the expansion of the gas which occurs at $\tau \approx 0.25\ \mu s$ after each single discharge pulse (discussed in chapter 3 in the 2-D DNS of NRP discharges in air). Therefore, if the local ignition delay time τ_{ig} computed with the local gas temperature and chemical composition at the end of the discharge pulse does not fulfill the criteria of $\tau_{ig} < 0.25\ \mu$s, the gas will first expand. The gas expansion may results in a temperature decrease to values below the one needed to ignite the mixture. In these conditions, mixture will not ignite. These small variations of the thermochemical conditions seen by the pulses, in comparison with those in quiescent case, can explain the ignition failure in the case of Fig. 4.10d at $t = 100\ \mu$s. Another possible explanation is the thinner spatial extent of these favorable thermochemical conditions compared to that in the quiescent case. Indeed, while in the quiescent case the hot spot conserves its spatial round-form, in turbulent flows the hot spot is stretched into a narrowed heated zone while still keeping the values of the gas temperature and species concentrations found at the end of the first

pulse. In a narrowed heated zone, assuming that the criteria $\tau_{ig} < 0.25$ μs is fulfilled and a first ignition event occurs, the diffusive heat losses can be more or as important as the heat released through initial exothermal combustion reactions. In this case ignition may also fail.

After a successful ignition event, an initial kernel is formed and either develops into a sustainable flame kernel or extinguishes due to heat losses. The decrease of the gas temperature in the centre of the discharge channel observed in Figs. 4.10c-d after a successful kernel formation (*see* the timespan identified by 3) shows the impact of the turbulence on the convection of these initial flame kernels.

4.5 Conclusions

In this chapter we analyzed the plasma-assisted ignition phenomena in quiescent and turbulent flow conditions. The physics governing the formation of the ignition kernel in NRP discharges are different from those governing the ignition by a single conventional spark.

In NRP discharges, when ignition occurs after several pulses, the transient thermochemical conditions seen by the pulses must be considered to accurately capture the phenomena. The ultrafast energy deposition is always associated with the gas expansion. By the time of a given discharge, if the thermochemical conditions are not favourable for a first ignition event, before the expansion of the gas, it might be necessary to apply another discharge to successfully ignite the mixture due to the decrease of the gas temperature following the isentropic expansion.

The deposition of part of the discharge energy directly into the dissociation of O_2 molecules increases the mixture reactivity even at low gas temperatures. In quiescent conditions the increase of the chemical reactivity at each pulse results in a significant decrease of the ignition delay and the total energy needed to ignite the mixture. It greatly reduces

the value of the gas temperature threshold of chain-branching reactions by comparison with the case where O atoms are not produced by the discharge. Between pulses, the fast recombination of the O atoms with CH_4 molecules increases the concentration of H and OH radicals which then recombine with other intermediate combustion species. In this sense, plasma-assisted technologies are an efficient way to initiate and enhance the combustion processes. The results have also shown that CH_2O is a long-lasting intermediate ignition species which is being accumulated following multiple discharges. Therefore, CH_2O is a good marker for experimental studies of NRP discharge-assisted ignition.

Under turbulent flow conditions, NRP discharge-assisted ignition is a complex phenomena. In addition to the hot spot-turbulence interactions, the frequency at which pulses are applied also plays a role one the effective ignition kernel formation at high turbulence intensities. The ignition phenomena was studied under two turbulent Reynolds numbers. While at low Reynolds numbers of the order of $\mathrm{Re}_{lt} = 44$ the ignition kernel is not must affected by the turbulence, under higher turbulence intensities the formation the ignition kernel is governed by the extent and the absolute value of the species and vibrational energy concentrations inside the discharge channel. The spatio-temporal evolution of the species concentrations and vibrational energy inside the discharge channel depends on the initial turbulence intensity, the pulse frequency and also on the distribution of the turbulent eddies relative to the centre of the discharge channel. Between pulses, the hot spot created by the former discharge may be stretched or convected by the turbulence yielding a non uniform distribution of the thermochemical conditions inside the discharge zone for the following pulse. If the thermochemical conditions are always those seen by previous pulses, mixture is unlikely to ignite. Therefore, the results suggest that turbulence intensity should be correlated to a given pulse frequency to increase the synergy of consecutive pulses in order to ignite the mixture.

The thermochemical conditions seen by the pulses are key for a successful ignition kernel formation. These conditions are governed not only by the turbulence intensity but also by the 3-D recirculating flow pattern induced by each nanosecond discharge, as will be further discussed in the next chapter.

Chapter 5

Study of the recirculating flow pattern effects inside a reactive kernel produced by nanosecond plasma discharges in a methane-air mixture: 3-D DNS and experiments

This chapter presents a study of the evolution of a kernel produced by a nanosecond plasma discharge. Synchronized numerical and experimental studies unveiled the multidimensional flow pattern generated by a single discharge pulse. Numerical and experimental schlieren images are compared shortly after the pulse and at longer instants. The impact of this flow pattern on the gas temperature and species concentrations, at the center of the discharge channel, is analyzed by means of a 3-D DNS. A comparative analysis of the 3-D and 2-D numerical results is also performed in order to better understand the impact of the intrinsically 3-D flow pattern on the mixture ignition / extinction under NRP discharges conditions.

Contents

5.1 Introduction

For conventional spark discharges, the effects of the gas dynamics on the ignition and flame kernel propagation have already been widely studied. A pioneering study is presented by Kono et al. (1988) where the process of formation of hot kernels by short duration sparks (about 300-nanosecond duration) is analyzed. In this work, 2-D axysymmetrical numerical simulations were performed in inert gas conditions. The gas temperature and pressure were imposed in the inter-electrode region as initial conditions. The authors assumed thermal equilibrium conditions and that only a small fraction of the discharge energy was instantaneously deposited into gas sensible energy. Initial values of the gas temperature and pressure were determined from the experimental shock wave velocity. The evolution of the hot kernel shape obtained from the computed temperature fields (shown in Fig. 5.1) was compared with experimental schlieren images after a spark discharge in air (shown in Fig.5.2) and in a propane-air mixture. The results showed that the gas flow produced after the shock wave resulted in specific kernel configurations, depending on the gap distance. For an inter-electrode gap of about 1 mm, the initially cylinder-shaped hot kernel turned into a toroidal shape. Despite the limited spatial derivatives discretization and temporal integration used in the numerical simulations, and the low gas temperature obtained in the simulations compared with those typically found after spark discharges, the results reproduced fairly well the hot kernel shape obtained in the experiments.

Thiele et al. (2000)a and Thiele et al. (2000)b have numerically studied the entrainment of fresh gases into the discharge channel following a spark discharge. In this study, ionization processes and different electrode geometries were considered. The results also showed that the blast wave generated by these spark discharges induced a flow recirculation in the vicinity of the discharge channel and impacted the ignition kernel topology.

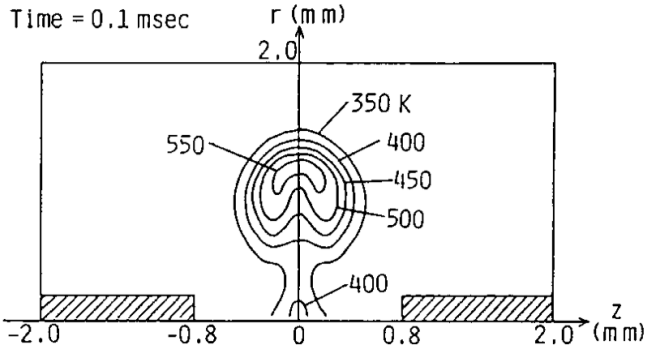

Figure 5.1: *Numerical results of the temperature distribution in the spark gap at t = 100 μs. Spark gap of 1.6 mm. Reproduced from Kono et al. (1988).*

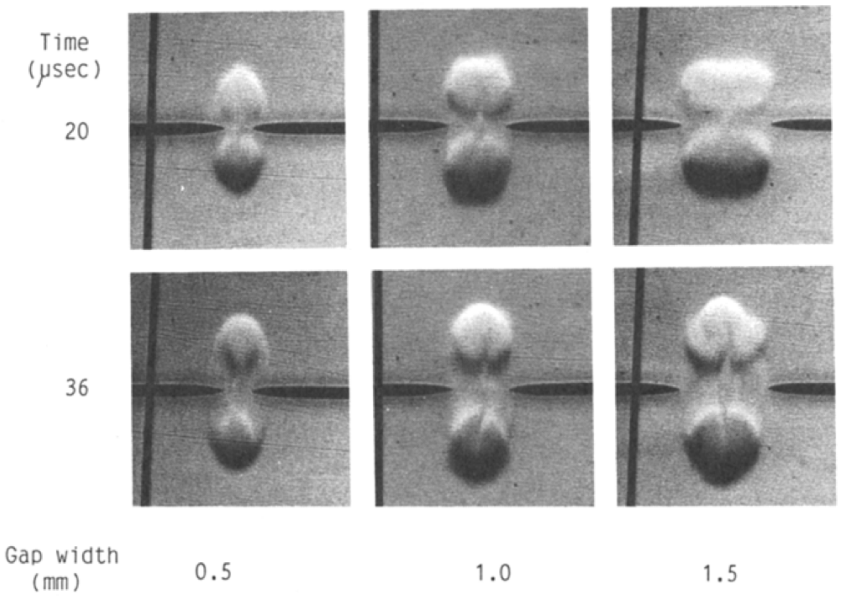

Figure 5.2: *Schlieren photographs taken by 5×10^5 fps movie in air. Spark energy: 4.6 mJ. Reproduced from Kono et al. (1988).*

These effects have also been observed experimentally for instance by Bradley et al. (2004) and Cardin et al. (2013) in laser-induced spark ignition. It was shown that the shock wave generated by a laser-beam source played an important role in ignition by modifying the topology of the initial kernel and leading to the formation of a third lobe. As discussed in Bradley et al. (2004), the formation of this third lobe in flammable mixtures eventually enhances flame kernel development. Nevertheless, few details on the spatial and temporal evolution of the species are given in these studies.

In NRP discharge-assisted ignition, gas dynamics have not been fully studied yet. The energy deposited by a NRP discharge of about 1 mJ is one to two orders of magnitude lower than that deposited by laser-induced breakdown (about 85-200 mJ in Bradley et al. (2004)) or spark ignition (for instance, 4.6 to 9.1 mJ in Kono et al. (1988) and 10-30 mJ in Reinmann and Akram (1997)). Furthermore, at the end of a NRP discharge, the gas temperature is of the order of 2000 K and the pressure ranges from 2 to 5 bar whereas in conventional spark or laser-induced breakdown discharges, gas temperatures are of the order of 10^4 K and gas pressures are of the order of hundreds of bars. Therefore, the shock wave generated by a NRP discharge is comparatively weaker than the ones generated by laser or conventional spark discharges. Nevertheless, as discussed in chapter 4, when ignition occurs only after several NRP discharges, the thermochemical conditions seen by each pulse are key for the ignition process. As previously shown in chapter 4, these conditions seen by the pulses are affected by turbulence. Thus, it is also important to analyze the evolution of these conditions under the recirculating flow pattern induced by each single NRP discharge.

Therefore, the objective of the present chapter is to identify to what extent the shock wave generated by a single nanosecond plasma discharge modifies the kernel topology and impacts the species concentrations and

the gas temperature at the center of the discharge channel. To this end, a 3-D DNS is performed using the detailed combustion chemistry and the plasma model developed in chapter 2. A sequence of instantaneous computational and experimental schlieren images are compared, following the nanosecond discharge in a methane-air mixture. The evolution of the velocity and temperature fields as well as species concentrations radial profiles are then analyzed.

It is noteworthy to mention that the recirculating flow pattern following a NRP discharge was first observed in 3-D DNS of a single pulse in air. A synchronized numerical and experimental work was then performed leading to the results presented in this chapter.

5.2 Test-case description

5.2.1 Experimental set-up

The schematic representation of the combustion chamber and the electric circuit used for the experimental study is given in Fig. 5.3 adapted from Xu et al. (2015). Nanosecond discharges in pin-to-pin geometry were initiated in air and in a lean methane-air mixture (ϕ=0.7) at pressure of p = 1 atm and temperature of T = 300 K. The gap between the pins was 1 mm for all the presented experimental results. The voltage pulses applied to the electrodes were produced by a FID Technology FPG 30-100MS pulse generator. The pulses had 20 ns duration and a few tens of kV in amplitude.

The electrode system was mounted inside a constant volume chamber (V = 100 cm^3) in order to perform the experiments in the methane-air mixture. Two sapphire optical windows of 5 cm diameter each were installed into the chamber walls to provide access for optical diagnostics. For each discharge, the voltage and the current signals were measured with a LeCroy high-voltage probe and a Pearson coil (model 6585), re-

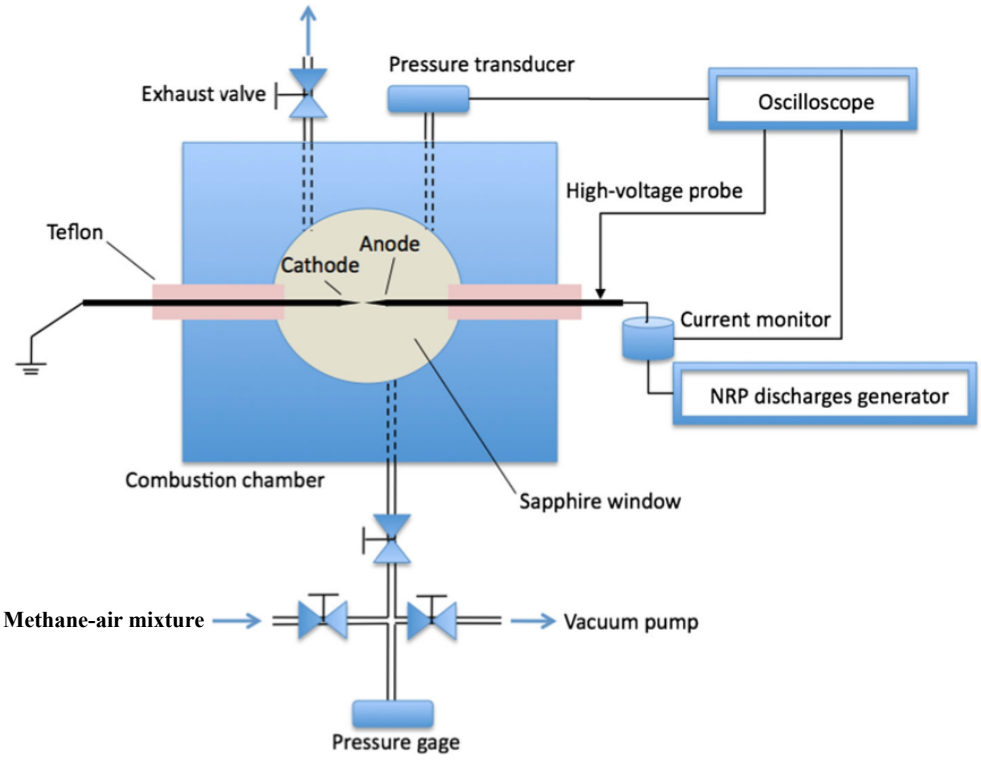

Figure 5.3: *Schematic representation of the combustion chamber and the electric circuit used in the present study. Adapted from Xu et al. (2015).*

spectively. Both signals were recorded with a 1 GHz Lecroy WavePro 7100A oscilloscope. Typical voltage and current temporal evolutions for the presented experimental results in air are shown in Fig. 5.4. The discharge energy, calculated from the profiles, is approximately 1.4-1.5 mJ for both air and methane-air mixtures. The schlieren technique was used to monitor the temporal evolution of the gas density distribution after the nanosecond discharge. Phase-locked schlieren images were obtained using a high-power diode laser light source CAVILUX HF and a Pi-Max4 CCD camera, with 512 × 512 pixel resolution. The schlieren system used in the present work is described in detail in Xu et al. (2015).

5.2.2 Numerical set-up

Figure 5.5 shows a schematic representation of the 2-D and 3-D computational domains. A 3-D cube with length of each side $L = 3.24$ mm was discretized with 256 non-uniformly distributed grid points. The grid spacing distribution is shown in Fig. 5.5b. The mesh size is around 10 μm inside the discharge channel. The overall domain contains 16.8 million grid points. Nonreflecting outflow NSCBC boundary conditions were imposed in all directions so that the pressure wave generated by the pulse is not reflected at the boundaries back into the computational domain. Electrode surfaces are not taken into account in the computational domain.

For both the air and the methane-air cases, the initial gas pressure and temperature are 1 atm and 300 K, respectively. For the reactive case, a quiescent mixture of methane-air with an equivalence ratio of 0.7 is uniformly distributed over the computational domain, at the beginning of the computations. The detailed combustion mechanism of Lindstedt (1998) with 29 species and 141 elementary reactions is used.

The spatial function $\mathcal{F}$, which defines the shape and the location of the discharge energy deposition in the computational domain is given by

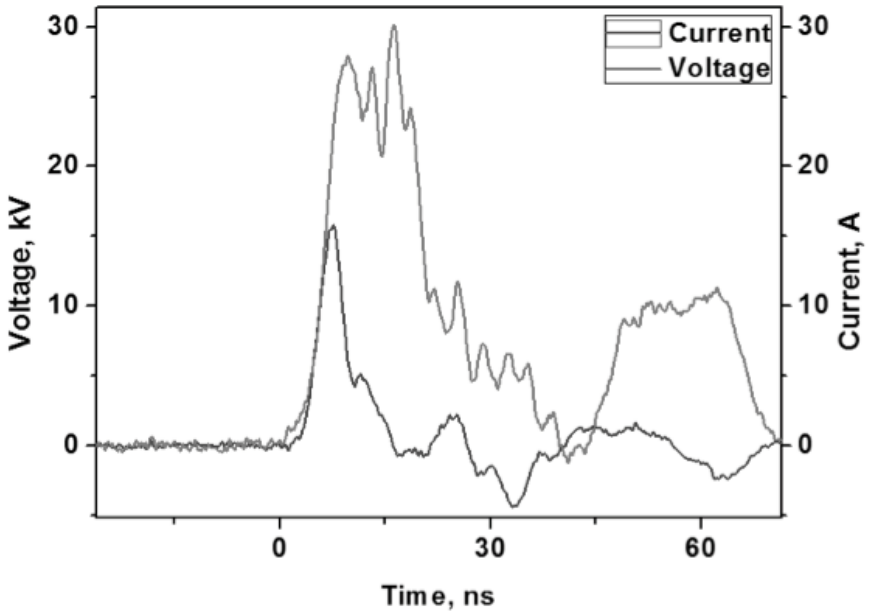

Figure 5.4: *Measured voltage and current waveforms during and after a single discharge in air.*

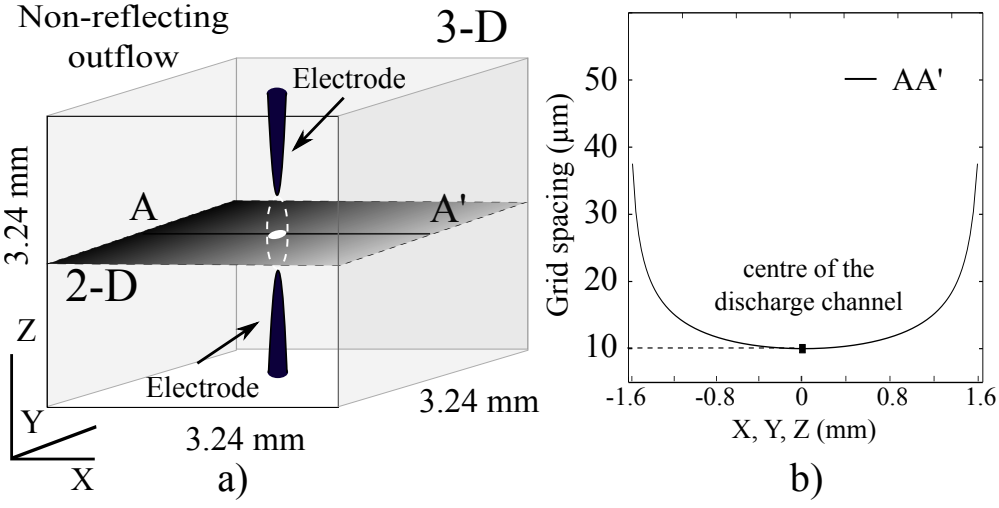

Figure 5.5: *Schematic representation of the 3-D computational domain used in the present work: a) solution domain and boundary conditions. b) mesh size distribution over the line AA′.*

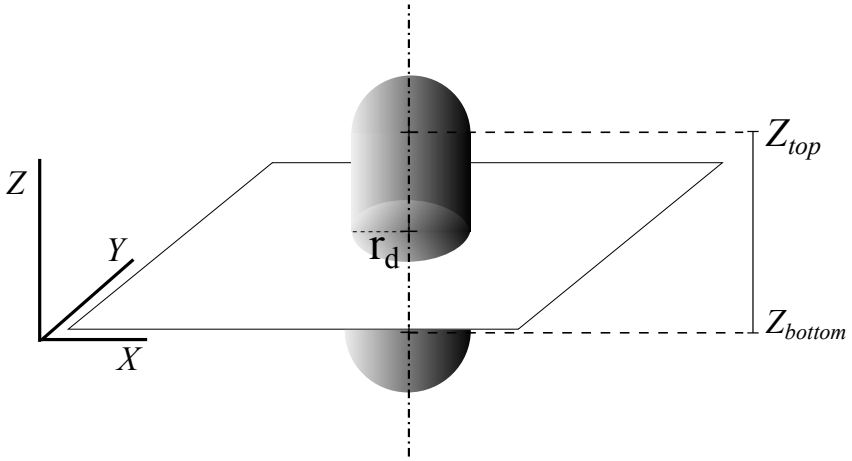

Figure 5.6: *Schematic representation of the shape and the location where the energy of the discharge is deposited in the 3-D computational domain.*

Eq. (3.1) of chapter 2:

$$\mathcal{F}(r) \;=\; \mathrm{erfc}\left(\frac{r^2}{a}\right)^b \tag{5.1}$$

where $a = 690{\times}10^{-10}$ m and $b = 5/2$. The values of these geometric parameters are fitted to model the experimental discharge radius $r_d = 225$ μm and a discharge length of $L_d = 1$ mm.
The value of r is defined in the 2-D and 3-D domain as follows:

- In the **2-D DNS**:

$$r^2(x, y) = (x - x_0)^2 + (y - y_0)^2 \tag{5.2}$$

  where x_0, y_0 are the coordinates of the center of the discharge channel.

- Figure 5.6 shows a schematic representation of the geometric parameters used to define r in the **3-D DNS**:

$$r^2(x,y,z) = \begin{cases} (x-x_0)^2 + (y-y_0)^2 & \text{if } z_{bottom} < z < z_{top} \\ (x-x_0)^2 + (y-y_0)^2 + (z-z_{top})^2 & \text{if } z \geq z_{top} \\ (x-x_0)^2 + (y-y_0)^2 + (z-z_{bottom})^2 & \text{if } z \leq z_{bottom} \end{cases} \quad (5.3)$$

where x_0, y_0 and z_0 are the coordinates of the center of the discharge channel in the 3-D computational domain. This spatial function $\mathcal{F}$ defines, therefore, a discharge channel as a cylinder within z_{bottom} and z_{top} and half-spheres at $z \geq z_{top}$ and $z \leq z_{bottom}$.

The discharge energy power $\dot{E}^p(t)$ is then given by Eq. (2.57) defined in chapter 2:

$$\dot{E}^p(t) = \begin{cases} \frac{\sigma_{pulse}}{\tau_{pulse}} \cdot \mathcal{F} & \text{if } t \leq \tau_{pulse} \\ 0 & \text{if } t > \tau_{pulse} \end{cases}$$

where σ_{pulse} is the discharge energy per unit volume of a single pulse and $\tau_{pulse} = 50$ ns is the characteristic time of the discharge, as defined in chapter 2.

5.2.3 Validation of the discharge energy deposited in the numerical simulations

As discussed in Xu et al. (2014), the evolution of the pressure wave and hot kernel radius early after the discharge pulse is a function of the gas temperature inside the discharge channel and the energy transferred through ultrafast gas heating. As will be discussed in the results, the gas recirculation intensity increases with the fraction of the pulse energy transferred into ultrafast gas heating. For simplicity, we keep the same values of $\alpha = 0.55$ and $\eta = 0.35$ as defined in chapter 2, and we adjust the total deposited energy in order to correctly predict the experimental pressure wave and hot kernel evolution at the first instants. Figure 5.7 shows the temporal evolution of the pressure wave and hot kernel radius at early instants after the discharge in air and methane-air mixtures. Good agreement between the experimental and numerical hot kernel radius is

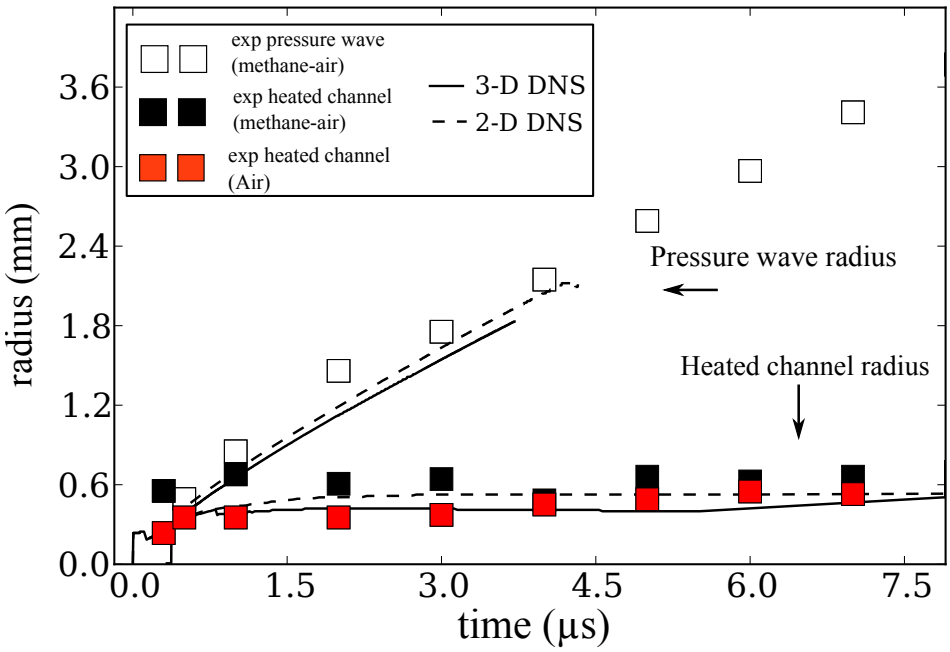

Figure 5.7: *Temporal evolution of the pressure wave and hot kernel radius at early instants after the discharge pulse. Symbols: experiments; Lines: computations.*

obtained for an energy deposition of 0.8 mJ, which agrees reasonably well with the measured deposited energy of 1.4-1.5 mJ.

5.3 Results

5.3.1 Flow dynamics induced by a single pulse discharge

Figure 5.8a shows side-by-side experimental (left-half) and computational (right-half) schlieren images captured at $t = 0.3$ μs and $t = 2$ μs following the discharge pulse in the methane-air mixture. In both experimental and numerical images, the black and grey zones are representative of maximum and zero gradients of the gas density in the x-axis direction, respectively. We define the extent of the hot kernel generated by the plasma discharge as the distance from the maximum value of the gas density gradient (identified by the red square in Fig. 5.8a)to the center of

the discharge channel ($x = 0$).

The ultrafast energy deposition leads to an ultrafast increase of the gas temperature and pressure inside the discharge zone. Figure 5.8a shows that, up to $t \approx 0.3$ μs, the hot kernel radius remains approximately equal to the discharge radius. After the ultrafast increase of the gas pressure, the gas expands. At $t \approx 0.3$ μs, a blast wave detaches from the central hot core and propagates outwards through the surrounding mixture. At $t = 2$ μs, computational and experimental results show the perturbation of the gas density associated with this blast wave (the contrast of the image in print is too low to distinguish the measured shock wave, but its radius is about 1.5 mm at $t = 2$ μs, as shown in Fig. 5.7), as well as the increase of the hot kernel radius due to the gas expansion.

Figure 5.8b shows the simulation results of the flow streamlines superimposed with the gas temperature fields at the same instants as in Fig. 5.8a. During the pulse, the ultrafast energy deposition into gas heating leads to an increase of the gas temperature from $T = 300$ K up to $T = 2100$ K. The temperature then decreases after the gas expansion and at t = 2 μs the gas temperature is about 1500 K at the center of the discharge channel. Because the pulse energy is deposited inside a cylinder-shaped channel, the fluid motion induced by the blast wave in the x-axis direction is stronger than that along the z-axis, as shown at $t = 2$ μs.

Figure 5.9 presents the same experimental and numerical plots of Fig. 5.8 but at $t = 9$, 80 and 200 μs after the discharge pulse. Due to the initial flow asymmetry observed in Fig. 5.8b at $t = 2$ μs, four recirculation zones are created, leading to the entrainment of fresh gas into the discharge channel. The maximum value of the flow velocity is found in the near-field of the electrodes where the flow accelerates towards the center of the discharge channel. The maximum value of the velocity magnitude is about 15 m/s at $t = 9$ μs and decreases to 6.8 m/s at $t = 200$ μs. The gas temperature at the center of the discharge decreases from 2000 to 600

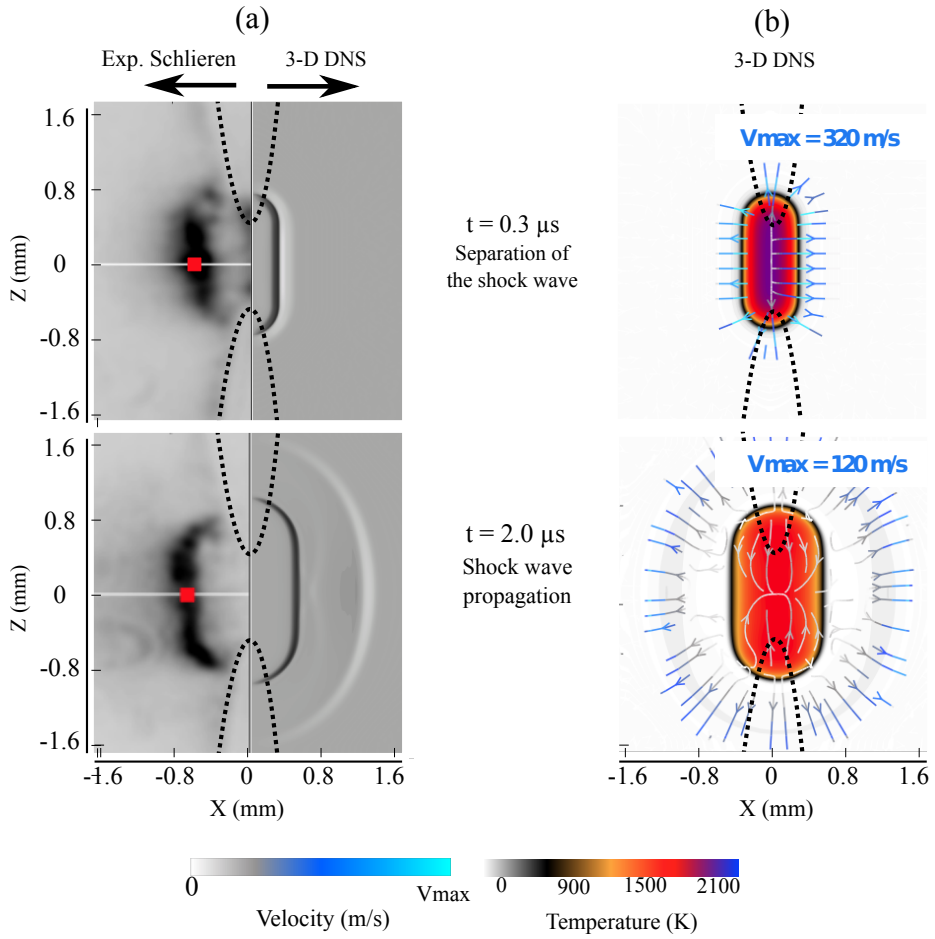

Figure 5.8: *Hot kernel topology captured at $t = 0.3$ µs and $t = 2$ µs after the plasma discharge in methane-air mixture: a) Experimental (left-half) and computational (right-half) schlieren images. b) Superposition of the computed gas temperature field and flow streamlines coloured by velocity magnitude. The same color map of velocity magnitude is used in for all images shown here, but the maximum value V_{max} varies and is indicated above each image.*

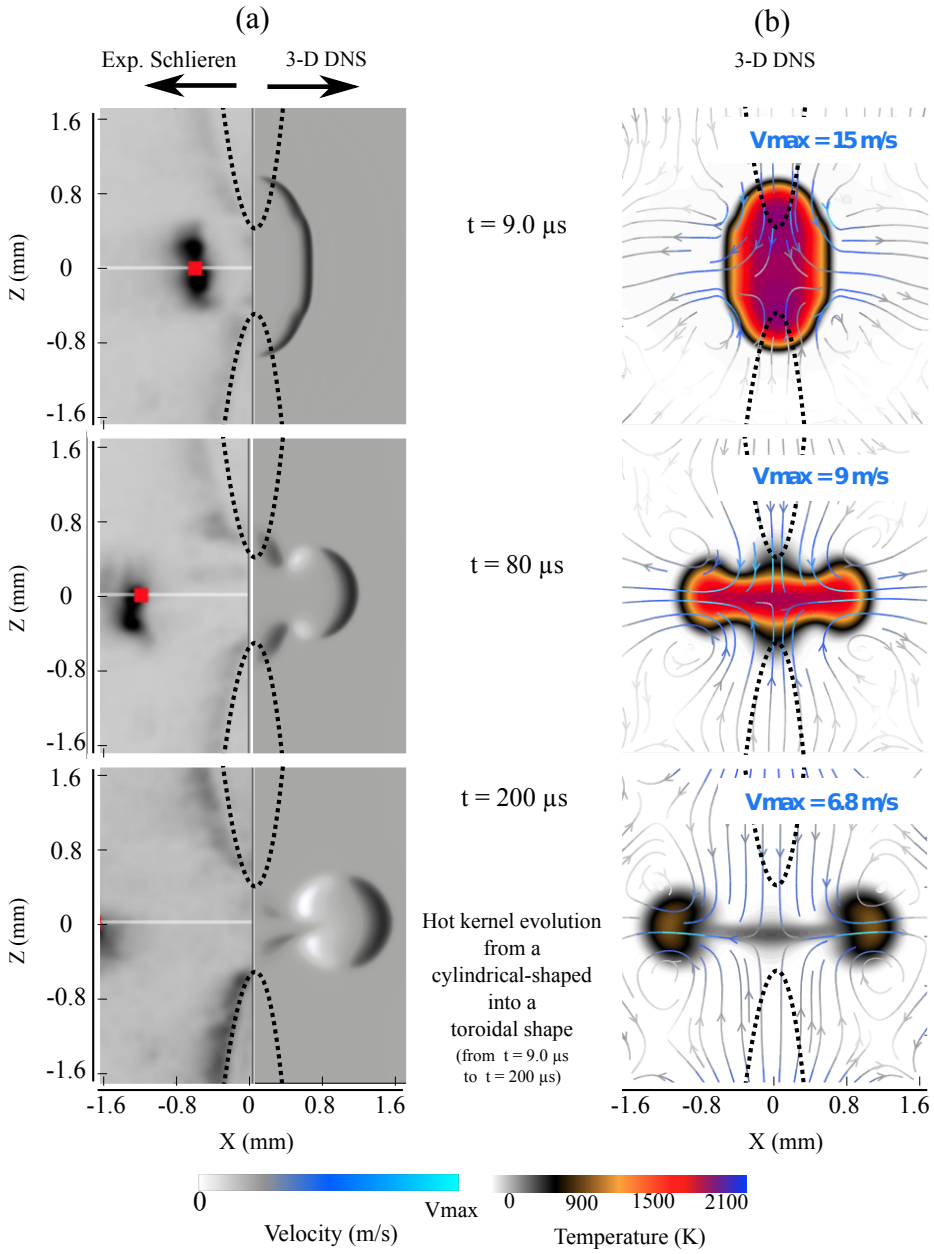

Figure 5.9: *Hot kernel topology captured at $t = 9\ \mu s$, $t = 80\ \mu s$ and $t = 200\ \mu s$ after the plasma discharge in methane-air mixture: a) Experimental (left-half) and computational (right-half) schlieren images. b) Superposition of the computed gas temperature field and flow streamlines coloured by velocity magnitude. The same color map of velocity magnitude is used in for all images shown here, but the maximum value V_{max} varies and is indicated above each image.*

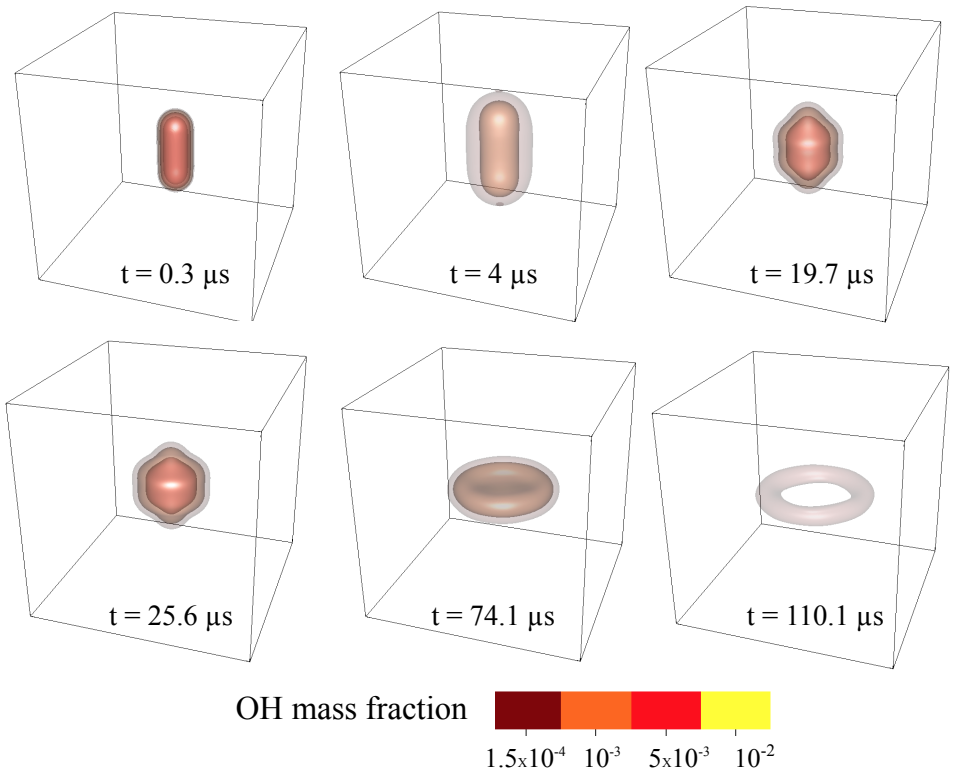

Figure 5.10: *3-D plot of the OH mass fraction at 6 instants following the discharge pulse. The initial cylinder-shaped hot kernel evolves into a toroidal shape.*

K between $t = 9$ μs and $t = 200$ μs mainly due to the gas recirculation, and the initially cylinder-shaped hot kernel (at $t = 2$ μs) evolves into a toroidal shape. The flow pattern resembles a counterflow with a stagnation plane at $z = 0$. Fig. 5.10 shows the 3-D plot of the OH mass fraction at 6 time instants. The evolution of the hot kernel from a cylinder-shaped into a toroidal shape is clearly visible in this figure.

Figures 5.8 and 5.9 show that the numerical simulations match the temporal evolution of the experimental hot kernel extent until well after the end of the discharge pulse.

To evaluate these 3-D effects of gas recirculation on the hot kernel growth, we performed a 2-D simulation in the plane $z = 0$ (shown in Fig. 5.5). In

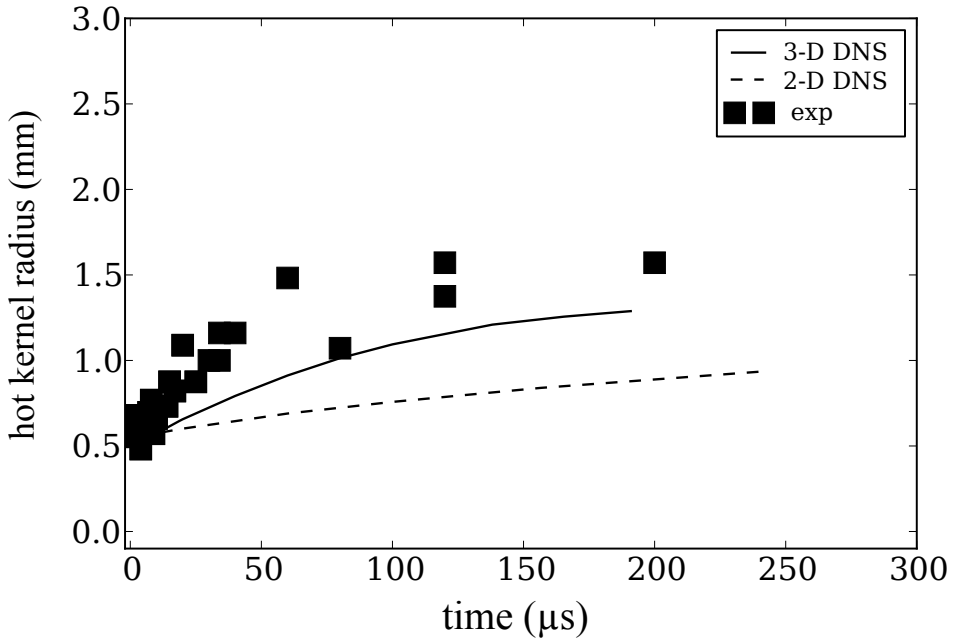

Figure 5.11: *Influence of gas recirculation on the evolution of the hot kernel radius . – With gas recirculation (3-D DNS), - - Without gas recirculation (2-D DNS).*

this 2-D simulation, there is no influence of the gas recirculation on the kernel growth, and the kernel growth is only controlled by gas expansion. Figure 5.11 shows the temporal evolution of the hot kernel extent with (3-D DNS) and without (2-D DNS) gas recirculation. The results show that the extent of the hot kernel is significantly underestimated when gas recirculation is not considered. In contrast, the evolution of the hot kernel is much better captured by the 3-D computations. Yet, the absence of the electrode geometry in the computational domain may explain the slower increase of the kernel extent, early after the pulse. On the other hand, the conductive losses to the electrode decrease the gas temperature in the electrode's near-field. This gas temperature decrease, and therefore the decrease of the density gradient in this zone, can slow down the gas recirculation. Nevertheless, 3-D DNS shows an overall good agreement with the experimental results.

5.3.2 Impact of gas recirculation on species and temperature profiles

Figure 5.12 shows the radial profiles in the plane $z = 0$, of major species mass fractions, at 3 different instants. The radial profiles plotted on the left side of Fig. 5.12 refer to the 3-D DNS case (with gas recirculation), whereas the profiles on the right side refer to the 2-D DNS case (without gas recirculation).

The results show that, at $t = 20$ μs, the mixture is ignited at the center of the discharge. They also show that the species radial profiles are similar in the 2-D and 3-D cases, which means that gas recirculation has a minimal impact up to at least $t = 20$ μs. At 80 μs, however, the species radial profiles differ significantly: for the case with recirculation (3-D), the mass fractions of CH_4, HCO and CH_2O increase at the center of the discharge channel, and those of O and OH decrease. This is due to the recirculation flow, which cools down the channel. The mass fractions of O and OH decrease because these species recombine rapidly. CH_2O and HCO, which were initially present only at the edges of the reaction zone, are entrained from the top and bottom zones of the initially cylinder-shaped reaction zone into the central part of the channel and, therefore, their mass fractions increase at the center of the discharge. The results also show that the thin reaction zone, present at $t = 20$ μs around $x \approx$ -0.4 mm, does not continue to propagate through the surrounding fresh mixture afterwards, in contrast to the 2-D case, where the reaction zone successfully evolves into a flame front. In fact, the extinction of the ignited kernel in the 3-D case is due to the low gas temperature upstream of the reaction zone and to an increase of the diffusion heat losses, since the toroidal shape of the 3-D hot kernel has a smaller radius than the cylindrical shape of the 2-D hot kernel. Indeed, the results show that at $t = 138$ μs, if gas recirculation is not taken into account (2-D DNS profiles on right side), the ignition kernel propagates through the surrounding fresh mixture.

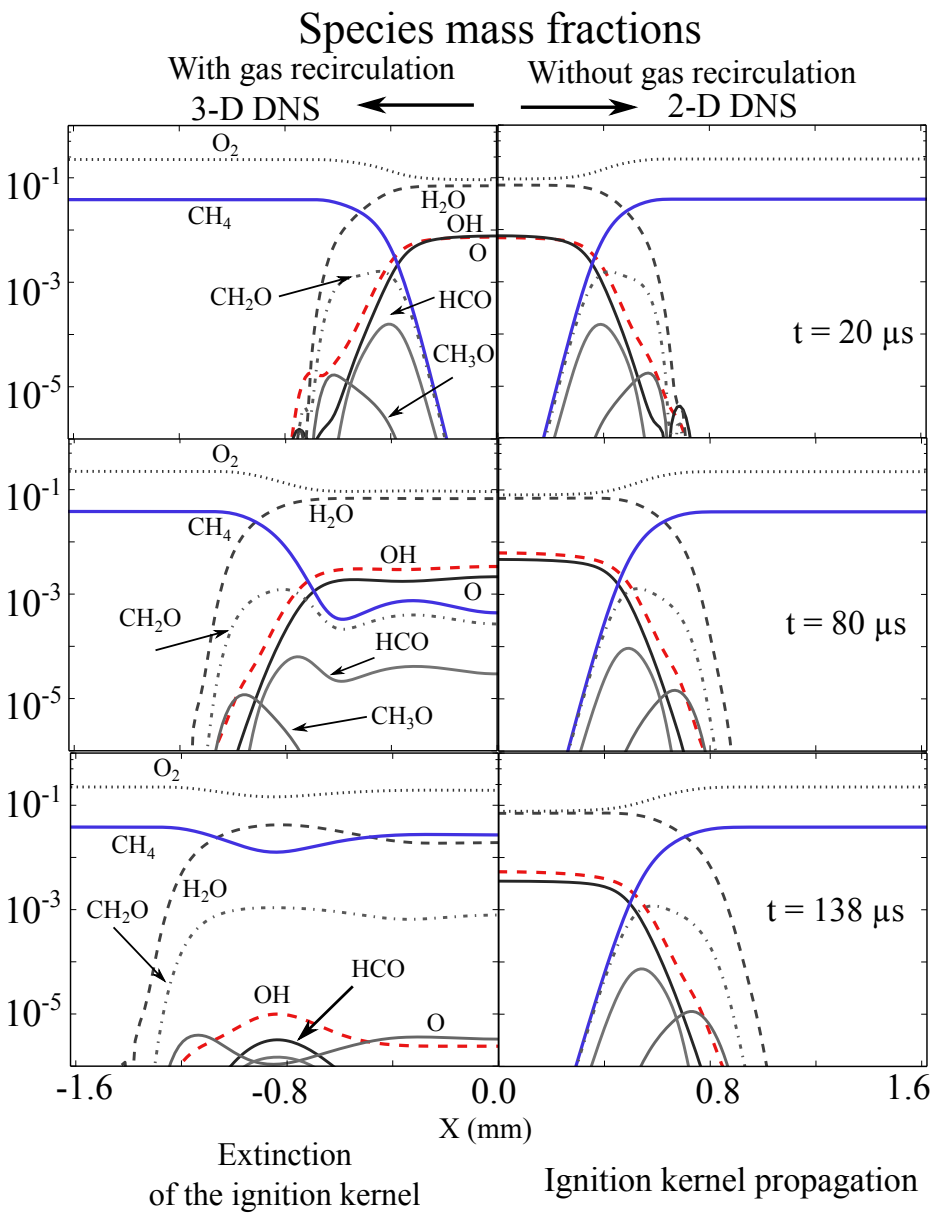

Figure 5.12: *Species mass fractions profiles along the line AA' depicted in Fig. 5.5. Species radial profiles plotted on the left side refer to the 3-D DNS case (with gas recirculation), whereas the profiles plotted on the right side refer to the 2-D DNS case (without gas recirculation).*

The temporal evolution of the O, OH and CH_2O mass fractions that remain inside the discharge channel will determine the minimum value of the pulse frequency at which nanosecond discharge pulses should be applied to successfully ignite and propagate the flame kernel. For example, if plasma discharges are applied at pulse frequencies lower than 5 kHz, (which correspond to a pulse period higher than 200 μs), both the gas temperature and the concentration of radicals inside the discharge channel become similar to those in the fresh mixture. Therefore, the cumulative effect of multiple discharges will be minimal.

On the other hand, gas recirculation may enhance the initial flame kernel propagation at lower pulse frequencies as it spreads long-lasting intermediate combustion species, such as CH_2O and HCO around the discharge zone. By spreading these intermediate species and increasing the gas energy around the discharge zone, more favorable thermochemical conditions are created to successfully propagate the initial ignition kernel. This may explain the flame speed enhancement observed experimentally when using NRP discharges vs. conventional spark discharges. In conventional spark ignition, the conditions downstream of the flame front are those of fresh gases as ignition occurs after a single pulse. In NRP discharge-assisted ignition, the results presented here show that the thermochemical conditions created by long-lasting intermediate species, formed by previous discharges and found downstream of the flame front, may be more favorable for flame front propagation at the early instants.

5.4 Conclusions

The effect of the gas recirculation generated by a single non-equilibrium plasma discharge in a methane-air mixture was analyzed in this chapter. The results show that the formation of a fresh gas counterflow, with stagnation plane at the center of the discharge and perpendicular to the electrodes, changes the topology of the hot kernel from an initial cylindri-

cal shape to a toroidal one. This phenomenon leads to an increase of the area/volume ratio of the reactive kernel, that may result under certain conditions in kernel extinction.

The results also show the importance of considering this 3-D gas flow recirculation to correctly predict the temporal evolution of the hot kernel. In particular, they show that the temperature and species concentrations in the central region of the discharge return to fresh gas conditions shortly after the end of the pulse. In the experimental case investigated here, this time is of the order of 150 μs. Simulation results show that, for example, at pulse frequencies lower than 5 kHz (which corresponds to a pulse period higher than 200 μs), the thermochemical conditions at the center of the discharge channel, by the time of the following pulse, are similar to those in fresh mixture. Therefore, the synergistic effect of multiple discharges on mixture ignition can only be reached if nanosecond discharges are applied at higher pulse frequencies. This result is particularly important for ignition by Nanosecond Repetitively Pulsed (NRP) discharges because it shows that the gas conditions at the beginning of each successive pulse strongly depend on the time interval between pulses, thus on the pulse frequency.

Conclusion and Perspectives

The application of non-equilibrium plasmas to lean premixed or partially premixed combustion regimes can provide additional ways to control mixture ignition and extend flame stability domains. In particular, non-equilibrium plasmas produced by Nanosecond Repetitively Pulsed (NRP) discharges are an energy-efficient way to generate O radicals, even at low gas temperatures, and these radicals can enhance combustion and ignition processes.

Conventional ignition models, based on the assumption of thermal equilibrium, cannot capture this low-temperature generation of radicals and, therefore, additional thermal non-equilibrium processes have to be considered. Although several detailed plasma kinetic models have been proposed in the literature to capture these non-equilibrium processes, they require prohibitive computational resources for DNS studies at high Reynolds numbers.

The model developed in this thesis is a high level model of plasma-assisted ignition that captures the governing plasma phenomena without having to incorporate detailed non-equilibrium plasma kinetics, thus reducing costs of DNS computations for high Reynolds number flows. With this model, multi-dimensional DNS computations of plasma-assisted ignition by repetitively pulsed discharges can be performed to focus on understanding plasma / combustion / turbulence interactions.

In Nanosecond Repetitively Pulsed (NRP) discharges at atmospheric pres-

sure, a large fraction of the discharge energy is channeled into the electronic and vibrational states of N_2 molecules. Dissociative quenching reactions between ground state molecules and electronically excited N_2 molecules lead to an ultrafast increase of the gas temperature and to the production of oxygen atoms. The relaxation of vibrationally excited N_2 molecules takes longer and is associated to a much slower heat release. Based on these phenomenological characteristics, in the present model considered that the discharge energy is decomposed into 1) ultrafast chemical and heat energy deposition with a characteristic time τ_{pulse}; and 2) slow heat energy deposition with a characteristic time τ_{VT}. In the model closure two parameters are defined:

- α: the fraction of the discharge energy that leads to ultrafast heating and O_2 dissociation within $\tau_{pulse} = 50$ ns;

- η: the fraction of the discharge energy leading to O_2 dissociation within $\tau_{pulse} = 50$ ns.

Values of α and η that model typical nanosecond discharges were proposed here. The values of these parameters are based on a review of experimental results and of numerical simulations obtained with detailed plasma kinetic models.

The main conclusions of the simulations performed in this work are summarized as follows:

- The ultrafast energy deposition within $\tau_{pulse} = 50$ ns occurs as a nearly constant volume process. The ultrafast temperature increase is accompanied by an increase of the gas pressure inside the discharge zone leading to gas expansion and shock waves formation at each discharge pulse. In this process only the discharge energy going into ultrafast gas heating contribute to the acoustic energy runaway from the centre of the discharge channel. Because part

of the discharge energy is directly deposited into gas chemical energy (dissociation of O_2) the energy runaway during gas expansion is reduced, since this loss of energy at the centre of the discharge is associated with the fraction of the discharge energy deposited into gas sensible energy.

- The ultrafast dissociation of the O_2 molecules induced by the plasma discharge plays a major role on the ignition enhancement of low temperature mixtures. It decreases the delay and the external energy needed to ignite. Different ignition delays and ignition energies (number of discharge pulses) are obtained depending on whether or not the O_2 dissociation model is considered. If only the ultrafast increase of the gas temperature is considered, the predicted ignition delay increases.

- Simulation results of plasma-assisted ignition in turbulent flows show that turbulence impacts the transient ignition phenomena. Between two consecutive discharges, at high Reynolds number, the radicals produced by the previous pulse are advected away from the discharge zone which reduces the synergy between consecutive pulses of NRP discharges. Furthermore, in turbulent flows, the spatial distribution of the turbulent eddies relative to the discharge zone may also stretch the high-temperature and highly-reactive zone so that diffusion effects will also impact the mixture ignition.

- The recirculating flow pattern observed both in the 3-D DNS and in experiments of a single nanosecond discharge in methane-air mixture also impacts the spatio-temporal evolution of the gas temperature and species concentrations inside the discharge channel. The initial cylinder-shaped discharge channel evolves into a toroidal kernel that may eventually extinguish.

The simulation results of the present work show that ignition by NRP

discharges is influenced by turbulence and that non-equilibrium effects should be considered in the simulation of plasma-assisted ignition in order to capture the fast production of radicals at low gas temperatures. This is particularly critical for simulations of plasma-assisted ignition at high Reynolds number and when ignition occurs only after several discharge pulses.

Future work

The results obtained in this thesis open several perspectives for future work:

- The impact of NRP discharges in reactive mixtures should be analyzed for different mixture equivalence ratios, gas temperatures and pressures. For this, further experimental studies of NRP discharges in a wider range of mixture thermochemical conditions are needed.

- Another interesting future work is to study the impact of different vibrational energy relaxation rates on the ignition phenomena. The model presented here used the relaxation rates of Millikan and White (1963), but as noted in Chapter 2 other rates have been proposed in the literature for instance in Popov (2011a).

- The results presented in this work show that long-lasting intermediate combustion species are being spread around the discharge zone by turbulence and by the recirculating flow pattern induced by the gas expansion. An interesting study would be to analyze which of the discharge energy shapes (inter-electrode gap distances) are more likely to intensify the spreading of these species around the discharge zone. Although higher intensities of the recirculating flow may lead to poorer thermochemical conditions at the centre of the discharge

zone, when mixture ignites after several pulses these long-lasting species around the discharge channel can enhance the development of the ignition kernel.

- As discussed in the 2-D DNS of NRP discharges in turbulent flow conditions, the spatio-temporal evolution of the gas temperature and species concentrations depends on the turbulence levels and on the pulse frequency. It is therefore interesting to analyze the correlation between the pulse frequency and the turbulence intensity. For this, 2-D DNS or 3-D DNS of NRP discharges in different conditions of forced turbulence would be of a great interest to investigate the range of the frequency / turbulence intensity in which mixture always ignites or extinguishes.

- Also of great importance, future work should investigate the impact of the hydrodynamics effects generated by NRP discharges on the smallest scales of turbulence. This investigation is needed in order to derive accurate sub grid scale turbulence models in the context of LES of NRP discharge-assisted ignition / combustion.

- LES of NRP discharge-assisted ignition / combustion are particularly interesting. For instance, LES of the MiniPAC system presented in Pilla et al. (2006) (a schematics of the MiniPAC system in presented in Fig. 1.2 on page 13 of this manuscript), would provide a valuable insight into the phenomena governing plasma-assisted combustion, and help design future plasma-assisted technologies. The plasma model developed in this thesis enables LES with realistic non-equilibrium plasma effects. Yet, LES of the MiniPAC system is particularly challenge as NRP discharges are applied inside the recirculation zone created behind the burner and not in a fresh gas mixture. Therefore, in order to pursue LES of the MiniPAC system, from the model point of view, future work should include the experimental characterization of nanosecond discharges

in burnt gas mixtures (CO_2 and H_2O mixtures). Based on this experimental characterization, the values of the model parameters α and η (or η_i in the case of i ultrafast dissociative processes) can be determined for NRP discharges applied in burnt gases. The phenomena governing NRP discharge-flame stabilization can then be studied in detail by means of relatively simple DNS numerical experiments and provide a priori sub grid scale models for LES of NRP discharge-assisted flame stabilization when discharges are applied in burnt gases. Nevertheless, the model as it is presented in this thesis can be straightforward applied to LES of NRP discharge-assisted ignition provided that a refined mesh grid is used inside and in the vicinity of the discharge zone.

- Finally, extending the generality of the model to simulate other types of discharges (microsecond or millisecond sparks, for instance) should not pose any major difficulty other than adjusting α, η and $\dot{E}^p$ parameters of the present model. These simulations would provide additional insight into spark ignition processes.

Appendix A

Estimation of the computational costs of DNS plasma-assisted ignition (YWC code)

The increase of the number of species considered in the kinetic mechanism, increases the number of equations to solve during the numerical simulations. In plasma-assisted combustion simulations, considering detailed plasma and combustion kinetic mechanisms, the computational costs are higher than those where only combustion species are considered in the simulations. The computational cost associated with multi-species reactive flow computations, referred as the CPU time τ_{CPU}, can be estimated from the following expression:

$$\tau_{CPU} = p\,\tau_p = \frac{N_{ite}\,N_{pts}}{C_{eff}} \tag{A.1}$$

where p refers to the number of processors considered, τ_p the real simulation time using the p processors, N_{ite} the number of iterations performed and N_{pts} the number of points used to discretize the numerical domain. The coefficient $1/C_{eff}$ represents a time cost per iteration and per point associated with a particular DNS solver and depends on the numerical methods, such as the order of the spatial derivatives discretization and temporal integration, as well as on the number of equations to be solved

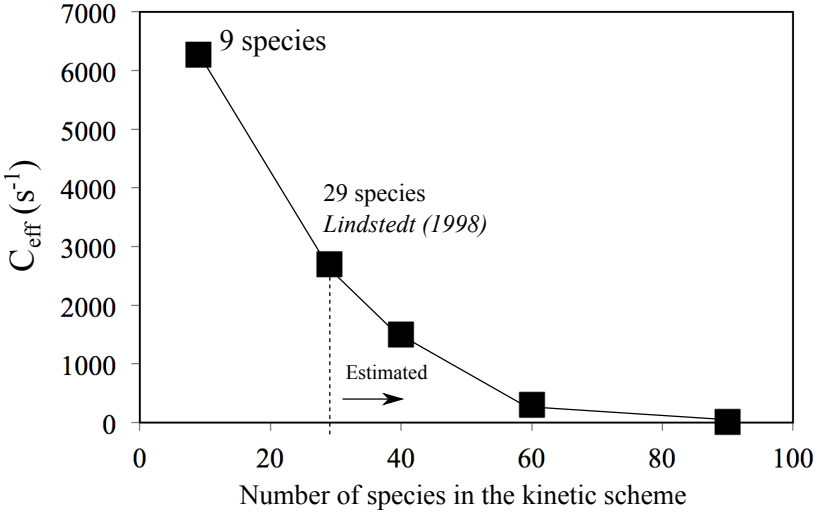

Figure A.1: *Value of the C_{eff} for the YWC DNS solver as a function of the number of species considered in the kinetic scheme.*

during the process. As this number of equations is directly proportional to the number of species considered in the kinetic scheme, the value of $1/C_{eff}$ increases with the increase of the number of species considered in the kinetic mechanism.

Figure A.1 shows the value of C_{eff} characteristic of the DNS solver YWC code, used in the present work, as a function of the number of species. The values of C_{eff} for kinetic mechanisms comprising with 9 and 29 species (Lindstedt mechanism) were obtained from the simulations performed during this thesis. The value of C_{eff} for 40, 60 and 90 species are estimated.

If perfect scalability of the DNS solver among p processors can be achieved, this C_{eff} is independent on the number of processors. Therefore, introducing the value of this coefficient into Eq. (A.1) the estimation of τ_{CPU} will depend on the number of points considered in the domain and on the number of iterations to be performed.

Figure A.2 shows a schematic description of the strategy used to estimate

N_{pts} and N_{ite} in the case of a DNS of NRP discharges-assisted combustion. The following analysis gives an estimation of N_{pts}, N_{ite} and τ_{CPU} for 2-D and 3-D DNS of repetitively pulsed discharges in air and hydrocarbon-air mixtures.

A.1 Estimation of the number of points N_{pts}

The number of points N_{pts} depends on the total length of the computational domain L and on the grid mesh size Δx.

- The length of the computational domain L must be sufficiently large to integrate the characteristic sizes of plasma. For simulations of a pin-to-pin configuration (see Fig. 2.2) the most constraining dimension is the distance of the inter-electrode gap L_d. Therefore, L should be larger than L_d by a factor of C_1 (where C_1 depends on the computational boundary conditions). In NRP discharges-assisted ignition in turbulent flow conditions, the dimension L should also ensure a sufficient number of the turbulent integral length scales $L_{i,i}$ in each spatial direction. Therefore, the value of L is the maximum among the values of $L_1 = C_1\, L_d$ and $L_2 = C_2\, L_{i,i}$.

- The grid mesh size Δx is conditioned by the minimum number of points needed to solve the steep gradients along the radial direction of the plasma channel. A typical radius of this channel is about 250 μm and thus, a mesh grid of about 10 μm represents 25 points inside the discharge channel radius. In the case of turbulent flows, the value of Δx is also conditioned by the Kolmogorov length scale and therefore, $\Delta x = C_2\, \eta_k$ (with a value of C_2 at most equal to 2).

Base on the work developed in this thesis, reasonable values for Δx and L for simulations of repetitively pulsed discharges in air and reactive mixtures are 10 μm and 5.12 mm, respectively. Therefore, considering a uniform mesh, the required number of points N_{pts} in the computation

domain is 512^2 and 512^3 in a 2-D and 3-D configuration, respectively.

A.2 Estimation of the number of iterations N_{ite}

The number of iterations can be estimated from the computational time-step Δt, and the physical time to simulate T_{phys}:

$$N_{ite} = \frac{T_{phys}}{\Delta t} \tag{A.2}$$

- T_{phys} can be estimated as $T_{phys} = N_{pulses}/f$, where N_{pulses} is the number of discharge pulses and f is the pulse frequency.

- The estimation of Δt is more complex, as Δt usually varies during the computations, depending on the chemical and flow characteristic time scales, and on the mesh grid size. Based on the computations performed during the thesis, a mean realistic value for DNS of NRP discharges in air and in hydrocarbon-air mixtures is a Δt between 1 to 5 nanoseconds. Therefore, to simulate 4 to 8 discharge pulses at pulse frequency of 10 kHz would require roughly $N_{ite} = 300\ 000$.

An estimation of the computational costs are given in Table A.1 as a function of the number of species considered in the kinetic mechanism. The values presented in Table A.1 are estimated for 2-D and 3-D DNS considering $N_{pts} = 512^2$ and 512^3, respectively and $N_{ite} = 300\ 000$ (computational domain with $L = 5.12$ mm in each direction with an uniform mesh with $\Delta x = 10\ \mu$m).

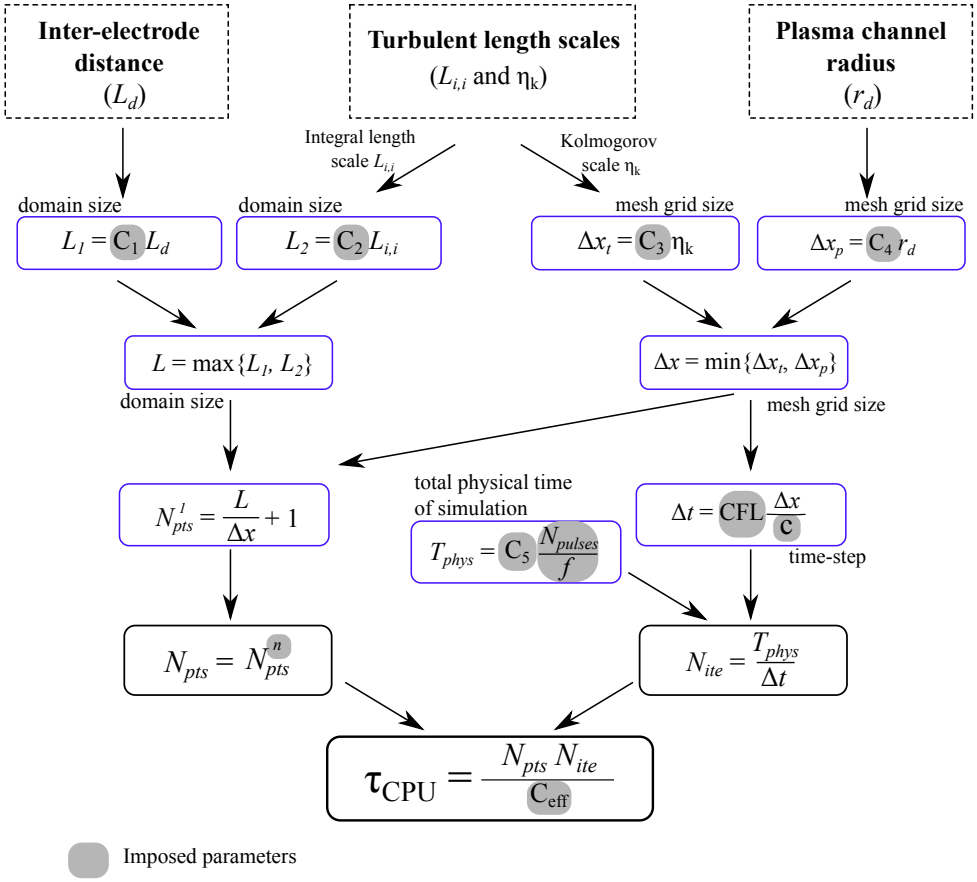

Figure A.2: *Schematic representation of the strategy to estimate N_{pts}, N_{ite} and the computational cost τ_{CPU}.*

Table A.1: *Estimation of the 2-D and 3-D DNS computational costs as a function of the number of species considered in the kinetic mechanism.*

DNS (YWC code)	N_{ite} 300.000	2-D N_{pts} = 512^2		3-D DNS $N_{pts} = 512^3$	
Nb of species	$\mathbf{C}_{eff}$	τ_{CPU} **hCPU**	τ_p **p = 2048**	τ_{CPU} **hCPU**	τ_p **p = 2048**
9	6270	3480	1.7 hours	1.78 $\times 10^6$	36 days
29	2700	8090	4 hours	4.14 $\times 10^6$	85 days
40	1500*	14600	7 hours	7.47$\times 10^6$	149 days
60	300*	72000	36 hours	36.8$\times 10^6$	2 years

Physical time of about 400 to 800 μs

3-D DNS performed in the present thesis:

Nb of species	N_{ite}	N_{pts}	τ_{CPU}	τ_p
29	150.000	256^3	hCPU	p = 2048
Physical time of about 200 μs			3.45 $\times 10^5$	7 days

References

Adamovich, I. V., T. Li, and W. R. Lempert (2015). Kinetic mechanism of molecular energy transfer and chemical reactions in low-temperature air-fuel plasmas. *Philosophical Transactions of the Royal Society A 373*, 20140336. *(p. 25)*

Aleksandrov, N. L., S. V. Kindysheva, M. M. Nudnov, and A. Y. Starikovskiy (2010). Mechanism of ultra-fast heating in a non-equilibrium weakly ionized air discharge plasma in high electric fields. *Journal of Physics D: Applied Physics 43*, 255201. *(p. 49)*

Aleksandrov, N. L., F. I. Vysikailo, R. S. Islamov, I. V. Kochetov, A. P. Napartovich, and V. G. Pevgov (1981). Electron distribution function in 4:1 N_2 - O_2 mixture. *Teplofiz. Vys Temp. 19*(1), 22–27. *(p. 14, 37)*

Babaeva, N. Y. and G. V. Naidis (1997). Dynamics of positive and negative streamersin air in weak uniform electric fields. *IEEE Transactions on Plasma Science 25*(2), 375–379. *(p. 30)*

Bach, E., J. Kariuki, J. R. Dawson, and E. Mastorakus (2013). Spark ignition of single bluff-body premixed flames and annular combustors. *51st AIAA*, 2013–1182. *(p. 9)*

Bak, M. S., H. Do, M. G. Mungal, and M. A. Cappelli (2012). Plasma-assisted stabilization of laminar premixed methane/air flames around the lean flammability limit. *Combustion and Flame 159*(10), 3128–3137. *(p. 19, 33)*

Ballal, D. R. and A. H. Lefebvre (1975). The influence of flow parameters on minimum ignition energy and quenching distance. *Symposium (International) on Combustion 15*(1), 1473–1481. *(p. 8, 9, 17)*

Ballal, D. R. and A. H. Lefebvre (1981). A general model of spark ignition for gaseous and liquid fuel-air mixtures. *Symposium (International) on Combustion 18*(1), 1737–1746. *(p. 17)*

Barbosa, S., G. Pilla, D. A. Lacoste, P. Scouflaire, S. Ducruix, C. O. Laux, and D. Veynante (2015). Influence of nanosecond repetitively pulsed discharges on the stability of a swirled propane/air burner representative of an aeronautical combustor. *Philosophical Transactions of the Royal Society A 373*(2048), 20140335. *(p. 12)*

Bolsig (2005). www.bolsig.laplace.univ-tlse.fr. *(p. 34)*

Bourgouin, J. F., D. Durox, T. Schuller, J. Beaunier, and S. Candel (2013). Ignition dynamics of an annular combustor equipped with multiple swirling injectors. *Combustion and Flame 160*(8), 1398–1413. *(p. 9)*

Bradley, D., C. Sheppard, I. Suardjaja, and R. Woolley (2004). Fundamentals of high-energy spark ignition with lasers. *Combustion and Flame 138*, 55–77. *(p. 111)*

Breden, D., L. L. Raja, C. A. Idicheria, P. M. Najt, and S. Mahadevan (2013). A numerical study of high-pressure non-equilibrium streamers for combustion ignition application. *Journal of Applied Physics 114*, 083302. *(p. 15, 19, 30)*

Candel, S., T. Schmitt, and N. Darabiha (2011). Progress in transcritical combustion: experimentation, modeling and simulation. *23rd ICDERS, Irvine, July*. *(p. 60, 69)*

Cardin, C., B. Renou, G. Cabot, and A. M. Boukhalfa (2013). Experimental analysis of laser-induced spark ignition of lean turbulent

premixed flames: New insight into ignition transition. *Combustion and Flame 160*, 1414–1427. *(p. 8, 111)*

Castela, M., A. S. Verissimo, A. M. A. Rocha, and M. Costa (2012). Experimental study of the combustion regimes occuring in a laboratory combustor. *Combustion Science and Technology 184*(2), 1131–1137. *(p. 6)*

Caudal, J. (2013). Simulation numérique du reformage autothermique du méthane. *Ph.D Thesis, Ecole Centrale Paris*. *(p. 68, 69, 71)*

Cavaliere, A. and M. Joannon (2004). Mild combustion. *Progress in Energy and Combustion Science 30*(4), 329–366. *(p. 5)*

Celestin, S. (2008). Study of the dynamics of streamer in air at atmospheric pressure. *Ph.D Thesis, Ecole Centrale Paris*. *(p. 30, 31)*

Chakraborty, N., E. Mastorakos, and R. S. Cant (2007). Effects of turbulence on spark ignition in inhomogeneous mixtures: a direct numerical simulation (DNS) study. *Combustion Science and Technology* (179), 293–317. *(p. 18)*

Cook, A. W. and W. H. Cabot (2004). A high-wavenumber viscosity for high-resolution numerical methods. *Journal of Computational Physics 195*, 594–601. *(p. 69)*

Cook, A. W. and W. H. Cabot (2005). Hyperviscosity for shock-turbulence interactions. *Journal of Computational Physics 203*, 379–385. *(p. 69)*

Coussement, A. (2012). Direct numerical simulation and reduced chemical schemes for combustion of perfect and real gases. *Ph.D Thesis, Ecole Centrale des Arts et Manufactures*. *(p. 68)*

Coussement, A., O. Gicquel, J. Caudal, B. Fiorina, and G. Degrez (2012). Three-dimensional boundary conditions for numerical simulations of reactive compressible flows with complex thermochemistry. *Journal of Computational Physics 231*(17), 5571–5611.

(p. 70)

Dale, J. D., M. D. Checkel, and P. R. Smy (1997). Application of high energy ignition systems to engines. *Progress Energy Combustion Science 23*(1), 379–398. *(p. 9)*

Dec, J., Y. Yang, and N. Dronniou (2011). Boosted HCCI - controlling pressure-rise rates for performance improvements using partial fuel stratification with conventional gasoline. *SAE International Journal Engines 1*(4), 1169–1189. *(p. 5)*

Dec, J. E. (2009). Advanced compression-ignition engines - understanding the in-cylinder processes. *Proceedings of the Combustion Institute* (32), 2727–2742. *(p. 4, 5)*

Do, H., M. A. Cappelli, and M. G. Mungal (2010a). Plasma assisted cavity flame ignition in supersonic flows. *Combustion and Flame* (157), 1783–1794. *(p. 12)*

Do, H., M. A. Cappelli, and M. G. Mungal (2010b). Plasma assisted flame ignition of supersonic flows over a flat wall. *Combustion and Flame* (157), 2298–2305. *(p. 13)*

Echekki, T. and H. Kolera-Gokula (2007). A regime diagram for premixed flame kernel-vortex interactions. *Physics of Fluids 19*, 043604. *(p. 18)*

Fiorina, B. and S. K. Lele (2007). An artificial nonlinear diffusivity method for supersonic reacting flows with shocks. *Journal of Computational Physics* (222), 246–264. *(p. 69)*

Flitti, A. and S. Pancheshnyi (2009). Gas heating in fast pulsed discharges in n_2-o_2 mixtures. *The European Physical Journal 45*, 21001. *(p. 49)*

Fru, G., D. Thévenin, and G. Janiga (2011). Impact of turbulence intensity and equivalence ratio on the burnin rate of premixed methane-air flames. *Energies 4*(6), 878–893. *(p. 18)*

Ju, Y. and W. Sun (2015). Plasma assisted combustion: Dynamics and chemistry. *Progress of Energy Science and Combustion 48*, 21–83. *(p. 7)*

Kono, M., K. Hatori, and K. Iinuma (1984). Investigation on ignition ability of composite sparks in flowing mixtures. *Symposium (International) on Combustion 20*(1), 133–140. *(p. 8)*

Kono, M., K. Niu, T. Tsukamoto, and Y. Ujiie (1988). Mechanism of flame kernel formation produced by short durantion sparks. *22nd Symposium (International) on Combustion Institute*, 1643–1649. *(p. 109, 111)*

Kosarev, I. N., V. I. Khorunzhenko, E. I. Mintoussov, P. N. Sagulenko, N. A. Popov, and S. M. Starikovskaia (2012). A nanosecond surface dielectric barrier discharge at elevated pressures: time-resolved electric field and efficiency of initiation of combustion. *Plasma Sources Science and Technology 21*, 045012. *(p. 25)*

Kravchik, T. and E. Sher (1994). Numerical modeling of spark lgnition and flame initiation in a quiescent methane-air mixture. *Combustion and Flame 99*(1), 635–643. *(p. 18)*

Kravchik, T., E. Sher, and J. B. Heywood (1995). From spark ignition to flame initiation. *Combustion Science and Technology 108*(1), 1–30. *(p. 18)*

Kruger, C. H., C. O. Laux, L. Yu, D. M. Packan, and L. Pierrot (2002). Nonequilibrium discharges in air and nitrogen plasmas at atmospheric pressure. *Pure and Applied Chemistry 74*(3), 337–347. *(p. 11)*

Lefebvre, A. H. (1998). *Gas Turbine Combustion* (2nd ed.). Taylor & Francis. *(p. 7, 8)*

Lefkowitz, J. K., P. Guo, A. Rousso, and Y. Ju (2015). Species and temperature measurements of methane oxidation in a nanosecond

repetitively pulsed discharge. *Philosophical transactions. Series A, Mathematical, physical, and engineering sciences 373*, 20140333. *(p. 25, 36)*

Lindstedt, P. (1998). Modeling of the chemical complexities of flames. *Proceedings of the Combustion Institute 1*(27), 269–285. *(p. 85, 114)*

Lo, A., G. Cleon, P. Vervisch, and A. Cessou (2012). Spontaneous raman scattering: a useful tool for investigating the afterglow of nanosecond scale discharges in air. *Applied Physics B 107*, 229–242. *(p. 14)*

Macheret, S., M. Shneider, and R. Miles (2005). Energy efficiency of plasma-assisted combustion in ram/scramjet engines. *36th AIAA Plasmadynamics and Lasers Conference, Toronto, Ontario, Canada*, 2005–5371. *(p. 7)*

Maly, R. and M. Vogel (1984). Initiation and propagation of flame fronts in lean CH_4-air mixtures by the three modes of the ignition spark. *Symposium (International) on Combustion 17*(1), 821–831. *(p. 8)*

Marode, E. (1975). The mechanism of spark breakdown in air at atmospheric pressure between a positive point and a plane. I. experimental: Nature of the streamer track. *Journal of Applied Physics 46*(5), 2005–2015. *(p. 30)*

Mastorakos, E. (2009). Ignition of turbulent non-premixed flames. *Progress in energy and combustion science 35*(1), 57–97. *(p. 8)*

Millikan, R. C. and D. R. White (1963). Systematics of vibrational relaxation. *Journal Chemical Physics 39*, 3209–3213. *(p. 40, 45, 53, 76, 132)*

Nagaraja, S., T. Li, J. A. Sutton, I. V. Adamovich, and V. Yang (2015). Nanosecond plasma enhanced $H_2/O_2/N_2$ premixed flat flames. *Pro-*

ceedings of the Combustion Institute 35(3), 3471–3478. *(p. 15)*

Naidis, G. V. (2008). Simulation of spark discharges in high-pressure air sustained by repetitive high-voltage nanosecond pulses. *Journal of Physics D: Applied Physics 41*(23), 234017. *(p. 56)*

Nakaya, S., K. Hatori, M. Tsue, M. Kono, D. Segawa, and T. Kadota (2011). Numerical analysis on flame kernel in spark ignition methane/air mixtures. *Journal of Propulsion and Power 27*(2), 132–138. *(p. 18)*

Nighan, W. L. (1970). Electron energy distributions and collision rates in electrically excited N_2, CO and CO_2. *Physics Review A 2*, 1989–2000. *(p. 14, 37)*

Pai, D. Z., D. A. Lacoste, and C. O. Laux (2010). Nanosecond repetitively pulsed discharges in air at atmospheric pressure - the spark regime. *Plasma Sources Science and Technology 19*(6), 065015. *(p. 30, 59)*

Pancheshnyi, S. V., D. A. Lacoste, A. Bourdon, and C. O. Laux (2006). Ignition of propane-air mixtures by a repetitively pulsed nanosecond discharge. *IEEE Transactions on Plasma Science 34*(6), 2478–2487. *(p. 12)*

Park, C. (1993). Review of chemical-kinetic problems of future NASA missions, i: Earth entries. *Journal of Thermophysics and Heat Transfer 7*(3), 385–39. *(p. 40, 45)*

Pilla, G., D. Galley, D. A. Lacoste, F. Lacas, D. Veynante, and C. Laux (2006). Plasma-enhanced combustion of a lean premixed air-propane turbulent flame using a repetitively pulsed nanosecond discharge. *Plasma Science, IEEE Transactions on 34*(6), 2471–2477. *(p. 12, 133)*

Popov, N. (2001). Investigation of the mechanism for rapid heating of nitrogen and air in gas discharges. *Plasma Physics Reports 27*(10),

886–896. *(p. 25, 39, 49)*

Popov, N. A. (2011a). Fast gas heating in a nitrogen-oxygen discharge plasma: I. kinetic mechanism. *Journal of Physics D: Applied Physics 44*, 285201. *(p. 39, 40, 78, 132)*

Popov, N. A. (2011b). Kinetic processes initiated by a nanosecond high-current discharge in hot air. *Plasma Physics Reports 37*(9), 807–815. *(p. 25)*

Popov, N. A. (2013). Fast gas heating initiated by pulsed nanosecond discharge in atmospheric pressure air. *AIAA Aerospace Sciences Meeting, Grapevine, TX, 7-10 January*, 2013–105251. *(p. 50)*

Reddy, H. and J. Abraham (2013). Influence of turbulence-kernel interactions on flame development in lean methane/air mixtures under natural gas fueled engine conditions. *Fuel 103*(1), 1090–1105. *(p. 18)*

Reinmann, R. and M. Akram (1997). Temporal investigation of a fast spark discharge in chemically inert gases. *Journal of Physics D: Applied Physics 30*, 1125–1134. *(p. 111)*

Reitz, R. D. and G. Duraisamy (2015). Review of high efficiency and clean reactivity controlled compression ignition (RCCI) combustion in internal combustion engines. *Progress in Energy and Combustion Science* (46), 12–71. *(p. 4)*

Rusterholtz, D. L., D. A. Lacoste, G. D. Stancu, D. Z. Pai, and C. O. Laux (2013). Ultrafast heating and oxygen dissociation in atmospheric pressure air by nanosecond repetitively pulsed discharges. *Journal of Physics D: Applied Physics 46*, 464010. *(p. 14, 18, 39, 49, 50, 52, 56, 57, 62, 68, 71, 74, 79)*

Ryan, T., T. Callahan, and D. Mehta (2004). HCCI in a variable compression ration engine - effects of engine variables. *SAE International* (2004-01-1971). *(p. 5)*

Saxena, S. and I. D. Bedoya (2013). Fundamental phenomena affecting low temperature combustion and HCCI engines, high load limits and strategies for extending these limits. *Progress in Energy and Combustion Science* (39), 457–488. *(p. 5)*

Stancu, G. D., F. Kaddouri, D. A. Lacoste, and C. O. Laux (2010). Atmospheric pressure plasma diagnostics by oes, crds and talif. *Journal of Physics D: Applied Physics 43*, 124002. *(p. 14, 18)*

Starik, A. M., B. I. Loukhovitski, A. S. Sharipov, and N. S. Titova (2015). Physics and chemistry of the influence of excited molecules on combustion enhancement. *Philosophical Transactions of the Royal Society A 373*, 20140341. *(p. 25)*

Starikovskiy, A. and N. Aleksandrov (2013). Plasma-assisted ignition and combustion. *Progress in Energy and Combustion Science 39*(1), 61 – 110. *(p. 8, 14, 37)*

Sun, W. (2013). Non-equilibrium plasma-assisted combustion. *Ph.D Thesis, Princeton University*. *(p. 10)*

Sun, W., M. Uddi, S. H. Won, T. Ombrello, C. Carter, and Y. Ju (2012). Kinetic effects of non-equilibrium plasma-assisted methane oxidation on diffusion flame extinction limits. *Combustion and Flame 159*(1), 221–229. *(p. 14)*

Tagalian, J. and J. B. Heywood (1986). Flame initiation in a spark-ignition engine. *Combustion and Flame 64*(1), 243–246. *(p. 8, 9)*

Taylor, A. M. K. P. (2008). Science review of internal combustion engines. *Energy Policy* (36), 4657–4667. *(p. 4)*

Thiele, M., S. Selle, U. Riedel, J. Warnatz, and U. Maas (2000). Numerical simulation of spark ignition including ionization. *Proceedings of the Combustion Institute 28*, 1177–1185. *(p. 18, 109)*

Thiele, M., J. Warnatz, and U. Maas (2000). Geometrical study of spark ignition in two dimensions. *Combustion Theory and Modelling 4*(4),

413–434. *(p. 18, 109)*

Tholin, F. (2012). Numerical simulation of nanosecond repetitively pulsed discharges in air at atmospheric pressure: application to plasma-assisted combustion. *Ph.D Thesis, Ecole Centrale Paris*. *(p. 30, 31, 69)*

Tholin, F., D. A. Lacoste, and A. Bourdon (2014). Influence of fast-heating processes and o atom production by a nanosecond spark discharge on the ignition of a lean h2/air premixed flame. *Combustion and Flame 161*, 1235–1246. *(p. 19)*

Vasquez-Espí, C. and A. Liñan (2001). Fast, non-diffusive ignition of a gaseous reacting mixture subject to a point energy source. *Combustion Theory and Modelling*, 485–498. *(p. 50)*

Verissimo, A. S., A. M. A. Rocha, and M. Costa (2011). Operational, combustion and emission characteristics of a small-scale combustor. *Energy Fuels 25*(1), 2469–2480. *(p. 5)*

Xu, D. (2013). Thermal and hydrodynamic effects of nanosecond discharges in air and application to plasma-assisted combustion. *Ph.D Thesis, Ecole Centrale Paris*. *(p. 15)*

Xu, D. A., D. A. Lacoste, and C. O. Laux (2015). Ignition of quiescent lean propane-air mixtures at high pressure by Nanosecond Repetitively Pulsed discharges. *Plasma Chemistry and Plasma Processing* (272-4324), 1–19. *(p. 12, 15, 112, 114)*

Xu, D. A., D. A. Lacoste, D. L. Rusterholtz, P. Q. Elias, G. D. Stancu, and C. O. Laux (2011). Experimental study of the hydrodynamic expansion following a nanosecond repetitively pulsed discharge in air. *Applied Physics Letters 99*, 121502. *(p. 15, 19, 69, 78)*

Xu, D. A., M. N. Shneider, D. A. Lacoste, and C. O. Laux (2014). Thermal and hydrodynamic effects of nanosecond discharges in atmospheric pressure air. *Journal of Physics D: Applied Physics 47*(23),

235202. *(p. 69, 79, 117)*

Yang, W. and W. Blasiak (2005). Mild combustion. *Energy and Fuels 19*(1), 1473–1483. *(p. 5)*

Yin, Z., I. Adamovich, and W. Lempert (2013). Measurements of temperature and hydroxyl radical generation / decay in lean fuel-air mixtures excited by a repetitively pulsed nanosecond discharge. *Proceedings of the Combustion Institute 34*(2), 3249–3258. *(p. 15)*

Ziegler, G. F. W., E. P. Wagner, and R. R. Maly (1984). Ignition of lean methane-air mixtures by high pressure glow and arc discharges. *Symposium (International) on Combustion 20*(1), 1817–1824. *(p. 8)*

université PARIS-SACLAY | ÉCOLE DOCTORALE Sciences mécaniques et énergétiques, matériaux et géosciences (SMEMAG)

Titre: Études DNS des décharges plasma hors-équilibre dans des mélanges reactifs au repot et en regime d'écoulement turbulent

Mots-clés: Allumage assistée par plasma, modélisation des plasmas hors-équilibre, turbulence.

Résumé: La combustion assitée par plasma a reçu une attention croissante dans les deux communautés de plasma et de combustion. Les décharges Nanoseconde Répétitive Pulsée (NRP) sont des techniques prometteuse et efficaces pour initier et contrôler les processus de la combustion en particulier quand les systèmes d'allumage conventionnels sont inefficaces ou trop coûteux en énergie. Néanmoins, les phénomènes rencontrés dans la combustion assistée par plasma sont encore mal connus. Les études numériques présentées dans la litérature sont limitées á des simulations 1-D et 2-D dans des conditions au repos. La complexité du problème augmente dans les configurations pratiques oú le phénomène d'allumage est contrôlé par le mouvement du fluide ainsi que le mélange autour de la zone de décharge. La simulations numérique directe (DNS) est un outil de recherche puissant pour la compréhension des interactions plasma/combustion/écoulement. Toutefois, le coût de calcul de la combustion turbulente avec un nombre de Reynolds élevé et la cinétique chimique détaillée couplée avec le plasma hors-équilibre est prohibitif. Cette thèse présente un nouveau modèle de couplage plasma-combustion pour introduire les effets des décharges de plasma hors-equilibre dans le système d'équations qui décrit le phénomène de la combustion. Le modèle est construit en analysant les chemins par lesquels l'énergie électrique est transferrée au gaz. Ce modèle de décharges NRP permet des simulations multidimensionales DNS de la combustion et l'allumage assistés par plasma. Les phénomènes physiques complexes de l'allumage assisté par décharges multiples de plasma dans des dans mélanges au repot et en regime d'écoulement turbulent sont analysés dans cette thèse.

Title: DNS of plasma-assisted ignition in quiescent and turbulent flow conditions.

Keywords: Plasma-assisted ignition, non-equilibrium plasmas modelling , plasma turbulence.

Abstract: Plasma-assisted combustion has received increasing attention in both plasma and combustion communities. Nanosecond Repetitively Pulsed (NRP) discharges are a promising and efficient technique to initiate and control combustion processes particularly when conventional ignition systems are rather ineffective or too energy costly. Even though a promising technique, the phenomena occurring in NRP discharges-assisted combustion are still poorly understood. The numerical studies presented in the literature are limited to 1-D and 2-D simulations in quiescent conditions. The problem complexity increases in practical configurations as ignition is also controlled by the mixing field characteristics in the vicinity of the discharge channel. Direct Numerical Simulations (DNS) is a powerful research tool to understand these plasma/combustion/flow interactions. However, the computational cost of fully coupled detailed non-equilibrium plasma and combustion chemistry, and high Reynolds number simulations is prohibitive. This thesis presents a novel plasma combustion model to describe the effects of non-equilibrium plasma discharges in the set of equations governing the combustion phenomena. The model is constructed by analyzing the channels through which the electric energy is transferred into the gas. This high-level model of NRP discharges allows DNS studies of plasma-assisted combustion / ignition in high turbulent Reynolds number. The complex physics underlying plasma-assisted ignition by multiple discharges in both quiescent and turbulent flow conditions are discussed in the present thesis.

Université Paris-Saclay
Espace Technologique / Immeuble Discovery
Route de l'Orme aux Merisiers RD 128 / 91190 Saint-Aubin, France